広島大学学位請求論文

Dynamics Study on Dissociation of Polyatomic Molecules Initiated by Photoexcitation of Chromophores

発色団の光励起に起因した
多原子分子解離反応の動力学的研究

２０１７年

広島大学大学院理学研究科
化学専攻

住田　聖太

目　次

1. 主論文

(英タイトル)

Dynamics Study on Dissociation of Polyatomic Molecules Initiated by Photoexcitation of Chromophores

(和タイトル)

発色団の光励起に起因した多原子分子解離反応の動力学的研究

2. 公表論文

[1] Photodissociation dynamics of C_3H_5I in the near-ultraviolet region
Masataka Sumida, Takuya Hanada, Katsuyoshi Yamasaki, Hiroshi Kohguchi
The Journal of Chemical Physics, vol. 141, 104316, 2014.

[2] Multiple product pathways in photodissociation of nitromethane at 213 nm
Masataka Sumida, Yasunori Kohge, Katsuyoshi Yamasaki, Hiroshi Kohguchi
The Journal of Chemical Physics, vol. 144, 064304, 2016.

3. 参考論文

[1] Photodissociation dynamics of nitromethane at 213 nm studied by ion-imaging
Yasunori Kohge, Takuya Hanada, Masataka Sumida, Katsuyoshi Yamasaki, Hiroshi Kohguchi
Chemical Physics Letters, vol. 29, 49, 2012.

[2] Internal and Translational Energy Partitioning of the NO Product in the S_2 Photodissociation of Methyl Nitrite
Masataka Sumida, Shu Masumoto, Mitsue Kato, Katsuyoshi Yamasaki, and Hiroshi Kohguchi
Chemical Physics Letters, 2017 (*accepted*).

[3] Multistep Intersystem Crossing Pathways in Cinnamate-Based UV-B Sunscreens
Kaoru Yamazaki, Yasunori Miyazaki, Yu Harabuchi, Tetsuya Taketsugu, Satoshi Maeda, Yoshiya Inokuchi, Shin-nosuke Kinoshita, Masataka Sumida, Yuuki Onitsuka, Hiroshi Kohguchi, Masahiro Ehara, Takayuki Ebata
The Journal of Physical Chemistry Letters, vol. 7, 4001, 2016.

Acknowledgement

This thesis owes its existence to the help, support, and inspiration of many people. First of all, I would like to express my sincere appreciation to my supervisor, Assoc. prof. Hiroshi Kohguchi for providing me this precious study opportunity as a Ph.D student in his laboratory. His enormous advice, support, and encouragement guide this doctoral thesis to complete. I would like to show my greatest appreciation to Prof. Katsuyoshi Yamasaki for useful discussions and valuable comments. I would like to thank Assoc. prof. Osamu Takahashi for helpful discussions and encouragement. I would like to express my gratitude to Prof. Takayuki Ebata for giving me insightful comments and suggestions, and providing me an opportunity for collaborative research, which broadened my knowledge and understanding. I am thankful to Prof. Misako Aida and for her constructive comments and suggestions on an earlier version of this thesis. I would like to appreciate all staff members of the Innovation Plaza at Hiroshima University for their immense assistance with development of the experimental apparatus, which will be shown in Chapter 2 in this thesis. Finally, I wish to offer my special thanks to all of the previous and present members of the research group of physical chemistry of kinetics and dynamics. The discussions and cooperation with them have contributed substantially to completion of this thesis.

March 1st, 2017

Masataka Sumida

主論文

Chapter 1.
General Introduction

1.1 Molecular Reaction Dynamics of Polyatomic Molecules

Molecular reaction dynamics is the field of chemistry to study elementary chemical reactions at a molecule level and to develop the methods for probing them or controlling them. Elucidating the molecular level mechanism of chemical and physical processes is a common aim for all chemists, because it is essential for understanding reaction mechanisms in any branches of chemistry; gas phase reactions such as atmospheric reactions and chain-branching combustion reactions, condensed phase reactions such as a proton or an electron transfers in solutions, reactions including ions or ionic compounds, catalytic reactions on metal surfaces, biochemical reactions such as enzymatic reactions in proteins, and so on.

Due to the simplest chemical bond rearrangement case, the unimolecular dissociation of a photoenergized molecule has been vigorously investigated with various types of experimental and theoretical studies. The dissociation of a photoexcited molecule is governed by the nuclear dynamics on the potential energy surfaces (PESs), consequently leading to characteristic internal state distributions and scattering distributions of the fragment molecules. The dissociation dynamics of a polyatomic molecule is very complex compared to that of small molecule, since it is involved with multiple and multidimensional PESs with similar energy. In the case the multidimensional PESs lie close to each other, their PESs frequently will undergo avoid crossing and then non-adiabatic transitions will frequently occur. However, because of this complexity, the dissociation dynamics of a polyatomic molecule provides essential information for breaking or making of a chemical bond.

1.2 Photochemistry of Polyatomic Molecules

Generally, a polyatomic molecule exhibits the characteristic photoabsorptions in specific visible (Vis) or ultraviolet (UV) wavelength region. These photoabsorption bands can be ascribed to the electronic transitions from the S_0 state to upper excited S_n (n = 1, 2, 3, …) states. Figure 1.1 shows UV photoabsorption spectra of several polyatomic molecules. Each spectrum shows one or more absorption bands in the characteristic wavelength region, which are often simply ascribed to the local excitations of functional groups in the molecule as a concept of "chromophore". In organic chemistry, this concept has been of use to determine a molecular structure and measure a reagent concentration since long ago. Recently, the molecular orbital (MO) method calculation technique has been developed and revealed the detailed correlation between the photoabsorption bands and electronic transitions of a polyatomic molecule.

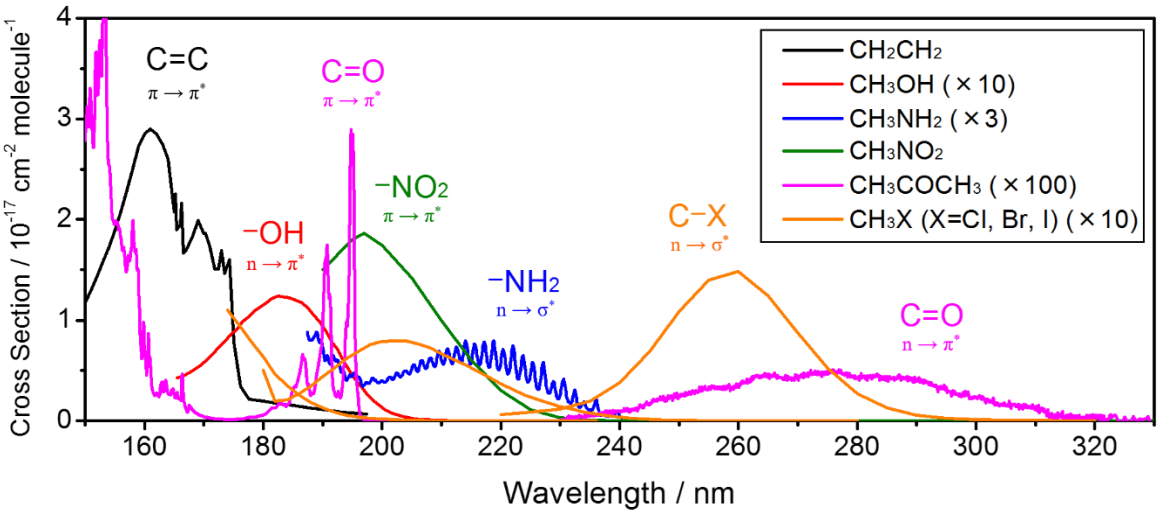

Figure 1.1 UV photoabsorption spectra of polyatomic molecules

While the photoabsorption step of a polyatomic molecule has been understood by the MO method, the dissociation step following the photoexcitation has not been completely understood by quantum mechanical calculations. In the photodissociation of a polyatomic molecule, the timescales of electronic and nuclear motions become comparable, leading to considerable coupling between electronic and nuclear motion. Thus, the breakdown of the Born-Oppenheimer approximation occurs, and consequently, the dissociation dynamics will be characterized by non-adiabatic effects. This complexity makes difficult to completely predict the dissociation dynamics of a polyatomic molecule by only the theoretical methods. For elucidating the complex reactions of polyatomic molecules, one needs to perform various types of experimental approaches and quantum mechanical calculations, and consider it in all its bearings.

It is helpful to systematically understand the dissociation dynamics of a polyatomic molecule by associating with understanding of the photoabsorption bands characterized by a concept of chromophore. The motion of larger molecules are more complex than smaller ones because the number of nuclear motion is increased with the increase of the number of atoms. However, the photodissociation of the polyatomic molecules with the same chromophore would represents the similar dynamics characterized by the local photoexcitation of the same chromophore. Thus, the elucidation of the photodissociation dynamics of the smallest molecule with a certain chromophore would be a benchmark for understanding that of larger molecules with the same chromophore.

1.3 Experimental Approaches for Photodissociation Dynamics

A pump-probe experiment has been widely used for exploring the molecular photodissociation dynamics. This experiment utilizes two different pulsed laser, a pump laser and a probe laser. A pump pulse interacts with a sample and initiates a photodissociation reaction. After a given delay, a probe pulse monitors the dissociating sample or the photoproducts. By the difference of the physical quantities of interest, the pump-probe experiment can be largely classified into two types of complemental methods; a frequency-resolved method and a time-resolved method. The former enables to state-selective detection of the photoproducts in the asymptotic states, while the latter enables to monitor the dissociating molecule in real time. The schematic view of these methods are shown in Figure 1.2.

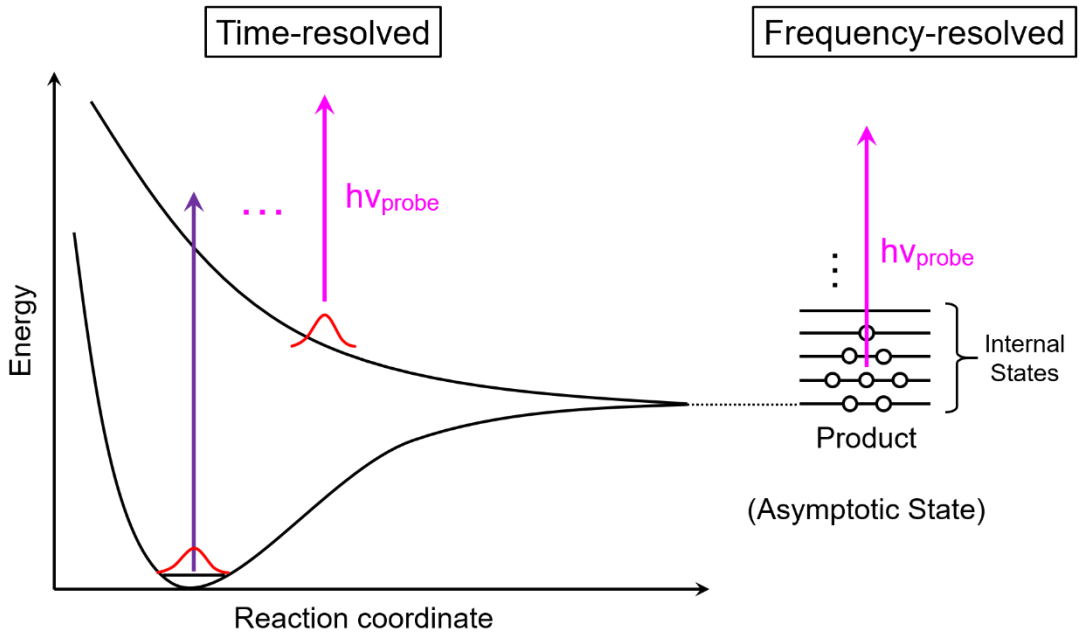

Figure 1.2 Schematic view of two types of laser pump-probe experiments; a frequency-resolved method and a time-resolved method.

One can measure the product energy disposal in a photodissociation with the state-resolved method. Energy disposal is one of the important information for understanding nuclear dynamics on excited state PESs. A number of spectroscopic techniques have been applied for detecting photoproducts. One of the detection techniques is resonantly-enhanced multiphoton ionization (REMPI) spectroscopy, which enables to select a certain state of a photoproduct to be ionized via a resonant excitation to an intermediate state by absorbing multiple photons. By detecting the nascent ion, one can obtain the internal state distribution of a photoproduct (see also Section 2.2.1). Laser-induced fluorescence (LIF) spectroscopy is also one of the detection techniques. In this technique, a probe laser pulse generates electronically excited photoproducts which then emits fluorescence. One can obtain the information of the energy distribution of the photoproducts by detecting the fluorescence (see also Section 2.2.3).

The translational energy distribution and the scattering angle distribution of photoproducts also provide important information for the molecular photodissociation dynamics. By combining the quantum state-selective ionizing technique with a time of flight (TOF) measurement technique, one can state-selectively observe the translational energy distribution of a photoproduct. In this method, a first pump laser pulse generates electronically excited parent molecules which then undergo dissociation. After the completion of the dissociation, a second probe pulse state-selectively ionizes photoproducts by REMPI technique. The formed ions are detected by a TOF spectrometer. Finally, the observed TOF spectrum is converted into the center-of-mass (CM) frame translational energy distribution. A scattering angle distribution of the

photoproduct can be observed by detecting the ions with the TOF spectrometer moved in the laboratory-fixed (LAB) frame angle. This method is different from the non-state selective method using a universal detector, which can detect all the neutral particles with the mass of interest. The velocity map imaging (VMI), which Eppink and Parker have developed by modifying the traditional photofragment imaging technique in 1997,[1] is a powerful technique because it enables to observe the velocity and angle distributions of scattered particles simultaneously. The method of VMI will be explained in detail in Section 2.2.2.

A time-resolved method, which is another technique utilized in laser pump-probe experiments, using femtosecond pulse lasers was applied for exploring the molecular photodissociation dynamics in the time domain by Zewail[2] in 1990s for the first time. In this method, a probe laser pulse monitors the change of the nuclear motions of a dissociating molecule induced by a pump laser pulse. A time-resolved experiment reveals how the chemical change unfolds in time, namely enabling one to watch the breaking or making of a chemical bond in real time.

1.4 The Present Study

The present study has focused on the correlation between the photoabsorptions characterized by chromophores and the following dissociations of polyatomic molecules. For elucidating this correlation, state-resolved laser pump-probe experiments have been carried out. I have designed and developed a VMI apparatus, and then applied it to explore the photodissociation reactions of three polyatomic molecules, C_3H_5I, CH_3NO_2, and CH_3ONO, in a molecular beam. From observed internal state distributions and scattering distributions of the photofragments, I will discuss the photodissociation dynamics of the polyatomic molecules.

In Chapter 2, I will explain the experimental apparatus developed for the present researches and experimental principles. In the following Chapters, I will represent the experimental results and discuss the photodissociation of three polyatomic molecules. The photodissociation process of each molecule is characterized by significantly different dynamics. In Chapter 3, the photodissociation dynamics of allyl iodide (C_3H_5I) will be discussed by focusing on the correlation between two UV photoabsorption bands ascribed to the local excitation in two different chromophores, C–I and C=C bonds, respectively, and the following C–I bond dissociation dynamics. In Chapter 4, the $\pi\pi^*$ photodissociation dynamics of nitromethane (CH_3NO_2) characterized by competitive multiple product pathways will be discussed. In Chapter 5, the direct O–N bond dissociation dynamics of methyl nitrite (CH_3ONO) on the S_2 PES will be discussed. Finally, I will conclude this thesis in Chapter 6.

Chapter 2.
Experimental Apparatus and Method

2.1 Apparatus Development

In this section, I will describe the experimental apparatus which has been designed and developed for the present research. Detailed experimental principles have been explained in Section 2.2.

The experimental setup used in the present study was a standard VMI apparatus combined with a molecular beam LIF detector, as shown in Figure 2.1. The VMI apparatus consists of a handmade supersonic molecular beam source and an imaging system with a time-of-flight detector. The molecular beam generated into the source chamber by a pulsed valve driven by a piezoelectric plate[3, 4] was introduced to the detector chamber through a skimmer (0.8 mm ϕ). The photolysis laser light was moderately focused on the molecular beam between the repeller and extractor electrodes with a quartz lens (f = 350 mm). The photolysis laser pulses were linearly polarized along the Y axis in Figure 2.1, which was perpendicular to the molecular beam aligned along the Z axis and parallel to a detector surface (XY plane). The fourth (266 nm) or the fifth (212.8 nm) harmonics of a Nd:YAG laser output (NY81DP dual-head, Continuum) was used for the photolysis light source. The probe laser was aligned with the pump laser in the counter-propagating direction and was focused on the interaction region, which was shown as the red cross mark on the right in Figure 2.1 (b), with another quartz lens (f = 350 mm). The probe laser pulse was optically delayed with respect to the photolysis pulse by 20-40 ns. The delay period was sufficient to separate the two laser pulses. The probe laser ionized the nascent photofragments state-selectively by REMPI spectroscopy, which has been mentioned in Section 2.2.1.

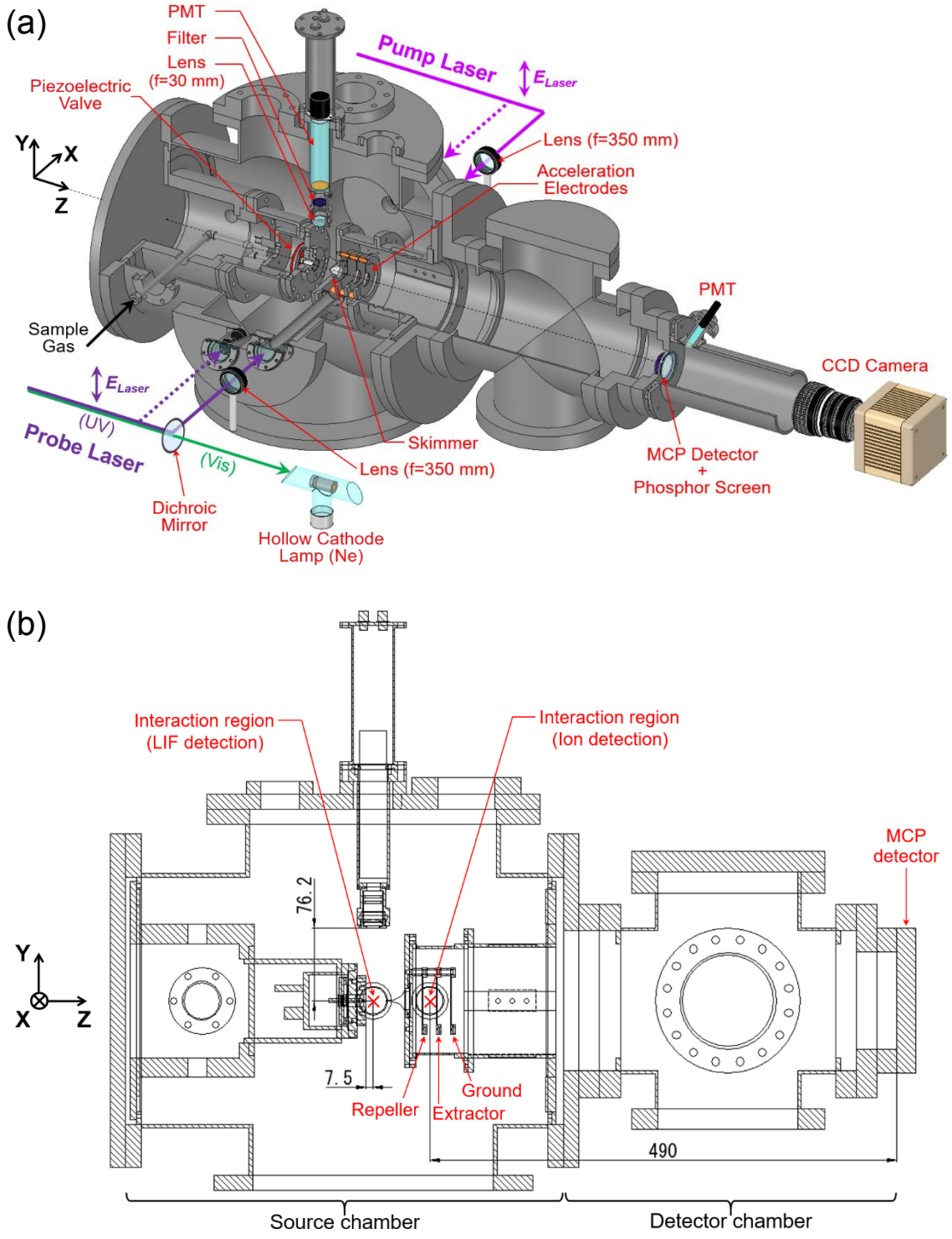

Figure 2.1 Experimental apparatus: (a) a 3D drawing and (b) a cross-sectional view (in the YZ plane). (a) The laser setup for detecting the photo-fragment by REMPI method is shown as a purple solid arrow, while that for detecting LIF is a purple dotted arrow. (b) Red cross marks indicate the positions of the interaction region for an ion detection and a LIF detection, respectively.

The light source for probing the photofragment was a dye laser (CobraStretch, Sirah) with a frequency-doubling unit pumped by a Nd:YAG laser. The probe laser wavelength was calibrated using an optogalvanic method[4] based on a Fe hollow cathode discharge lamp filled with Ne (Hamamatsu, L2783-26). The dye laser fundamental was separated from the frequency doubled light with a dichroic mirror and introduced into the hollow cathode lamp. The wavelengths of observed REMPI and LIF spectra were calibrated by simultaneously recorded Ne optogalvanic signal peaks, which serve as very accurate wavelength markers.

The operations of the pulsed valve, the pump and probe laser pulses, and detection electronics were synchronously controlled by a cascade of digital delay generators (Model555 BNC and DG535 SRS) with a repetition rate of 10 Hz. A microchannel plate (MCP) detector (Chevron-type, Photonis) was gated with a pulsed high voltage of 0.1 μs width to amplify only those ions with the mass of interest. The ionized products were accelerated by an electric field applied by three electrodes with voltages adjusted to a VMI condition (see Section 2.2.2), which was determined using the simulation with the ion optics simulation program of SIMION 8.0. After the acceleration, ions drifted the free flight length of 490 mm toward MCP detector with a phosphor screen in the back. The position of an ion arriving at the phosphor screen was recorded by a CCD camera (Hamamatsu C8800). The image data were collected for the 50,000-100,000 laser cycles with a centroiding algorithm, which provided a real-time ion-counting method.[5, 6] One of the merits of the ion-counting method in the present study is correction of uneven sensitivity of the MCP detector. The ion intensity was obtained with a photomultiplier tube (PMT, Hamamatsu,

R2496), which detected the emission from the phosphor screen.

The laser setup for LIF detection is shown in Figure 2.1 (a) as purple dotted arrows. The methodology and principle of LIF have been mentioned in Section 2.2.3. The unfocused photolysis laser beam was introduced into the chamber and was crossed the supersonic free-jet expansion 7.5 mm downstream from the end of the nozzle. The unfocused probe laser beam propagated along the same axis as the pump laser beam but in the opposite direction and excited the nascent photofragments. The probe laser pulse was optically delayed with respect to the photolysis pulse by 0.5-2 μs. The LIF detector consisting of a quartz lens with a focal length of 30 mm, a filter, and a PMT (Hamamatsu, R374) was located at the distance of 76.2 mm from the interaction region (shown in Figure 2.1 (b) as the red cross mark on the left) and at right angles to the XZ plane shown in Figure 2.1 (a). The fluorescence was collected through a quartz lens and observed through a suitable filter with a PMT. For reducing scattered light, two light baffles were respectively mounted into the laser ports on both sides of the source chamber.

2.2 Experimental Principles

2.2.1 REMPI Spectroscopy

Resonantly-enhanced multiphoton ionization (REMPI) spectroscopy is one of the widely utilized techniques in reaction dynamics experiments which involve very small numbers of neutral molecule. A typical pump-probe experiment under single collision conditions may produces a few hundred products. REMPI method can detect these products high sensitively and specify the chemical species.

REMPI is a multiphoton ionization process induced by laser excitation, as shown in Figure 2.2. In the first step, a molecule in the populated state absorbs one or more photons to be resonantly excited to the intermediate state. Following that, the molecule in the intermediate state absorbs one or more additional photons to be ionized. By scanning the probe laser wavelength while detecting nascent ions, one can observe a vibronic spectrum. The intensities of the spectral peaks are divided by the transition intensity whereby an internal state distribution is obtained.

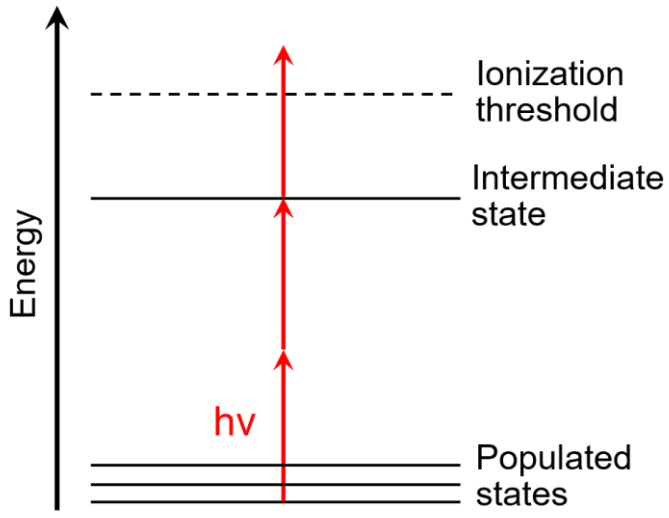

Figure 2.2 Principle of REMPI spectroscopy

REMPI schemes are usually labeled as "[m + n] REMPI", where m indicates the number of photons required to excite a molecule from the populated state to the resonance state and n indicates the number of photons required to ionize the molecule in the resonant state. For example, REMPI scheme illustrated in Figure 2.2, which requires two photons for the excitation and one photon for the ionization, is labeled as "[2 + 1] REMPI".

2.2.2 Velocity Map Imaging

2.2.2.1 Principle and Method

Velocity map imaging (VMI)[7] is an experimental technique that enables the measurement of the "full" three-dimensional (3D) velocity distribution of scattered particles. The term "full" indicates inclusion of all information; the kinetic energy and angular distributions of scattered particles. A schematic of a standard VMI apparatus used for the photodissociation researches is presented in Figure 2.3. A VMI apparatus consists of a beam source, skimmer, three optical lens electrodes (repeller, extractor, and ground electrodes), a two-dimensional (2D) detector and a CCD camera.

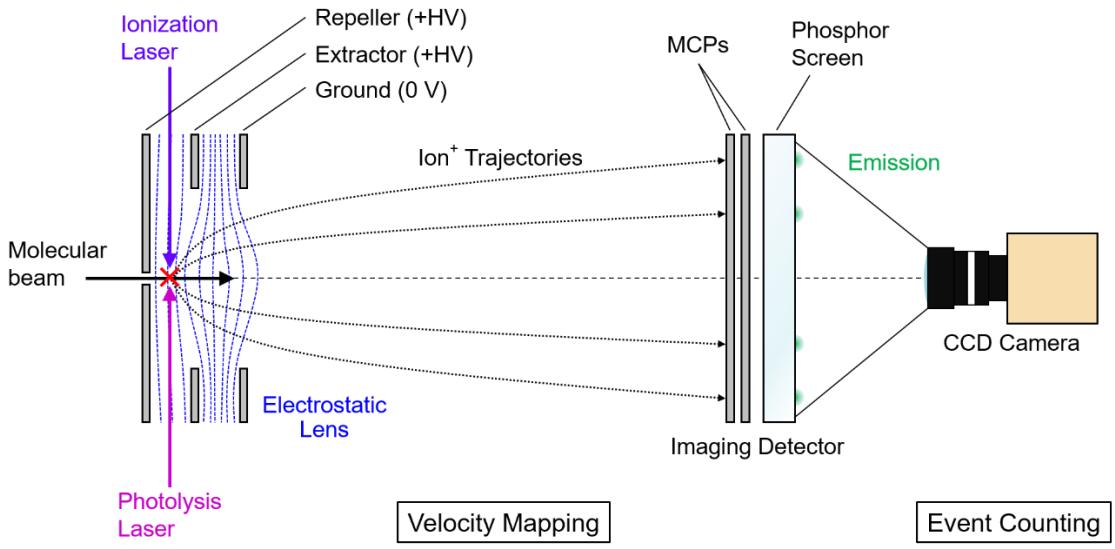

Figure 2.3 Schematic view of the standard VMI apparatus

A molecular beam is generated by the beam source, which is mounted along the direction of a TOF tube and perpendicular to a detector surface and the laser axis, and introduced into the detector chamber through a skimmer. The molecular beam is crossed with a pair of counter propagating laser beams. The photolysis laser dissociates the parent molecule. After a short delay of generally tens of nanoseconds, the probe laser ionizes the scattered fragments with a recoil velocity quantum state-selectively via REMPI process (see Chapter 2.2.1). The laser produced ions are accelerated by the electrostatic lens field (shown in Figure 2.3 as blue dashed lines) created by three electrodes along a flight tube toward a 2D position sensitive detector, which consists of a microchannel plate (MCP) coupled to a phosphor screen, by a three-electrode electrostatic lens as shown in Figure 2.4. The voltages of three electrodes are adjusted to a velocity map imaging (VMI) condition, under which all particles with the same initial velocity vector are mapped onto the same point on the detector. When an ion hits on the MCP detector surface, the corresponding position on the phosphor screen installed in the back side of the MCP detector emits light. By recording the light distribution on the phosphor screen with a CCD camera, one can obtain a scattering distribution of the arriving ions.

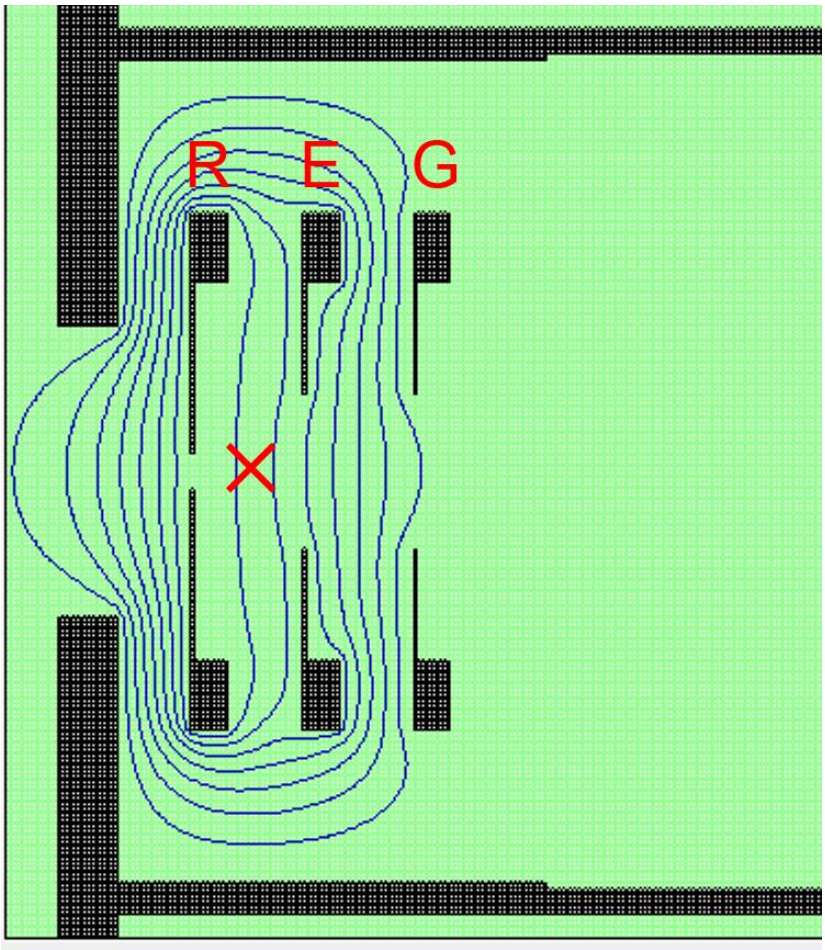

Figure 2.4 Electrostatic lens formation by three VMI electrodes, R: Repeller, E: Extractor, and G: Ground, simulated with SIMION 8.0 for. Black grid indicates electrodes and blue lines indicate an electric field calculated for electrodes.

2.2.2.2 Analysis of a Scattering Distribution

In this type of experiment, a 3D expanding sphere of charged particles is projected down a flight tube creating a 2D image at the detector, as shown in Figure 2.5. The reconstruction of the original 3D Newton sphere of expanding charged particles from observed 2D projection image is required. One of the inversion methods is the polar basis set expansion (pBasex) method,[8] which reconstructs the original distribution by fitting a set of basis functions with a known inverse Abel integral to two the 2D projection image. For example, Figure 2.6 represents the scattering distribution and a 3D slice image of atomic oxygen ions (O^+) produced in the dissociation of a molecular oxygen (O_2) following a UV multiphoton excitation to high Rydberg states.

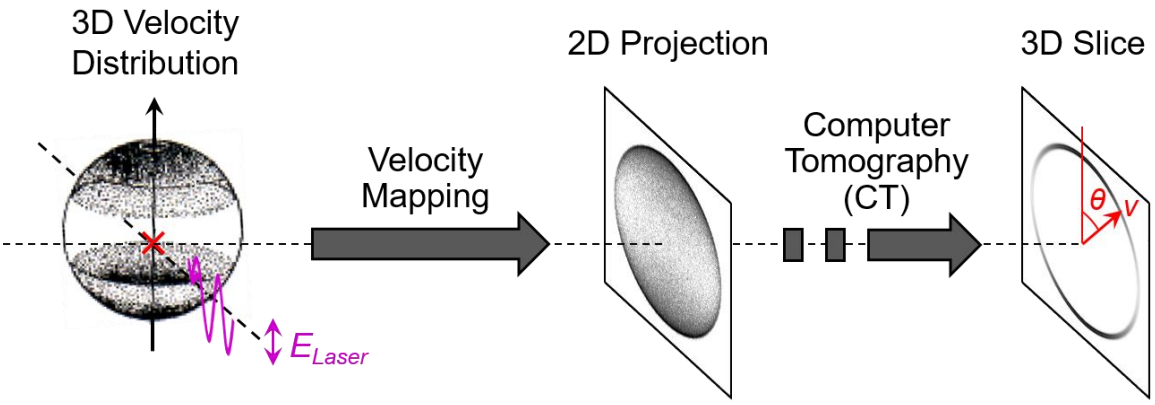

Figure 2.5 Measurement and analysis of 3D Newton sphere.

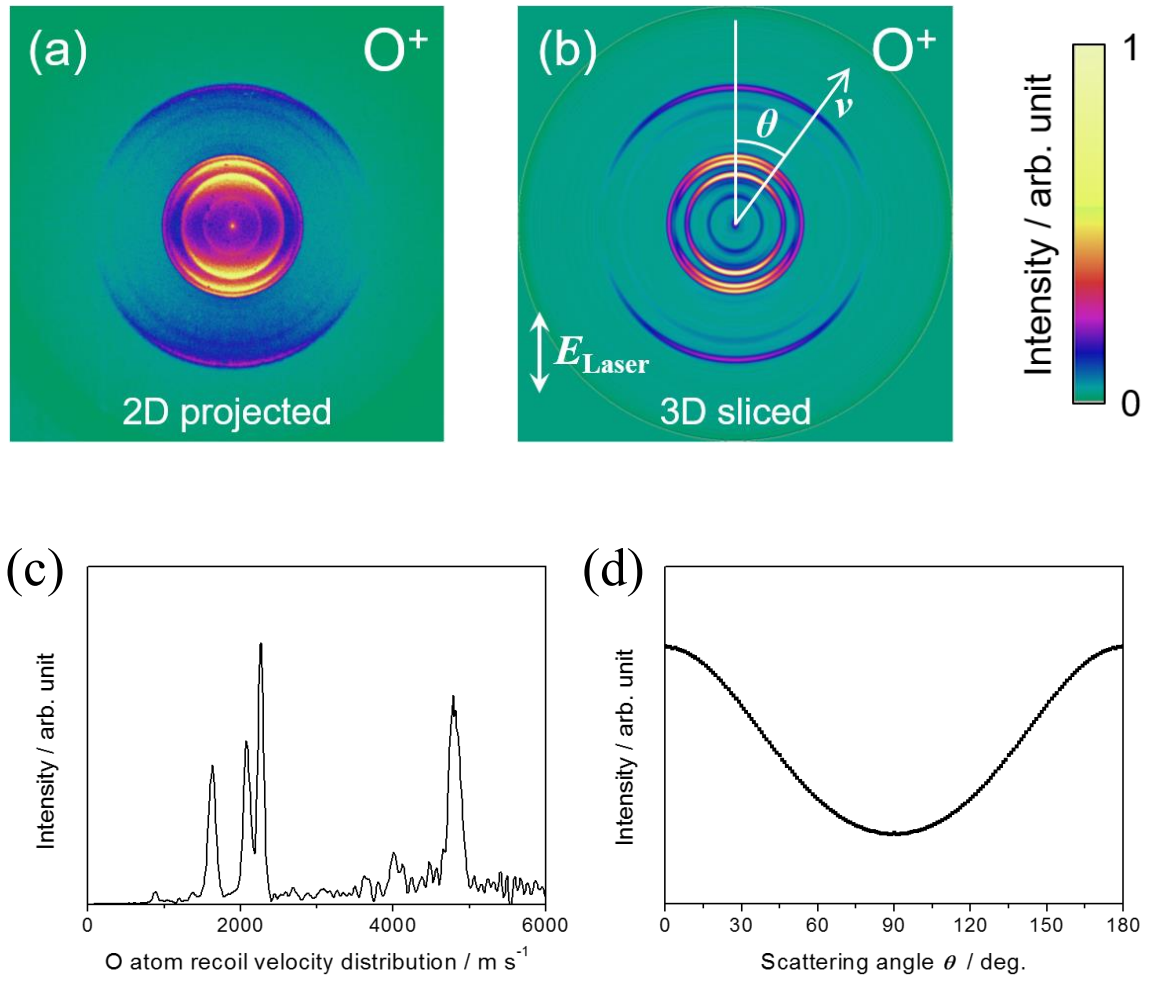

Figure 2.6 Reconstruction from (a) the 2D projection image to (b) the 3D slice image of atomic oxygen ions by pBasex. (c) The recoil velocity and (d) the scattering angle distributions were extracted from the 3D slice image of atomic oxygen ions.

A 3D slice image includes information of the recoil velocity, v, and the scattering angle, θ, of the photofragment. The distance from the center point in the 3D slice image is proportional to v, which reflects the dissociation process of the parent molecule. The radial scale of the 3D image can be calibrated by using scattering image of the same photofragment generated through a well-

known dissociation process. For the calibration, the photodissociation producing an atom as the counter-product is favorably selected because on the basis of the energy conservation law (explained below) the observed photofragment has only a few kinds of recoil velocities due to the simple internal state structure of the counter-produced atom. The θ with respect to the direction of the photolysis laser polarization gives rich information concerning an electronic character; an angle between a transition dipole moment and a dissociating direction, and the dissociation lifetime of the parent molecule. Figure 2.6 shows (c) the recoil velocity and (d) angular distributions extracted from (b) the 3D sliced image of O^+.

On the basis of the linear momentum conservation law, the recoil velocity of a target photoproduct, v_P, is correlated with that of the counter-photoproduct, v_{CP}, by the relation, $m_P v_P = m_{CP} v_{CP}$, where m_P and m_{CP} are mass of a target photoproduct and the counter-photoproduct, respectively. Figure 2.7 shows the recoil velocities of photoproducts. One can determine the total kinetic energy, E_{trans}, by summing kinetic energies of both photoproducts, $m_P v_P^2/2$ and $m_{CP} v_{CP}^2/2$. In addition, the internal energy of the counter-photoproduct, E_{int}^{CP}, can be determined on the basis of the energy conservation law,

$$E_{int}^{CP} = h\upsilon - D_0 - E_{trans} - E_{int}^{P} \qquad (2.1)$$

where $h\upsilon$ is the photon energy of a photolysis laser, D_0 is the bond dissociation energy, and E_{int}^{P} is an internal energy of a target photoproduct, as shown in Figure 2.8. Since the probe laser ionizes a target photoproduct state-selectively by REMPI method, the E_{int}^{P} is a fixed value. Therefore, the E_{int}^{CP} distribution can be obtained from observed E_{trans} distribution.

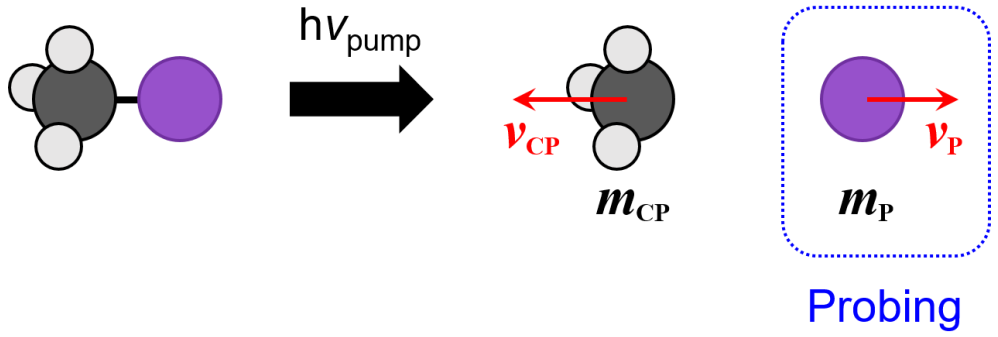

Figure 2.7 Recoil velocities, v_P and v_{CP}, of the photofragments; the v_P indicates the recoil velocity of the photofragment probed by the laser and the v_{CP} indicates the recoil velocity of the counter-photoproduct.

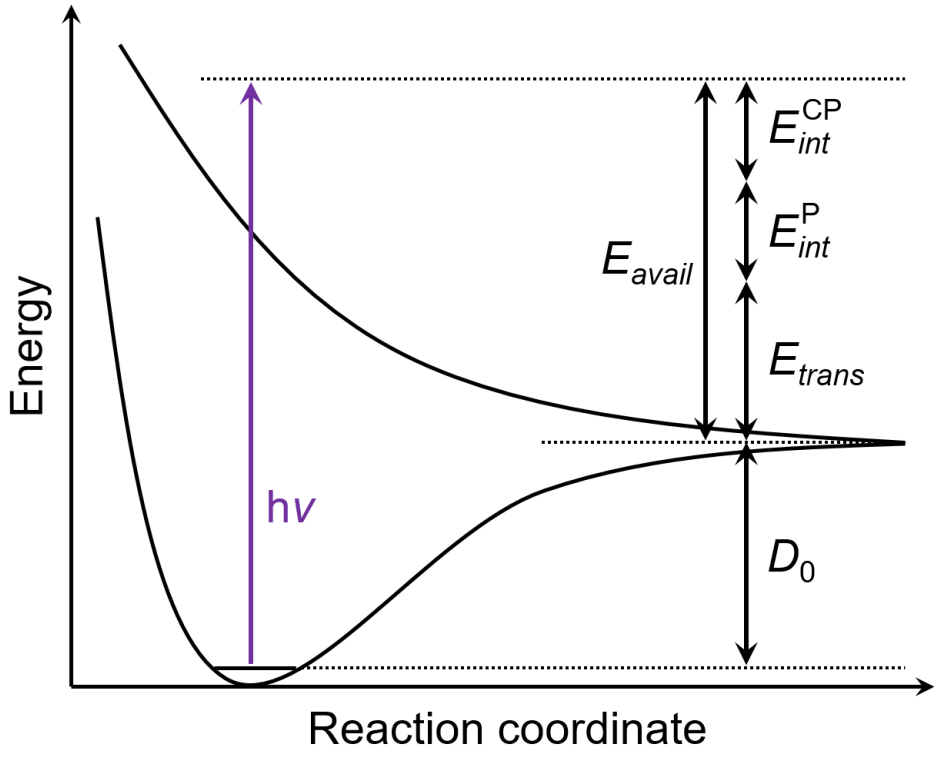

Figure 2.8 Energy conservation in the photodissociation. The term of E_{avail} indicates the available energy, defined as $E_{avail} = h\nu - D_0$.

One can determine an anisotropy parameter, β ($-1 \leq \beta \leq 2$), by fitting the standard formula for one-photon photodissociation with the Legendre polynomial, $P_2(\cos\theta)$,

$$\frac{\partial\sigma}{\partial\Omega}(\theta) = \frac{\sigma}{4\pi}\left(1 + \beta P_2(\cos\theta)\right), \tag{2.2}$$

to observed angular distribution, where θ is the scattering angle and σ is the integral cross section. When the transition dipole moment lies parallel to the dissociating bond and the dissociation lifetime is far shorter than the rotational period, $\beta = 2$ and Eq. (2.2) leads to $\cos^2\theta$. Similarly, when the transition dipole moment lies perpendicular to the dissociating bond, $\beta = -1$ and Eq. (2.2) leads to $\sin^2\theta$. If the dissociation lifetime is sufficiently longer than the rotational period, the parent molecule would rotate a number of times before breaking up, the memory of the photoexcitation process would be completely lost. In this case, the photofragment scatters isotropically, and $\beta = 0$.

2.2.3 LIF Spectroscopy

Laser-induced fluorescence (LIF) spectroscopy is widely utilized for the reaction dynamics experiments as well as REMPI spectroscopy due to the high sensitivity and high selectivity. Figure 2.9 shows the principle of LIF spectroscopy. The probe laser photon resonantly excites a target molecule in the populated state. The excited molecule emits fluorescence with own specific lifetime and is quenched to the electronic ground state. By scanning the probe laser wavelength while detecting the fluorescence, one can observe a rovibrational spectrum of the target molecule. Since the peak intensity is proportional to the original population of the lower state, observed spectrum can be transformed into the rovibrational state distributions of the nascent photofragments.

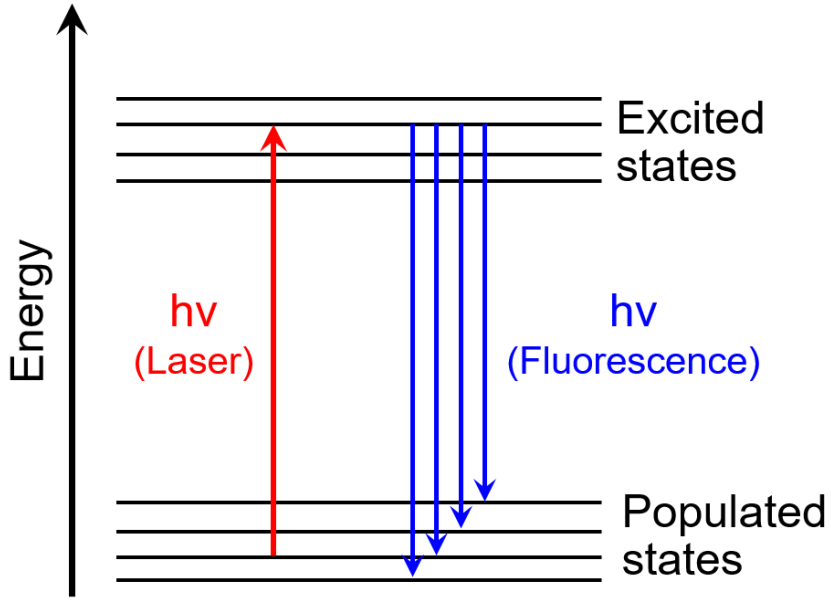

Figure 2.9 Principle of LIF spectroscopy

Chapter 3.

Photodissociation Dynamics of Allyl Iodide in the Near-Ultraviolet Region

3.1 Introduction

Competition between several reaction mechanisms that branch to different product pathways is an important issue in the photodissociation of polyatomic molecules. For polyatomic molecules that contain more than one functional group, the dissociation mechanism and the pathways can largely depend on the photoabsorption, since a certain absorption band might be responsible for the local excitation of one part of the molecule as a concept of chromophore. It is considered that a nascent repulsive force due to an anti-bonding orbital involved in the photoexcitation is exerted on a different moiety at each photolysis wavelength. However, since the photoenergized parts of the molecule and the subsequent dynamics may not in reality be completely localized within an individual group, the occurrence of site-selective photodissociation dynamics should be carefully verified by comparing the different absorption bands. Allyl iodide (C_3H_5I), which consists of a halogen (−I) and an allyl ($-C_3H_5$) group, is an appropriate molecule to corroborate the relationship between the photoabsorption property and the photochemical mechanism. Allyl iodide has several dissociative absorption bands in the ultraviolet (UV) region and the electronic character of these were simply interpreted in terms of the local symmetry of the molecular orbitals in previous spectroscopic studies.[9, 10]

The UV absorption spectrum of C_3H_5I in the relatively short wavelength region (140-250 nm) was measured by Worrell.[9] Three peaks at 173 nm, 188 nm and 201 nm were identified as having the electronic excited states with an electron promoted to the π^*_{CC} orbital. The 173-nm band was characterized as the $\pi_{CC}\pi^*_{CC}$ transition, and the 188-nm and 201-nm bands were ascribed to the electronic promotion from the non-bonding 5*p*-orbitals of the iodine atom

(n_I) on the basis of the one-electron molecular orbital model. Quantum chemistry calculations based on the configuration interaction method reported by Parsons *et al.*[11] indicated the dominant contribution of a mixture of the $\pi_{CC}/n_I \rightarrow \sigma^*_{C-I}/\pi^*_{CC}$ and the $\pi_{CC} \rightarrow$ Rydberg configurations to the excited states near 200 nm. This *ab initio* calculation showed that two electronic excited states with the similar electronic characters were responsible for the photoabsorption at approximately 200 nm. The lower state was related to a weak band observed as a shoulder on the 201-nm band by Boschi and Salahub;[10] before the *ab initio* calculation, the shoulder structure at approximately 215 nm was assigned to $n_I\pi^*_{CC}$. The UV spectra observed by Boschi and Salahub for the longer wavelength region showed a further weaker band at 270 nm, which was assigned to the $n_I\sigma^*_{C-I}$ transition in the systematic analyses of a series of iodine-containing hydrocarbons.[10] The near-UV spectra observed by Jenkin *et al.* is shown in Figure 3.1, wherein the absolute absorption cross section of the longest band (270-nm band) of C_3H_5I was measured to be 2.42×10^{-18} cm^2 at the maximum (269.1 nm).[12, 13]

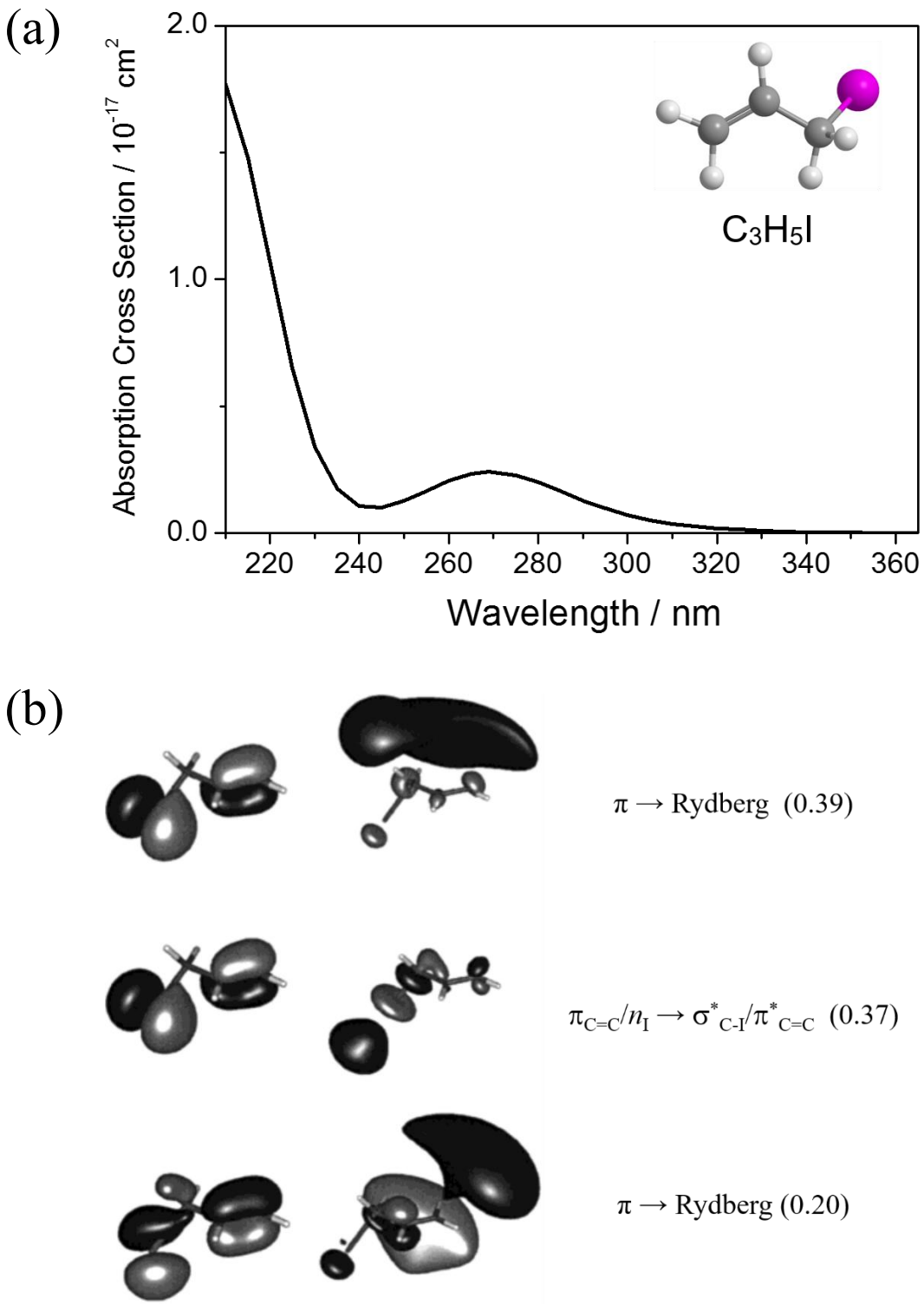

Figure 3.1 (a)The near-UV absorption spectra of allyl iodide at room temperature measured by Jenkin *et al.* (Refs. 12 and 13). (b) Electronic configurations corresponding to bright states near 200 nm calculated by Parsons *et al.* (Ref. 11). The numerical values in brackets indicate the relative proportions of the transitions.

The photodissociation dynamics of C_3H_5I have been investigated experimentally at several photolysis wavelengths in the gas phase. Time-resolved spectroscopy was applied by Baklanov *et al.* to obtain the lifetimes at 355 nm,[14] 159 -166 nm,[15] 700 nm,[14] and 600 nm[16] regions. For the latter two in the visible region, the C−H overtone excitation to the v_{CH} = 5 and 6 vibrational states was used to dissociate C_3H_5I in the electronic ground state. The initial nuclear motions following the photoabsorption were examined by emission spectroscopy at 199.7 nm[11] and 225-241 nm.[17, 18] The emission spectra in the photodissociation at 199.7 nm was analyzed by comparison with the results of an *ab initio* calculation. Since the excitation of neither the C−C=C torsion nor the C−I stretching vibrational mode was observed in the emission spectrum during the dissociation of C_3H_5I to C_3H_5 + I, it was concluded that the mechanism of C−I bond fission is not direct dissociation on the excited-state potential energy surface but rather inclusion of curve crossing or predissociation.[11] Detailed dynamics studies by translational spectroscopy and ion-imaging[19-21] were conducted for the photodissociation at 193 nm. One of the subjects intensively discussed in the studies at 193 nm was the stability of the allyl radical (C_3H_5) produced by the photodissociation of C_3H_5I, perhaps due to the importance of C_3H_5 as an intermediate in a variety of chemical processes. The pyrolysis of C_3H_5I is widely used as an efficient source for a cold C_3H_5 radical beam for use in spectroscopy, unimolecular and bimolecular reactions.[22-26] While in the photolysis, Szpunar *et al.* found that, although the nascent internal energy of the C_3H_5 photoproduct at 193 nm is high enough to overcome the reaction barrier to the C_3H_4 + H decomposition (secondary dissociation), loss of an atomic hydrogen occurs inefficiently.[21] The stability of the internally hot C_3H_5 radical

was explained to be due to the large energy partitioning to the rotation, which suppresses the unimolecular decomposition as a centrifugal effect.[27] The stability of the allyl radical generated at 193 nm was further investigated by isotopic substitution[20] and ion-imaging.[19]

The branching ratio between the $^2P_{1/2}$ and $^2P_{3/2}$ spin-orbit states of an atomic halogen photoproduct is another important topic in the photodissociation dynamics of polyatomic halides. Since the large spin-orbit splitting of an atomic iodine (0.94 eV)[28] is comparable to the bond dissociation energy of C_3H_5I to C_3H_5 + I (1.95 eV),[29] the spin-orbit branching mechanism is closely related to the C−I bond dissociation. From an experimental viewpoint, the determination of the spin-orbit branching ratio requires careful measurements, especially when resonantly-enhanced multiphoton ionization (REMPI) spectroscopy is applied. The experimental problems and the importance of the spin-orbit branching ratio were discussed by Fan and Pratt in the photodissociation study of a series of halogenated hydrocarbons.[19, 30] They applied two methods based on ionization detection by vacuum ultraviolet spectroscopy as complementary approaches to REMPI and translational spectroscopy. Their careful comparison and calibration yielded the fractions of $I^*(^2P_{1/2})$ to be 0.61 and 0.90 with respect to the total I photofragment ($I(^2P_{3/2}) + I^*(^2P_{1/2})$) in the photodissociation of C_3H_5I at 193 nm and 266 nm, respectively.[19, 30]

In this Chapter, I present the REMPI spectra and the spin-orbit state-resolved scattering distributions of the I fragment generated by the photodissociation of C_3H_5I at 266 nm and 213 nm. These two photolysis wavelengths are located in the lowest and next-lowest absorption bands.[9, 12, 31] The reaction dynamics, which show a site-selective photochemistry, are discussed along

with the electronic characterization from a photochemical viewpoint.

3.2 Experimental

The experimental apparatus and laser setup were explained in Section 2.1 in detail. The gas sample, prepared by seeding 0.1% of allyl iodide in a He buffer, was used at a stagnation pressure of 2 atm. The fourth (266 nm) and the fifth (213 nm) harmonics of the output of a Nd:YAG laser were employed for the photolysis. A wavelength of 266 nm is located at the peak of 270-nm band, while 213 nm is located at the middle of the next shorter band, which appeared as a shoulder of the stronger 201-nm band in the UV spectrum. The photoabsorption cross section at 213 nm is seven times larger than that at 266 nm, as shown in Figure 3.1.

The atomic iodine photofragments, I($^2P_{3/2}$) and I*($^2P_{1/2}$), were state-selectively ionized by [2+1] REMPI spectroscopy with the $6p \leftarrow 5p$ two-photon resonance transitions in the 303-307 nm region. The REMPI spectra were measured with a Daly detector, the output of which was fed into a gated integrator (SR250, SRS). The pulse energies of the pump and probe laser were monitored with a photodiode to keep them sufficiently constant in a measurement. For determination of the relative yields of the I($^2P_{3/2}$) and I*($^2P_{1/2}$) photofragments, the signal intensities at the neighboring four lines (304.672 nm for I($^2P_{3/2}$) and 304.024, 305.569, and 306.729 nm for I*($^2P_{1/2}$)) were measured six times until the variation of the relative intensity was less than 10%. For measurement of the state-resolved scattering distribution, I replaced the Daly detector by a MCP detector at the same position. The resonant lines at 304.672 nm (($^3P_2$)$6p$ $^2[3]_{5/2} \leftarrow 5p$ $^2P_{3/2}$) and 304.024 nm (($^3P_1$)$6p$ $^2[1]_{1/2} \leftarrow 5p$ $^2P_{1/2}$) were used for I($^2P_{3/2}$) and I*($^2P_{1/2}$) detection, respectively. These lines were chosen because they were the strongest of the lines with the common lower

states (I($^2P_{3/2}$) or I*($^2P_{1/2}$)). I confirmed the identical scattering images to be observed using different resonant lines but with the same lower states. The probe laser wavelength was repetitively scanned over the Doppler width of the photofragment atomic line as the line profile and the images were recorded. The velocity scale of these images was calibrated by comparison with the images for the photodissociation of methyl iodide at 266 nm[32] under the same detection condition.

Three dimensional velocity and angular distributions for the photofragments were reconstructed from the observed projection images by the Abel inversion after fitting them with pBasex method. The basis functions used to fit the raw images were 200 Gaussian type radial functions that are equally separated with a half width at half maximum of 2 pixels and angular functions of the Legendre polynomials up to the fourth order. By the use of these continuous and well-behaved functions, the numerical noise in the Abel inversion was much reduced and the accuracy in the background subtraction was improved.

The I*($^2P_{1/2}$) images at both photolysis wavelengths contained hardly any one-color (pump-only or probe-only) signal, whereas a small amount of intensity (9% at 266 nm and 17% at 213 nm) in the I($^2P_{3/2}$) images was observed as background noise due to the use of the 304-nm probe laser. The signal-to-noise ratios were seemingly inconsistent with the absorption intensities at room temperature shown in Figure 3.1. This can be partly ascribed to the two conformers (*cis*- and *gauche*-allyl iodide) at room temperature and reduction of the dissociation quantum yield by photoemission process.[11] Under the

present molecular beam condition, I surely assumed that the *gauche*-allyl iodide was exclusively dominant in the sample. Subtraction of the probe-only data from the pump-probe data did not significantly alter the velocity and angular distributions for the 266-nm photolysis. In addition, the ion-imaging measurement for the 266-nm photolysis but with a different detection wavelength of [2+1] REMPI with the $7p\ ^2D_{3/2} \leftarrow 5p\ ^2P_{3/2}$ resonance showed the identical results for the I($^2P_{3/2}$) products to those with the $6p\ ^2D_{3/2} \leftarrow 5p\ ^2P_{3/2}$ resonance at 304 nm. These results confirmed that unwanted multiphoton processes induced by the 304-nm light were negligible in the I($^2P_{3/2}$) data at 266 nm for the subsequent analysis. However, the I($^2P_{3/2}$) image data at 213 nm required more careful treatment, since the one-color signal due to the 304-nm light overlapped the characteristic features of the I($^2P_{3/2}$) image at the 213-nm photolysis. The analysis of the scattering data for the I($^2P_{3/2}$) image at 213 nm is discussed in more detail in a later section.

3.3 Result and Discussion

3.3.1 The Branching Ratio of the Spin-Orbit States

The REMPI spectra of the iodine fragments at 266 nm and 213 nm are shown in Figure 3.2. The relative populations of the spin-orbit states, $N(^2P_{1/2})$ and $N(^2P_{3/2})$, are in principle obtained from the observed spectral intensity. However, as discussed by Fan and Pratt,[19, 30] precise determination of the spin-orbit state branching ratio from the multi-photon spectrum requires careful analysis. I adopted the procedure for determining the spin-orbit branching ratio $\Phi^* = N(^2P_{1/2})/(N(^2P_{1/2}) + N(^2P_{3/2}))$ used by Eppink and Parker in the CH_3I photodissociation study.[32] The REMPI spectra of the iodine photofragments at 266-nm photodissociation of CH_3I were also measured under the same probe laser conditions as that for C_3H_5I for reference. Using the reference value of Φ^* = 0.73 of the CH_3I photodissociation at 266 nm,[33, 34] the detection efficiency of the atomic lines were calibrated, and then the relative $N(^2P_{1/2})$ and $N(^2P_{3/2})$ of the C_3H_5I photodissociation were determined from the observed REMPI spectra. The experimental error for $N(^2P_{1/2})$ and $N(^2P_{3/2})$ was evaluated from the variation of the observed intensity at the three atomic lines having the lower state of $I^*(^2P_{1/2})$, the ratio of which would be constant in an ideal measurement. The Φ^* values determined in this manner for C_3H_5I were 0.83 (0.08) and 0.78 (0.10) for 266-nm and 213-nm photolysis, respectively. The Φ^* values are shown in Table 3.1 together with the Φ^* data for other iodides for the sake of comparison.

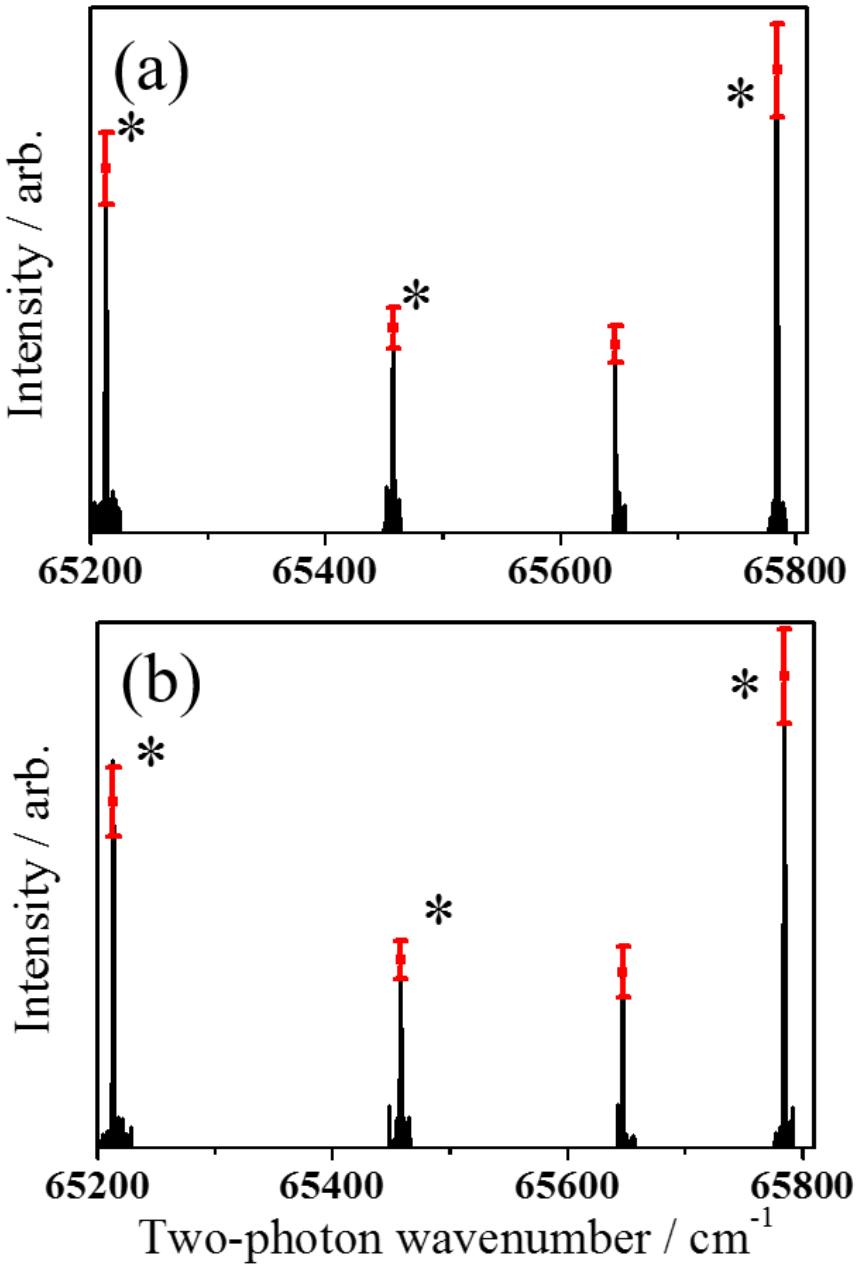

Figure 3.2 The REMPI spectra of the atomic iodine produced in the photodissociation of C_3H_5I at the photolysis wavelength of (a) 213 nm and (b) 266 nm. An asterisk indicates the line associated to the spin-orbit excited state $I^*(^2P_{1/2})$.

The present measurement yielded large Φ^* values (approximately 80 %) for both of the two UV bands. The Φ^* value at 266 nm is consistent with the result measured by Fan and Pratt ($\Phi^* = 0.90 \pm 0.10$),[30] and the Φ^* value at 213 nm is perceptibly larger than the $\Phi^* = 0.61$ at 193 nm,[30] which belongs to the higher absorption band. The dominance of the energetically unfavorable $C_3H_5 + I^*(^2P_{1/2})$ pathway indicates that the adiabatic state-correlation substantially remains from the Franck−Condon region to the product asymptotes. The Φ^* value may be given by the photoabsorption cross sections to electronic excited states and the non-adiabatic transition probability between those electronic states if the electronic excited states are well correlated to the asymptotic product states ($C_3H_5 + I(^2P_{3/2})$, $C_3H_5 + I^*(^2P_{1/2})$). This is the case for CH_3I and the larger alkyl iodides ($C_nH_{2n+1}I$),[35-39] to which Mulliken's analysis[40, 41] has been widely applied to understand the electronic state-correlation in numerous studies for the so-called A-band photodissociation. The A-band of the alkyl iodides, which is commonly located at around 270 nm, is well characterized to be an apparently single absorption band with contributions from three electronic excited states with $n_I\sigma^*_{C-I}$ character (designated as $^1Q_1$, $^3Q_1$, and $^3Q_0$ by Mulliken's notation). The $^1Q_1$ and $^3Q_1$ states adiabatically correlate to the $I(^2P_{3/2})$ channel and the $^3Q_0$ state correlates to the $I^*(^2P_{1/2})$ channel. The large Φ^* value for CH_3I (0.73), which is the simplest C−I single bond system, was experimentally corroborated by Eppink and Parker[32] as a result of the large absorption cross section of $^3Q_0$. Other alkyl iodides also have large Φ^* values in the photodissociation around the 270-nm region as shown in Table 3.1, and this indicates that preferential $I^*(^2P_{1/2})$ production is a common electronic feature of the A-band in saturated iodides. In contrast, cyclic and aromatic iodides

exhibit small Φ^* values in the 270-nm region. The small Φ^* value for C_2H_3I (0.27) and C_6H_5I (0.32) are considered to be due to significant mixing of the π orbital and the σ_{C-I} orbital around the alpha carbon atom, which may collapse the adiabatic correlation as the C−I bond elongation. Although allyl iodide has an unsaturated π system, the Φ^* observed at 266 nm is as large as those of alkyl (non-π) iodides. This finding implies that the photochemical process is localized in the C−I bond and shows the typical A-band property of alkyl iodides.

Table 3.1 Spin-orbit branching ratio (Φ^*) of iodides. Errors of other species than C_3H_5I are omitted.

$\lambda_{photolysis}$	C_3H_5I	CH_3I	C_2H_5I	C_3H_7I	C_4H_7I	C_2H_3I	C_6H_5I	$C_6H_{11}I$
266 nm	0.83 ± 0.08[a]	0.73[b]	0.67[c]	0.6[d]	0.61[c]	0.27[f]	0.32[g]	0.22[h]
	0.90 ± 0.10[i]		0.7[d]					
213 nm	0.78 ± 0.10[a]							
193 nm	0.61 ± 0.10[i]					0.435[f]		

[a]This work.
[b]Reference 32. Other values of 0.71, 0.75, 0.76 are also reported.
[c]Reference 38 at 267 nm.
[d]Reference 35.
[e]Reference 39 at 277 nm.
[f]Reference 42.
[g]Reference 43. Other values of 0.35 and 0.51 are also reported.
[h]Reference 37.
[i]Reference 30.

While the Φ^* value observed in the 270-nm band is qualitatively understood by a C−I bond model, as discussed above, the preference of the C_3H_5 + $I^*(^2P_{1/2})$ pathway in the 215-nm band was not analyzed as well since I do not readily assume the isolation of the π-system (allyl framework) from the C−I bond for higher electronic states than that associated with the A-band ($n_I\sigma^*_{C-I}$ states). The quantum chemistry calculation carried out by Parsons *et al.* predicted two excited states near 200 nm, both of which contain the $\pi_{CC}/n_I \rightarrow \sigma^*_{C-I}/\pi^*_{CC}$ mixed character.[11] It is considered that a large deformation of the allyl framework due to the photoabsorption involving the π_{CC} and π^*_{CC} orbitals obscures the product state-correlation, resulting in small Φ^* values.[42-44] If the electronic correlation from the photoexcitation region to the product asymptotes is completely lost, the scrambling would give $\Phi^* = 0.33$, which is the ratio of the degeneracy. The $\Phi^* = 0.78$ observed at 213 nm is considerably larger than the expected value. Although a small difference in the Φ^* values between the 215-nm band (0.78 at 213 nm) and the higher 201-nm band (0.61 at 193 nm)[30] is not fully explained, the large Φ^* in the 215-nm band at least indicates that the adiabatic correlation remains between the excited state involving the π^*_{CC} orbital in the Franck−Condon region and the product asymptotes.

3.3.2 Scattering Distributions of $I^*(^2P_{3/2})$ and $I(^2P_{1/2})$ Products

3.3.2.1 266-nm Photodissociation

The scattering images of the $I(^2P_{3/2})$ and $I^*(^2P_{1/2})$ products are shown in Figure 3.3: (a) $I(^2P_{3/2})$ and (b) $I^*(^2P_{1/2})$ at 226 nm, and (c) $I(^2P_{3/2})$ and (d) $I^*(^2P_{1/2})$ at 213 nm. These four images displayed similar angular distributions, while the velocity distributions were sensitively dependent both on the product states and the photolysis wavelengths. The center-of-mass translational energy distribution, $P(E_{trans})$, obtained from the velocity distribution at 266 nm is shown in Figure 3.4 (a), wherein all the angular components were summed. The $P(E_{trans})$ of $I^*(^2P_{1/2})$ consisted of a single narrow component that peaked at E_{trans} = 1.1 eV (Figure 3.4 (a), red). The $P(E_{trans})$ of $I(^2P_{3/2})$ showed a relatively broad peak with a shoulder (Figure 3.4 (a), black). The structured peak was decomposed to two Gaussian functions and the low and high E_{trans} components yielded average $\langle E_{trans} \rangle$ values of 0.90 eV and 1.49 eV, respectively. The ratio of these two components was slow:fast = 3:7. As explained in Section 2.2.2.2, the internal energy of the allyl radical, $E_{int}(C_3H_5)$, can be determined from the total translational energy by using the energy conservation relation as shown: $E_{int}(C_3H_5) = h\nu - D(C_3H_5{-}I) - E_{int}(I) - E_{trans}$, where $h\nu$ is the dissociation photon energy, $D(C_3H_5{-}I)$ is the bond dissociation energy (1.95 eV) evaluated from the thermodynamics data,[29] and $E_{int}(I)$ is the spin-orbit energy of the I atom ($^2P_{3/2}$: 0 eV, $^2P_{1/2}$: 0.94 eV).[28] The $E_{int}(C_3H_5)$ distribution resolved in each spin-orbit product channel is shown in Figure 3.4 (b). For a guide of the internal energy scale, the vibrational levels of typical vibrational modes, the first electronic excite state,[45] and the barrier height for decomposition[21, 46] were su-

perimposed. Corresponding to the bimodal $P(E_{trans})$, the C_3H_5 radical co-produced with $I(^2P_{3/2})$ was found to have relatively hot ($<E_{int}(C_3H_5)> = 1.22$ eV) and cold ($<E_{int}(C_3H_5)> = 1.81$ eV) components. The energetics are summarized in Table 3.2.

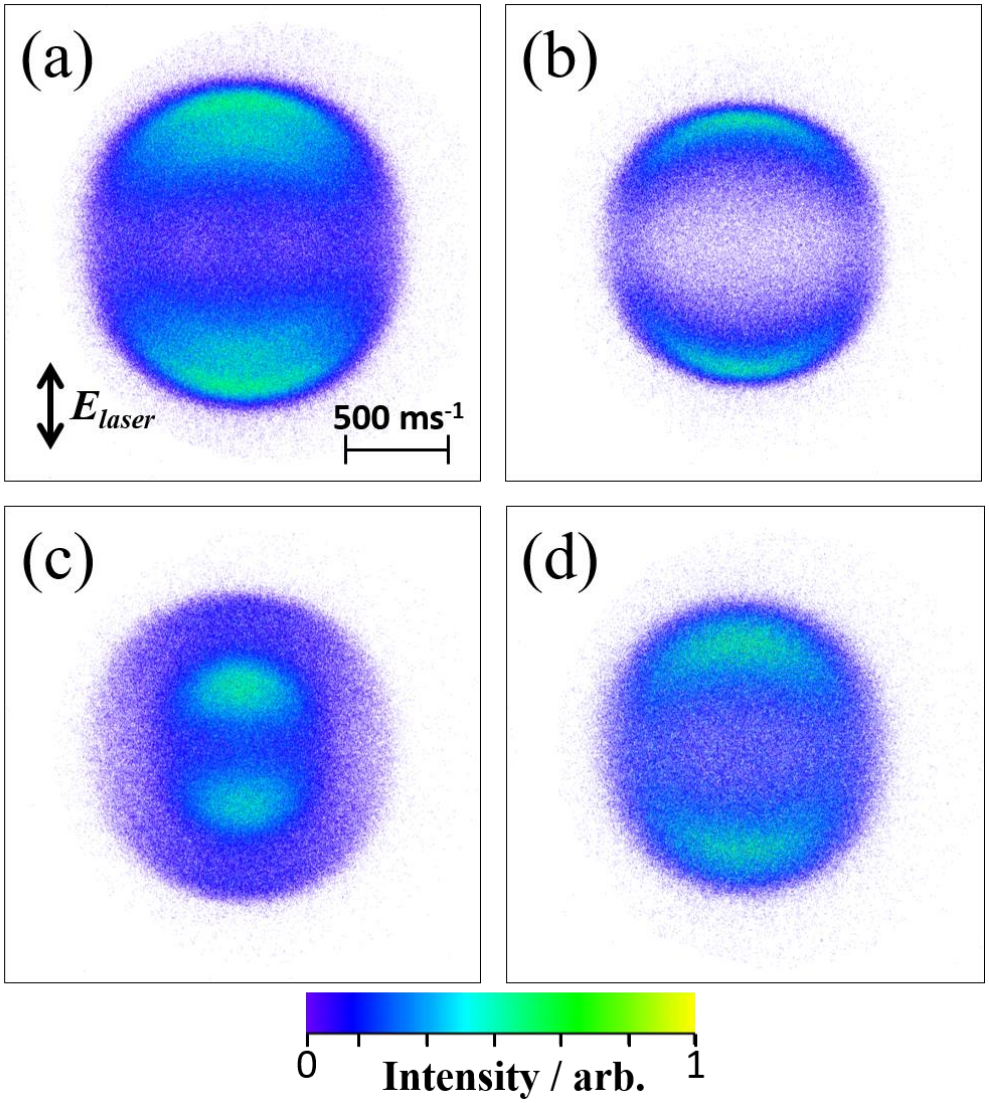

Figure 3.3 The observed scattering raw images of the iodine product from the C_3H_5I photolysis: (a) the $I(^2P_{3/2})$ and (b) the $I^*(^2P_{1/2})$ spin-orbit states at the photolysis wavelength of 266 nm, and (c) the $I(^2P_{3/2})$ and (d) the $I^*(^2P_{1/2})$ spin-orbit states at the photolysis wavelength of 213 nm. The laser polarization axis is vertical on the figures.

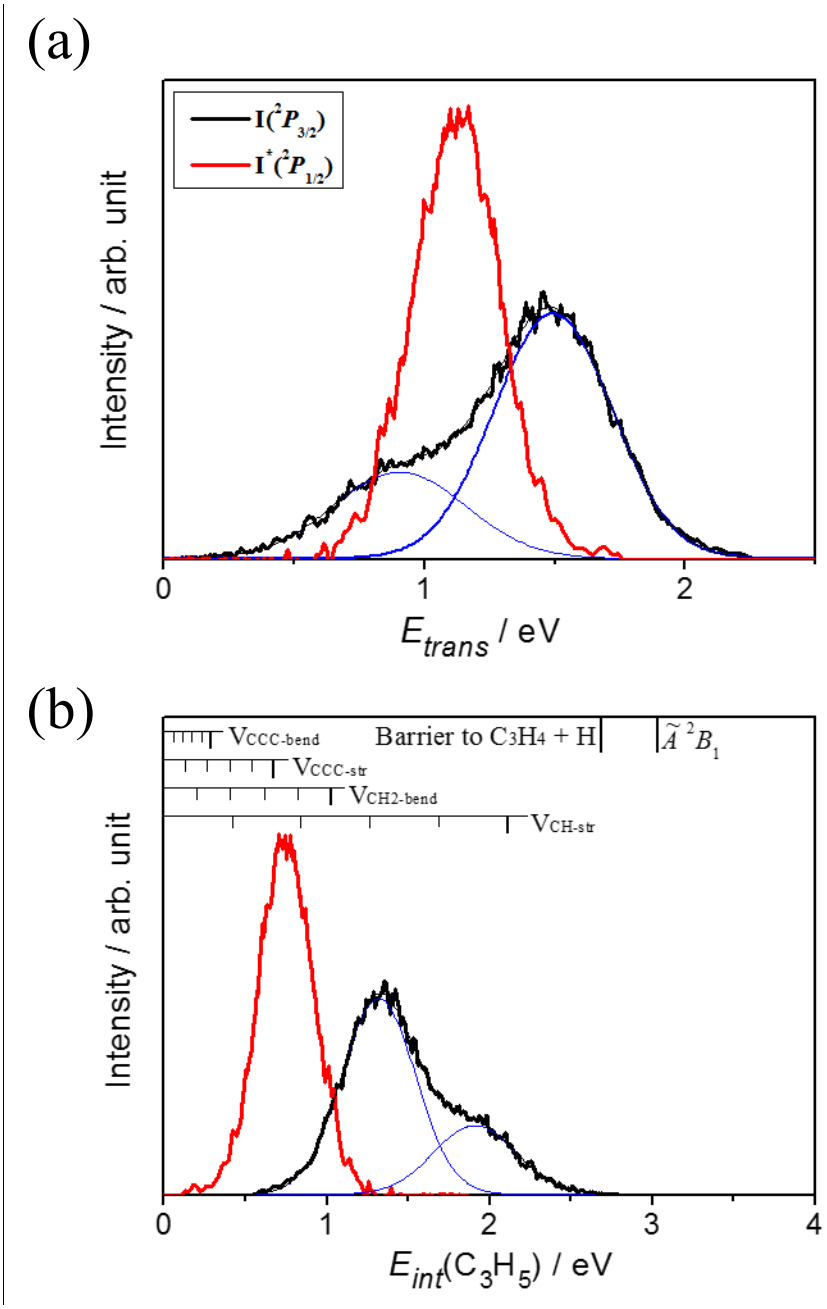

Figure 3.4 (a) The center-of-mass translational energy distribution of the C_3H_5I photolysis at the photolysis wavelength of 266 nm. (b) The internal energy distribution of the C_3H_5 counter-product. The data of $I(^2P_{3/2})$ and $I^*(^2P_{1/2})$ are shown by black and red lines, respectively. The blue lines show the two Gaussian functions fitted to the observed data of the $I(^2P_{3/2})$ state for decomposition. The intensity is normalized so that the data of the $I(^2P_{3/2})$ and $I^*(^2P_{1/2})$ channels have the same area intensity.

Table 3.2 Energy partitioning of the C_3H_5I photodissociation.

$\lambda_{photolysis}$	Channel	Component	$\langle E_{trans} \rangle$ (eV)	f_{trans}	$\langle E_{int}(C_3H_5) \rangle$ (eV)
266 nm	$I(^2P_{3/2})$	Fast	1.49	0.55	1.22
		Slow	0.90	0.33	1.81
	$I^*(^2P_{1/2})$	(Single)	1.12	0.41	0.65
213 nm	$I(^2P_{3/2})$	Fast	1.12	0.29	2.76
		Slow	0.41	0.11	3.47
	$I^*(^2P_{1/2})$	(Single)	0.96	0.25	1.98

The spin-orbit state dependence of the $P(E_{trans})$ similar to that observed in the present measurement was also seen in other allyl halides; the bimodal $P(E_{trans})$ of the spin-orbit ground state ($^2P_{3/2}$) channel and the singly peaked $P(E_{trans})$ of the spin-orbit excited state ($^2P_{1/2}$) channel were observed in the photodissociation studies of C_3H_5Br at 234 - 267 nm[47] and C_3H_5Cl at 235 nm.[48] The differences in the E_{trans} values for the two peaks in the $^2P_{3/2}$ channel are 0.51 - 0.77 eV for C_3H_5Br and 1.05 eV for C_3H_5Cl. The intensity ratio of the slower halogen products (Br and Cl) to the fast one was less than 10 % in both the allyl halides. Although an analogy can be seen in the spin-orbit state-resolve $P(E_{trans})$ of the halogen atom elimination of the $C_3H_5{-}X$ (X = Cl, Br, and I) photodissociation, a unified interpretation is not quantitatively accurate because of the different excited-state property of each allyl halide. In these studies for C_3H_5Br and C_3H_5Cl, the two components in the $X(^2P_{3/2})$ channel were attributed to the different mechanisms,[47, 48] namely predissociation to the lower repulsive states and internal conversion to the ground states, wherein the initial photoabsorption was assumed to involve the $\pi_{CC}\pi^*_{CC}$ transition. However, the

270-nm band of C_3H_5I is well separated from the shorter wavelength bands, which plausibly have a large $\pi_{CC}\pi^*_{CC}$ character. The band at around 270 nm is a common feature of alkyl- and alkenyl-iodides[10, 49] and it is assigned to composite electronic transitions with a $n_I\sigma^*_{C-I}$ character (the ground state → the $^1Q_1$, $^3Q_1$ and $^3Q_0$ states). By simply applying Mulliken's model to the present data, it is considered that the simultaneously photoinitiated $^1Q_1$ and $^3Q_1$ potential energy surfaces that are correlated with the I($^2P_{3/2}$) channel can produce C_3H_5 with different $E_{int}(C_3H_5)$ distribution due to each surface structure, leading to the two peaks in the $P(E_{trans})$ of the I($^2P_{3/2}$) fragments, as shown in Figure 3.5. The I*($^2P_{1/2}$) channel would be correlated from a single repulsive $^3Q_0$ surface in a hypothetical $n_I\sigma^*_{C-I}$ transition at 266 nm, possibly yielding a singly peaked $P(E_{trans})$. This discussion requires more quantitative bases such as absorption cross section, vertical energy, and adiabaticity for the $^{1,3}Q_{0,1}$ states. However, the fact that the $n_X\sigma^*_{C-X}$ character of the first excited state increases with the heavier halogens due to the increased n_X orbital energy gives us a qualitative explanation. This halogen-dependence found in the A-band studies of allyl[9] and vinyl halides[42] indicates that the photochemistry of C_3H_5I at 266 nm is more reasonably understood by dissociative absorption in the C−I bond rather than considering the π_{CC} (or π^*_{CC}) orbital as in the C_3H_5Br and C_3H_5Cl photodissociation.[47, 48]

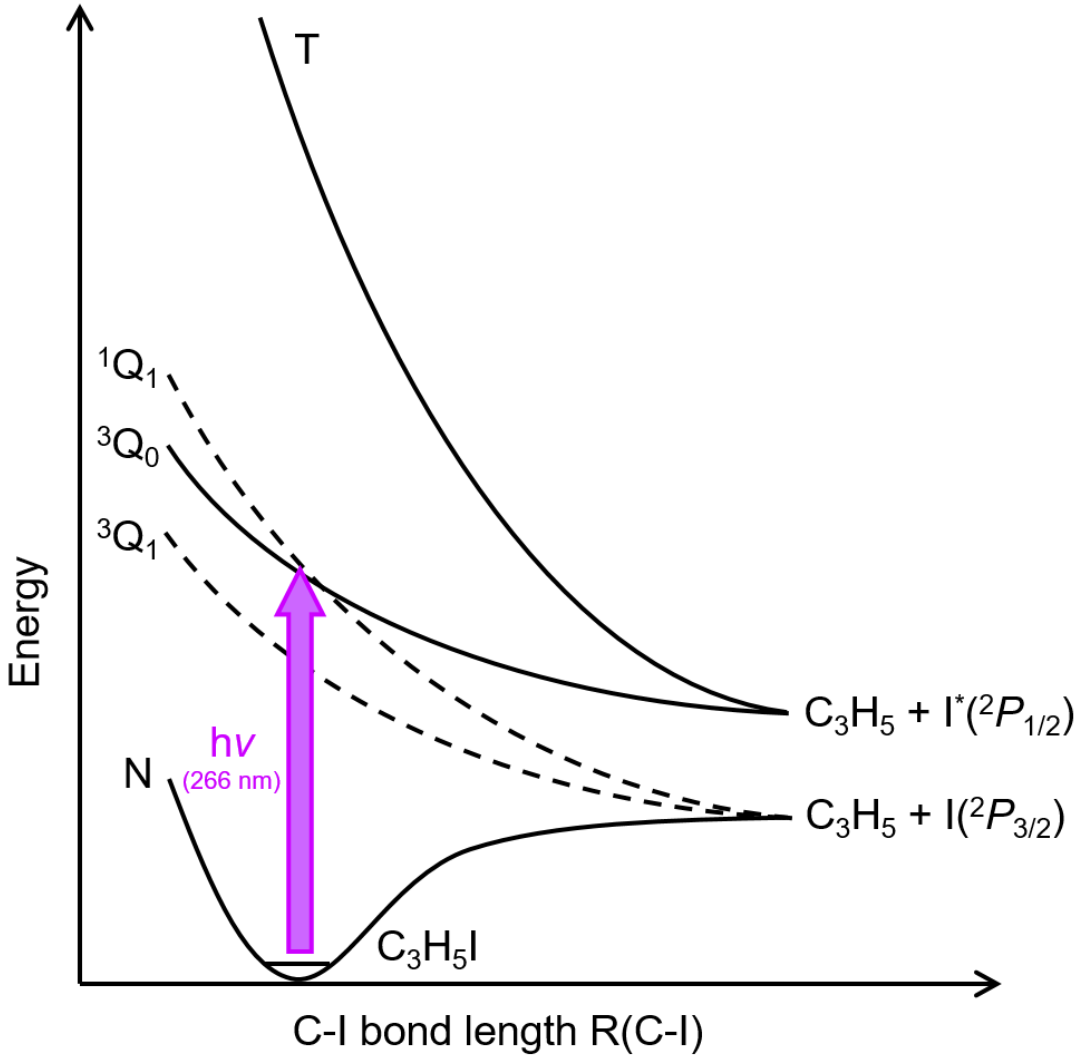

Figure 3.5 Schematic view of the electronic transition in the 270 nm band represented by simply applying Mulliken's notation. $^3Q_0$ and T states corresponding to $I^*(^2P_{1/2})$ channel represent solid lines, while $^{3,1}Q_1$ states corresponding to $I(^2P_{3/2})$ channel represent broken lines. There are $^3Q_0$ and $^{3,1}Q_1$ states around 270 nm region.

The scattering angular distribution also provides an electronic characterization for the 270-nm band. As explained in Section 2.2.2.2, the anisotropy parameter, β, was determined by fitting Eq. (2.2) the observed angular distributions. A value of $\beta = 1.4 \pm 0.1$ was determined for the fast component and $\beta = 1.0 \pm 0.1$ for the slow one in the I($^2P_{3/2}$) channel, which were practically separated at the velocity of 640 m/s. A value of $\beta = 1.5 \pm 0.1$ was determined for the I*($^2P_{1/2}$) channel treated as a single component. These large positive β values indicate a roughly parallel direction between the transition dipole moment and the C−I bond, assuming that the dissociation is prompt. This is reasonable for the dominant $^3Q_0$ photoabsorption at 266 nm. Although the I($^2P_{3/2}$) channel is likely affected by the non-adiabatic process, the similar results to the present measurements are found for a representative C−I system of CH_3I; the large and positive β parameters were observed for the I($^2P_{3/2}$) channel at most of wavelengths in the A-band.[32] Thus, the observed β values at 266 nm are not inconsistent with an interpretation that the excited state(s) contain a large proportion of $n_I\sigma_{C-I}^*$ character localized in the C−I bond.

3.3.2.2 213-nm Photodissociation

The $P(E_{trans})$ and $E_{int}(C_3H_5)$ distributions at 213 nm are shown in Figure 3.6 in the same way as Figure 3.6 for the 266-nm data. Similarly to the 266-nm data, the $P(E_{trans})$ and $E_{int}(C_3H_5)$ distributions in the $I^*(^2P_{1/2})$ channel had a single component (Figure 3.6 (a) and (b), red), whereas those in the $I(^2P_{3/2})$ channel showed a bimodal structure (Figure 3.6 (a) and (b), black). It was noted that the observed image for the $I(^2P_{3/2})$ channel (Figure 3.3 (c)) contained a non-negligible one-color signal in the outer (faster) region (> 500 m/s); 17 % of the total intensity over the entire velocity range was solely due to the probe laser and the one-color signal at a particular velocity region amounted to at most half of the pump-probe signal intensity. This one-color signal at 304 nm is considered to be due to dissociation and detection within the same laser pulse, since the scattering distribution was quite similar to the pump-probe data at 266 nm. The probe laser wavelength of 304 nm is located at the longer side edge of the 270-nm band. The $P(E_{trans})$ distribution of the $I(^2P_{3/2})$ channel in Figure 3.6 (a) (black) were obtained by subtracting the one-color (304 nm) data from those under the pump + probe (213 nm + 304 nm) conditions with the same pulse energy. As a result of the subtraction, the ratio between the slow and fast components (slow:fast = 6:4) obtained by fitting two Gaussian functions to the $I(^2P_{3/2})$ data is not sufficiently accurate for a quantitative discussion. However, the generation of two differently energized C_3H_5 fragments was well illustrated in the present measurement. Analysis of the angular distributions yielded a value of $\beta = 1.0 \pm 0.1$ for the $I^*(^2P_{1/2})$ channel. The $I(^2P_{3/2})$ data were divided into the slow and fast components at a scattering velocity of 500 m/s, and the values of $\beta(^2P_{3/2}, \text{fast}) = 1.0 \pm 0.1$ and $\beta(^2P_{3/2}, \text{slow}) = 0.9 \pm 0.1$ were

determined. The error was evaluated from the influence of the subtraction and the selection of the velocity ranges. The average values of $<E_{trans}>$ and $<E_{int}(C_3H_5)>$, along with the fraction of the translational energy in the available energy, f_{trans}, are summarized in Table 3.2.

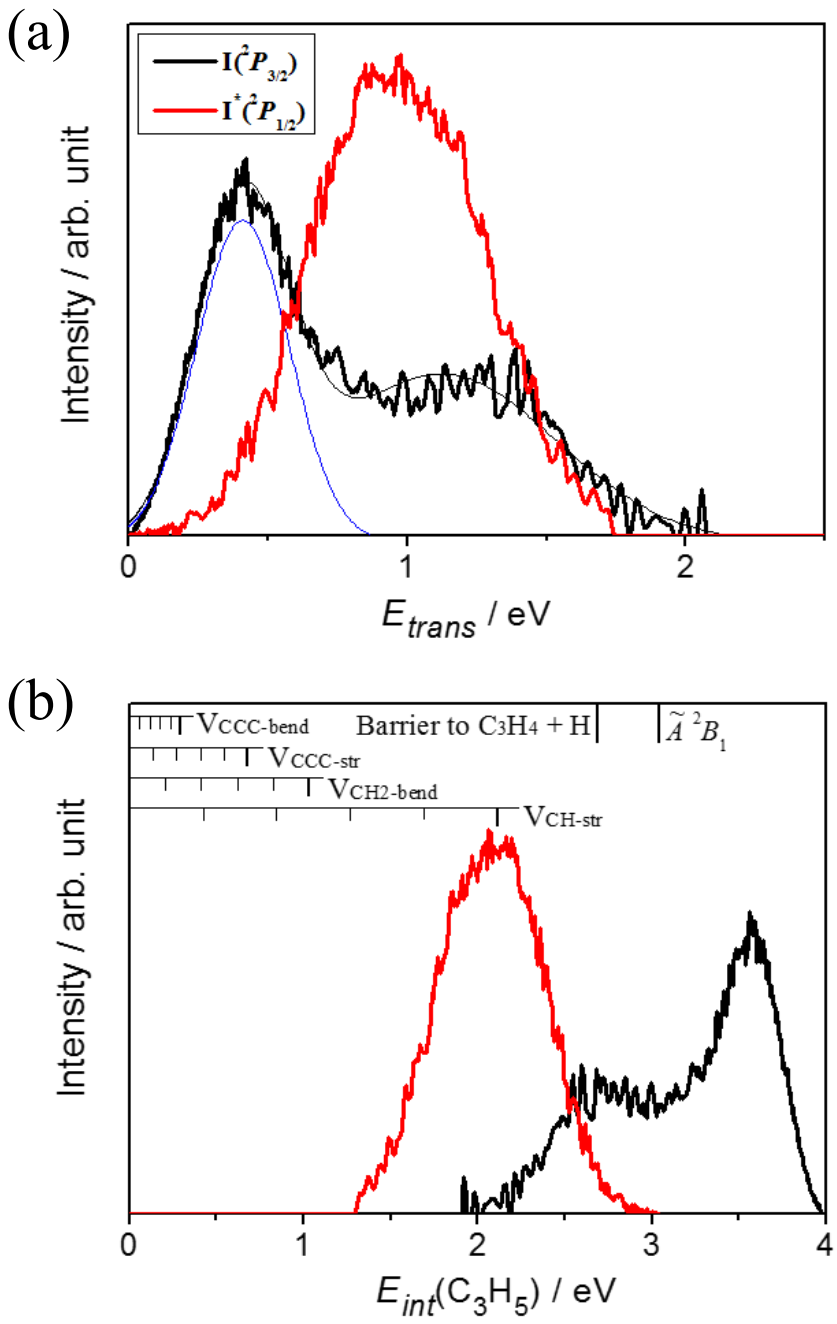

Figure 3.6 (a) The center-of-mass translational energy distribution of the C_3H_5I photolysis at the photolysis wavelength of 213 nm. (b) The internal energy distribution of the C_3H_5 counter-product. The data of $I(^2P_{3/2})$ and $I^*(^2P_{1/2})$ are shown by black and red lines, respectively. The intensity is normalized so that the data of the $I(^2P_{3/2})$ and $I^*(^2P_{1/2})$ channels have the same area intensity.

The UV absorption bands of C_3H_5I below 240 nm were interpreted as being relevant to the π-type orbital of the allyl group (electronic configuration with π_{CC}^{-1} or π_{CC}^{*}) in the spectroscopic studies[9, 10, 12] and the *ab initio* calculation.[11] In a simplified description using the local symmetry at the allyl group and the C−I bond, the $\pi_{CC}\pi_{CC}^{*}$ state is a bound state about the C−I bond, as shown in Figure 3.7, indicating that an electronic relaxation from the photoinitiated $\pi_{CC}\pi_{CC}^{*}$ state is required for the C−I bond cleavage to occur. In the C−X (X = Cl, Br) fission pathway of the C_3H_5Cl and C_3H_5Br photodissociation following the $\pi_{CC}\pi_{CC}^{*}$ excitation, the fast and slow components in the bimodal $P(E_{trans})$ of the X($^2P_{3/2}$) fragments were attributed to the different potential energy surfaces.[47, 48, 50] For C_3H_5Cl, the fast and slow Cl($^2P_{3/2}$) were ascribed to predissociation by the $n_{Cl}\sigma_{C-Cl}^{*}$ surface and internal conversion to the ground state, respectively. For C_3H_5Br, the two repulsive excited-state surfaces ($\pi_{CC}\sigma_{C-Br}^{*}$ and $n_{Br}\sigma_{C-Br}^{*}$) were presumed to be the origin of the bimodal $P(E_{trans})$. Furthermore, I refer to the systematic study of the photodissociation of vinyl halides[42] as the simplest π-system + *p*-orbital (of halogens) system for an interpretation of the present data. A model provided by Zou *et al*. explained that the photodissociation mechanism of vinyl iodide was attributed to excited-state dissociation rather than internal conversion, in contrast to fluoride and chloride.[42] Since this model was based on the increase of the np_X orbital energy as heavier halogens (X = F, Cl, Br, I) with respect to the π_{CC} orbital energy, it is applicable to allyl halides. From this halogen-dependence of the photodissociation mechanism associated with the $\pi_{CC}\pi_{CC}^{*}$ transition in π + *np* systems, it can be deduced that the high and low E_{trans} peaks in Figure 3.6 (a) are caused

by predissociation from the photoinitiated $\pi_{CC}\pi_{CC}^*$ state at 213 nm to the dissociative surfaces. Since the angular distribution describes the relationship between the recoil velocity vector and the laser polarization direction (hence, the transition dipole moment), the almost the same β values observed in all the three components support their identical photoinitiation. Ji *et al*. suggested the possible participation of the $\pi_{CC}\sigma_{C\text{-}Br}^*$ surfaces in the C_3H_5Br photodissociation on the basis of the *ab initio* calculation for the low-lying states.[47] However, I presume that the production mechanisms of $I(^2P_{3/2})$ and $I^*(^2P_{1/2})$ at 213 nm involve predissociation through the $n_I\sigma_{C-I}^*$ states by comparison with the 266-nm data (Figure 3.4), for which I interpreted the reaction mechanism as the direct absorption to the dissociative $n_I\sigma_{C-I}^*$ (three $^{1,3}Q_{0,1}$) states in the former section. If it is assumed that the energy order is $^1Q_1 > {}^3Q_1$ according to Mulliken's model, the slower (the major) and faster (the minor) components in Figure 3.6 (a) are assigned to the predissociation to the $^3Q_1$ and $^1Q_1$ surfaces, respectively, both of which are adiabatically correlated to $C_3H_5 + I(^2P_{3/2})$.

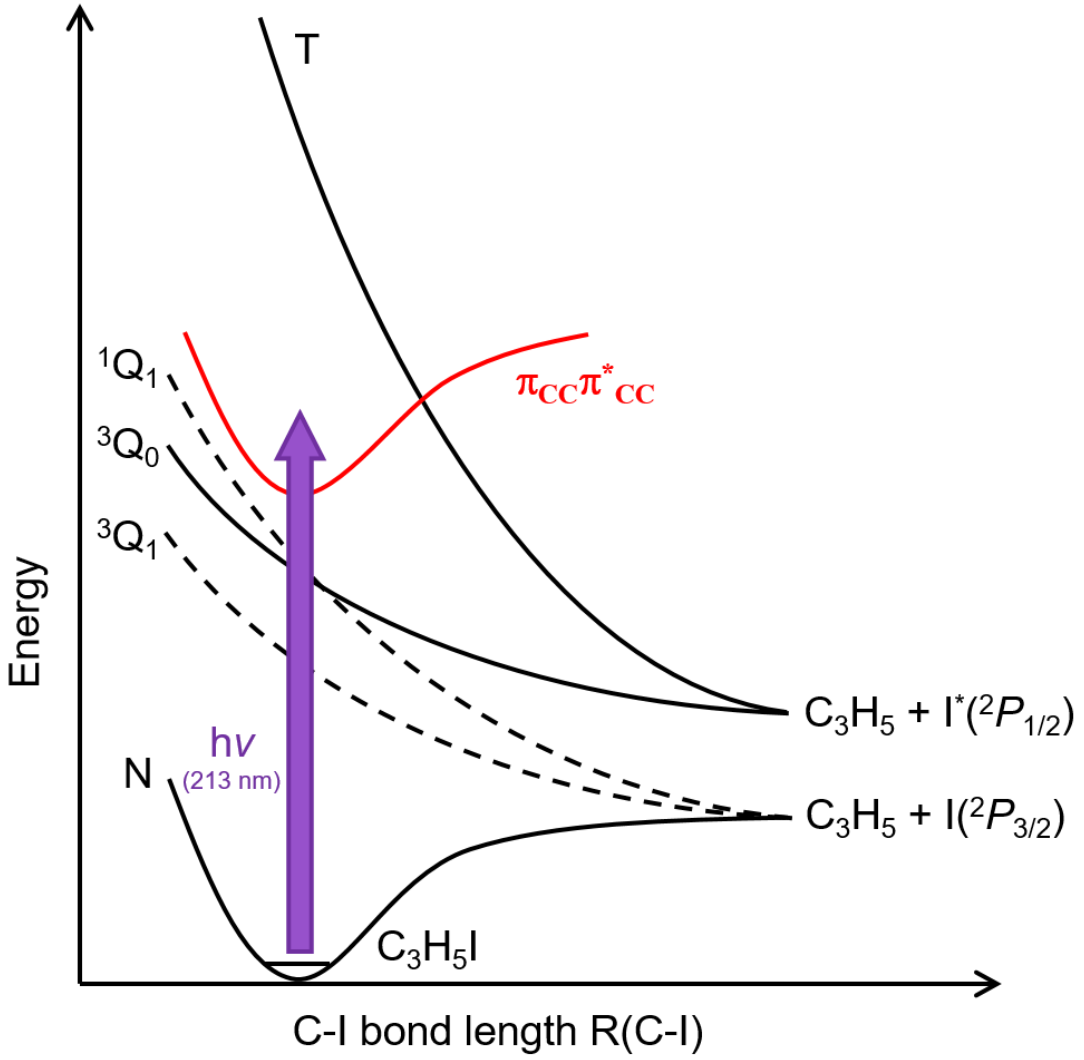

Figure 3.7 Schematic view of the electronic transition in the 200 nm band. In addition to nσ^* states simply represented by Mulliken's notation (shown in Figure 3.5), C_3H_5I has $\pi\pi^*$ state derived from the C=C bond. The photoabsorption band around 200 nm can be ascribed to the transition to the $\pi\pi^*$ state.

It is noteworthy that there are limitations in describing the electronic excited states by labels of local orbitals (n_I, σ_{C-I}, π_{CC}) for a non-planer polyatomic C_3H_5I even though the C=C bond is not directly connected to the C−I bond. The mixing of the n_I and σ_{C-I} orbitals was shown by the *ab initio* calculation as the excited-state property in the Franck−Condon region for photoabsorption at around 200 nm.[11] On the other hand, the energy partitioning at 213 nm shown in Table 3.2 clearly represents the local photoinitiation in the allyl framework. The photochemical property of the 213-nm photodissociation is seen more clearly compared with the result at 266 nm, which I attributed to a local photochemistry in the C−I bond. The f_{trans} values at 213 nm (0.29, 0.11, and 0.25) were almost half of those in the corresponding pathways at 266 nm (0.55, 0.33, and 0.41). The value of $(1 - f_{trans})$, which gives a fraction of the rovibrational energy of the C_3H_5 radical in the available energy, was significantly larger at 213 nm than at 266 nm in all the pathways. Correspondingly, the $<E_{int}(C_3H_5)>$ at 213 nm (2.76 eV, 3.47 eV, and 1.98 eV) is markedly higher than that at 266 nm (1.22 eV, 1.81 eV, and 0.65 eV). This analysis showed that the C_3H_5 radical generated at 213 nm is internally excited more than the photon energy difference between 213 nm and 266 nm ($h\nu_{213} - h\nu_{266}$ = 1.17 eV). Although the bimodal distribution of the $I(^2P_{3/2})$ channel precludes accurate evaluation of the energy width, the wider $<E_{int}(C_3H_5)>$ distribution in the $I^*(^2P_{1/2})$ channel at 213 nm (fwhm = 0.8 eV by Gaussian fitting) than that at 266 nm (fwhm = 0.4 eV) is visible on comparing Figure 3.4 (b) and Figure 3.6 (b). These results provide evidence that the $\pi_{CC}\pi_{CC}^*$ photoinitiation deforms the allyl framework. The instantaneous distortion energy, which is locally given to the allyl framework, is partially used for the C−I bond cleavage, leaving the

other portion ($1 - f_{trans}$) in the C_3H_5 radical. This phenomenological explanation is equivalent to predissociation from the photoexcited $\pi_{CC}\pi_{CC}^*$ to the repulsive $n_I\sigma_{C-I}^*$ states. It was noted that the emission spectra obtained upon the 199.7-nm photolysis observed by Parsons *et al.* did not show the excitation of the C−C=C torsional mode, which was expected as experimental evidence of the $\pi_{CC}\pi^*_{CC}$ configuration.[11] The absence of the out-of-plane C−C=C torsion in the initial motions was explained as being the result of dominant Rydberg character of the excited state over the π^*_{CC} character. However, translational spectroscopy carried out by the same group[20] and ion-imaging[19] for the 193-nm photolysis showed the relatively low $P(E_{trans})$ distributions peaked at approximately 20 kcal/mol, which corresponds to the f_{trans} values of 0.19 and 0.25 for the I($^2P_{3/2}$) and I*($^2P_{1/2}$) channels, respectively. These f_{trans} values at 193 nm are similar to those observed at 213 nm, thus consistently indicating the generation of internally excited C_3H_5 radical.

3.4 Summary and Conclusion

The photodissociation dynamics of C_3H_5I in the two lowest UV bands were investigated. The REMPI spectrum and the scattering distributions of the iodine products were selectively measured for the two spin-orbit states at photolysis wavelengths of 266 nm and 213 nm: $C_3H_5I + h\nu_{266,213} \rightarrow C_3H_5 + I(^2P_{3/2})$, $C_3H_5 + I^*(^2P_{1/2})$. The two UV bands showed the preferential generation of $I^*(^2P_{1/2})$, indicating that the electronic correlation from the Franck−Condon region to the product asymptotes describes the dissociation mechanism well. The singly peaked and bimodal velocity distributions observed, respectively, in the $I^*(^2P_{1/2})$ and $I(^2P_{3/2})$ pathways were ascribed to the numbers of the correlating $n_I\sigma_{C-I}^*$ potential energy surfaces. While for the identical exiting pathways along the $n_I\sigma_{C-I}^*$ ($^{1,3}Q_{0,1}$) surfaces in the 270-nm and 215-nm bands, the difference in the electronic characters between these two bands was observed in the energy partitioning of the available energy. The average of the translational energy release at 266 nm was found to be larger than that of the more energized photolysis at 213 nm, indicating the generation of the internally cold and hot C_3H_5 radicals at 266 nm and 213 nm, respectively. These results were interpreted to be due to site-selective photochemistry; direct absorption to the $n_I\sigma_{C-I}^*$ ($^{1,3}Q_{0,1}$) dissociative states at 266 nm causes the fast C−I bond cleavage, while the photoinitiation of the allyl group (π system) at 213 nm is followed by predissociation to the $n_I\sigma_{C-I}^*$ surfaces to produce the C_3H_5 radical with a proportion of the energy remaining. These conclusions are mostly drawn on the basis of Mulliken's model, which was applied to the A-band photolysis of alkyl iodides, and on the systematic investigation of the photodissociation of vinyl halides.

Chapter 4.

Multiple Product Pathways of Nitromethane in Photodissociation of 213 nm

4.1 Introduction

Competition of several product pathways is one of the most important issues related to the photochemistry of polyatomic molecules. The product branching may be attributed to different excited state potential energy surfaces (PESs) or different trajectories (mechanisms) on an individual PES. Non-adiabatic transitions can be another important origin determining the product branching ratios. Nitromethane (CH_3NO_2) is one species that shows multiple product pathways during photodissociation. Although the photochemistry of CH_3NO_2, following ultraviolet (UV) photoabsorption, has been extensively studied by different experimental[51-63] and theoretical[64-66] approaches, identification of the overall product pathways and understanding of the reaction mechanisms have not yet been completed. The UV absorption spectrum of CH_3NO_2 consists of two broad maxima approximately centered at 275 nm ($n\rightarrow\pi^*$) and 200 nm ($\pi\rightarrow\pi^*$), as shown in Figure 4.1. It is widely accepted that the primary photodissociation process following both UV absorption bands is C−N bond cleavage to yield CH_3 and NO_2, *i.e.* $CH_3NO_2 + h\nu \rightarrow CH_3 + NO_2$. Other dissociation pathways competing with or following the C−N bond cleavage in the $\pi\rightarrow\pi^*$ absorption bands have been suggested in the experimental and theoretical studies, that are briefly outlined below.

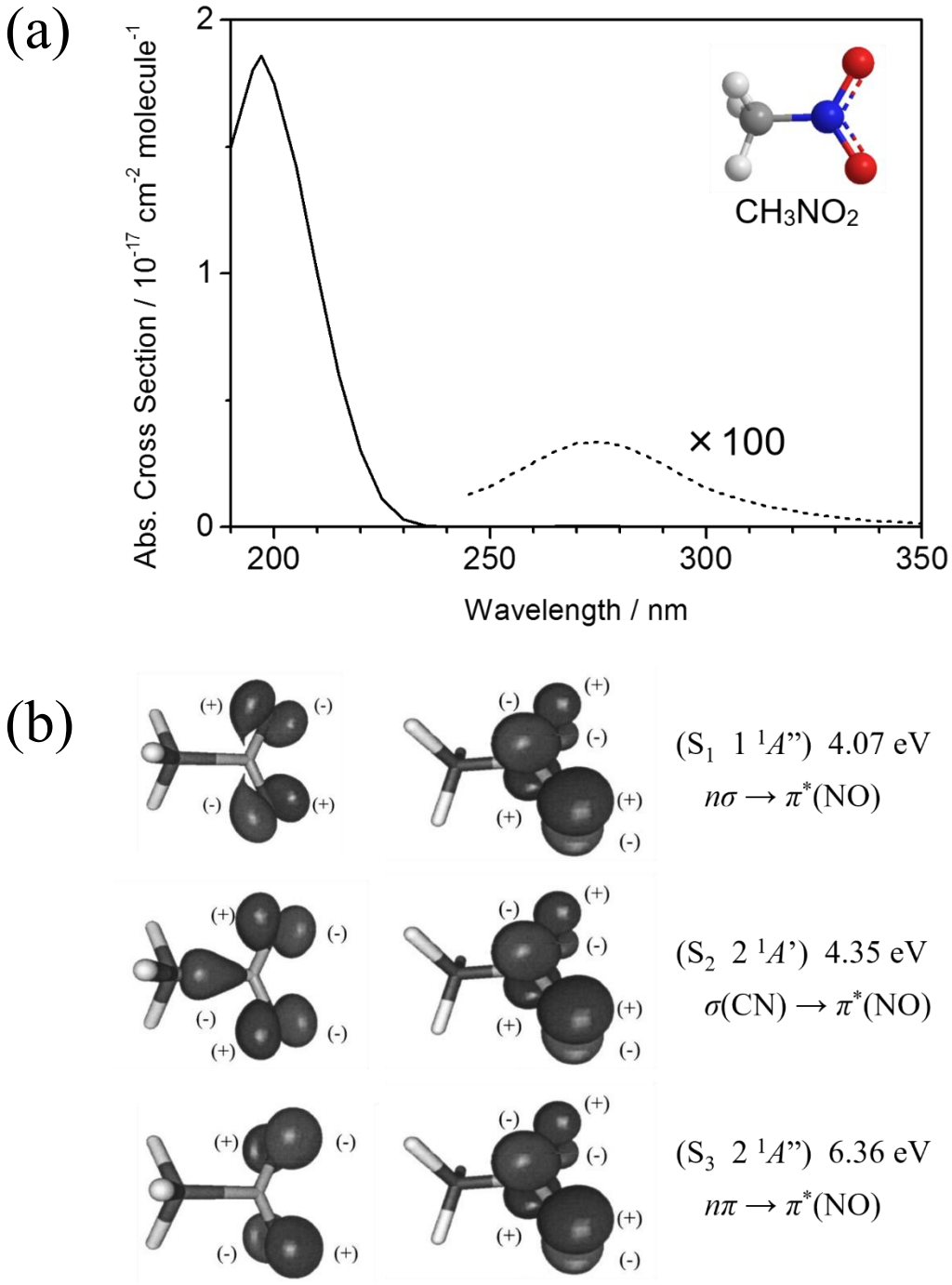

Figure 4.1 (a) The near-UV absorption spectrum of nitromethane at room temperature measured by W. D. Taylor *et al*. (Ref. 67). A dashed line displayed the absorption spectrum with a 100-fold enlarged scale. (b) Electronic configurations and vertical transition energies corresponding to $n \rightarrow \pi^*$ ($S_0 \rightarrow S_1$), $\sigma \rightarrow \pi^*$ ($S_0 \rightarrow S_2$), and $\pi \rightarrow \pi^*$ ($S_0 \rightarrow S_3$) transition calculated with MS-CASPT2 by Arenas *et al.* (Ref. 64).

The photodissociation dynamics of CH_3NO_2 following the $\pi \rightarrow \pi^*$ transition under a molecular beam condition was investigated at 193 nm[58, 59, 61, 63] and 226 nm.[62] The photolysis wavelength of 193 nm is located near the maximum of the $\pi \rightarrow \pi^*$ band, which has a large absorption cross-section (σ_{abs}(193 nm) = 1.7×10^{-17} cm^2) with presumably unit quantum yield for photodissociation.[58] In the dynamics study by Butler *et al,*[59] wherein product emission spectroscopy and photofragment translational spectroscopy were applied, two processes in the primary C−N bond cleavage were suggested to generate NO_2 in different electronic states on the basis of the two peaks observed in the CH_3 translational energy distribution. The higher translational energy component was ascribed to the *major* process generating NO_2 in the 1 $^2B_2$ electronic excited state, some of which undergoes unimolecular decomposition into NO and O. The slower CH_3 fragment, which was referred to as originating from the *minor* process, was explained as the counter-product of NO_2 generated in a different electronic state. The electronic state was not identified but characterized as having an efficient photoabsorption at 193 nm, subsequently dissociating into NO and O by absorbing a second photon within the same laser pulse. The *minor* process was assigned to CH_3 + NO_2(2 $^2B_2$) by Lao *et al.*[60] in the polarized emission spectroscopy study applied to dissociating CH_3NO_2, where the electronic state-correlation to the product pathways was taken into account. Moss *et al.*[61] proposed that NO_2 produced in the *minor* channel undergoes secondary photodissociation into the electronic excited NO(A $^2\Sigma^+$) and the O(^3P) atom. This conclusion was drawn based on the spectroscopic identification of the A $^2\Sigma^+ \rightarrow$ Rydberg transition and the state-resolved translational energy distribution of the NO(A $^2\Sigma^+$) fragment. The nanosecond and femtosecond laser

photolysis analyses at 226 nm were conducted by Guo *et al,*[62] who employed resonantly-enhanced multiphoton ionization (REMPI) spectroscopy and time-of-flight (TOF) measurement. The results of the photolysis experiments at both timescales indicated that the NO_2 molecule produced in the primary C−N bond cleavage is the precursor of the observed NO($X\,^2\Pi$) product. It was suggested that the nascent NO_2($1\,^1B_2$) intermediate absorbs a 226 nm photon to generate the NO product since a single 226 nm photon does not have enough energy to yield CH_3 + NO + O. In a recent photodissociation study at 193 nm, Rodriguez *et al.* measured the CH_3 translational energy distribution to obtain the speed-dependent anisotropy parameters by using a slice imaging technique.[63] They attributed the slow CH_3 product to the parent cluster dissociation and the fast one to three different dissociation mechanisms which generate ground-state CH_3 and NO_2 through different PESs.

Quantum chemistry calculations for the singlet and triplet PESs of CH_3NO_2 were performed by Arenas *et al*.[64] with high-level *ab initio* methods. The role of the surface crossing was investigated in order to interpret the experimental results of the photodissociation at 193 nm.[65] The calculation results showed that NO_2 is generated in at least two electronic states ($1\,^2B_2$ and $1\,^2A_1$) due to the decomposition of CH_3NO_2 after electronic deactivation through conical intersections. In a recent theoretical study using the global reaction root mapping calculations by Isegawa *et al,*[66] competing product pathways generating various products (CH_3NO, CH_3O, CH_2NO, H_2CO, HNO, OH, NO, and O) were predicted. The photoabsorption at 193 nm was computationally characterized as the $S_0 \rightarrow S_3(\pi\pi^*)$ transition, which was indicated to electronically

cascade down to the S_2, S_1 and S_0 PESs. The formation of $NO_2(1\ ^2B_2)$ was ascribed to the direct dissociation on the S_1 PES as the *major* product pathway. Their calculations yielded some efficient means through which the sequential electronic relaxation can reach the S_0 PES, on which the system has a large excess energy that can yield remarkable dynamics. Possible pathways of nitro-nitrite isomerization and the roaming paths generating $O(^1D)$, OH and NO were theoretically found on the S_0 PES, all of which are initiated by the $\pi \rightarrow \pi^*$ photoabsorption.

In our previous 213 nm photolysis study,[68] two peaks were observed in the recoil velocity distribution of the CH_3 fragment, which were similar to those observed in the experiments at 193 nm.[59, 61] The concerted three-body dissociation pathway of $CH_3 + NO(X\ ^2\Pi) + O(^3P)$ was proposed as the origin of the slow CH_3 product. In the present study, which was conducted for further investigation, I measured the REMPI spectra and the state-resolved translational energy distributions of the photofragments: $CH_3(X\ ^2A_2''; v = 0, v_2 = 1)$, $NO(X\ ^2\Pi; v = 0, 1, 2$ and $A\ ^2\Sigma^+)$ and $O(^3P)$. Herein I discuss the photodissociation dynamics of CH_3NO_2 following the $\pi \rightarrow \pi^*$ transition by comparing our observed data with the results of previous experimental studies and the recent theoretical studies.

4.2 Experimental

The experimental apparatus and laser setup were explained in Section 2.1. A commercial CH_3NO_2 reagent was used without further purification. The gas sample, 0.5% diluted CH_3NO_2 in a He buffer, was used at a stagnation pressure of 2 atm. The inner pressure in the source chamber was 2×10^{-5} Torr. The pressure in the detector chamber was kept in the range of 10^{-7} Torr when the molecular beam was introduced through a skimmer. The pulse energy of the photolysis laser was varied from 10 μJ/pulse to 30 μJ/pulse. During the measurement, the molecular beam condition and photolysis pulse energy were varied from the above values when cluster formation of the parent molecule was examined.

The different pulse energies of the probe laser were applied for each photofragment: from 80 μJ/pulse to 200 μJ/pulse for the detection of the CH_3 fragment, less than 10 μJ/pulse for the NO fragment, and 30 μJ/pulse for the $O(^3P_J)$ fragment. The probe laser was circularly polarized using a Berek polarization compensator (New Focus, Model 5540) to detect the CH_3 fragment. The intense *Q*-branch in the [2+1] REMPI spectrum with linearly polarized light is known to be sufficiently suppressed by circular polarization, enabling resolution of the rotational (*N*) lines. Other products were detected with linear polarization.

The velocity and angular distributions for the photofragments were obtained by applying Abel inversion, which assumes cylindrically symmetric scattering distribution. The anisotropy parameter, β, was determined by means described in Section 2.2.2.2. The data analysis neglects the higher-order multipole moments relevant to molecular alignment, which can be measured by

circularly polarized light. Rodriguez *et al.*[63] found mild rotational alignment of the CH_3 fragment at the 193 nm photolysis by applying an advanced slice imaging technique, implying that the β values obtained in this study are effective β_2 parameters. I estimated the error of the β parameters to be ±0.2, limiting the following discussion angular distributions to a qualitative one.

4.3 Results and Analysis

4.3.1 CH_3 Fragment

The CH_3 fragments in the vibrational ground ($v = 0$) and excited states were probed by using the two-photon resonance associated with the $3p\ ^2A_2'' \leftarrow X\ ^2A_2''$ electronic transition. The [2+1] REMPI spectrum of the CH_3 fragment produced in the $v = 0$ state with circularly polarized light is shown in Figure 4.2. The *O*-, *P*-, *R*- and *S*-branches, which interfered with the intense *Q*-branch stack in our previous study using linearly polarized light,[68] appear clearly in this spectrum. The REMPI spectrum shows the rotational state population of the $CH_3(v = 0)$ product extending up to approximately $N = 15$. By using the formula for the line strength that was presented by Chen,[69] the rotational state distribution and average rotational energy of the $CH_3(v = 0)$ product ($<E_{rot}^{CH_3}>$) were obtained to be $<E_{rot}^{CH_3}> = 1.3$ kJ/mol.

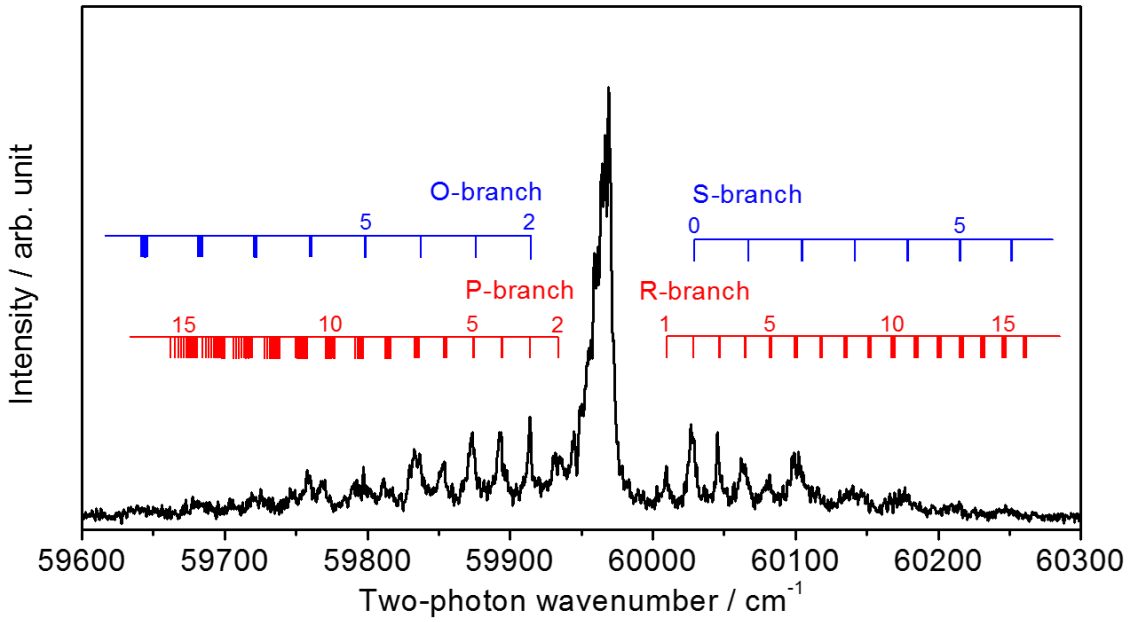

Figure 4.2 [2+1] REMPI spectrum of the CH_3 fragment (v=0) generated in the photodissociation of CH_3NO_2 at 213 nm. The circularly polarized light is employed for ionization. The rotational (N) structure with the O-, P-, R- and S-branches is resolved in both sides of the intense Q-branch (rotationally unresolved). The positions of the K states are shown as stacked bars in each N transition for reference.

I observed the scattering distributions of the CH_3 fragment at four rotational lines associated with the $N = 2-12$ states in the $v = 0$ state and that of the ν_2 (out-of-plane bending) excited state at the maximum of the Q branch of the 2_1^1 band (Figure 4.3 (a)). The rotational lines of the CH_3 ($\nu_2 = 1$) fragment REMPI spectrum could not be resolved because of the weak signal intensity of the 2_1^1 band. The scattering image observed at the mixed line with the $N = 2$ and 3 states in the $v = 0$ state most strongly demonstrates the production of

slow and fast CH_3 fragments, which were consistently observed in the molecular beam experiments at 193 nm[59, 61, 63] and 213 nm.[68] The ratio of the fast and slow component intensities significantly varied with the internal (vibrational and rotational) energy. The CH_3 translational energy distributions ($P(E_{trans}^{CH_3})$) obtained from the scattering images are shown in Figure 4.3 (b). The $P(E_{trans}^{CH_3})$ of the CH_3 ($v = 0$) fragment consists of two components as shown in the images; the high $E_{trans}^{CH_3}$ component is distributed in a broad region from $E_{trans}^{CH_3}$ = 10 kJ/mol to 90 kJ/mol, and the low $E_{trans}^{CH_3}$ component exhibits a narrow distribution within $E_{trans}^{CH_3}$ < 10 kJ/mol. The $P(E_{trans}^{CH_3})$ plots were normalized so that the maximum of the high $E_{trans}^{CH_3}$ component of each N state would have the same intensity, thus clarifying the variation of the relative intensities of the sharp and the broad components with respect to the N values. The ratio of the lower $E_{trans}^{CH_3}$ component relative to the higher one markedly decreases as N increases. The $P(E_{trans}^{CH_3})$ of the $v_2 = 1$ state also shows a bimodal structure. The contribution of the low $E_{trans}^{CH_3}$ peak to the total signal is as small as that in the high N (> 6) states in the $v = 0$ state. The peak and average values of $E_{trans}^{CH_3}$ for both components of the $v = 0$ and $v_2 = 1$ states are listed in Table 4.1. These $E_{trans}^{CH_3}$ values for the CH_3 ($v = 0$) fragment are slightly larger than those of the $v_2 = 1$ state. However, the difference is much smaller than the vibrational energy spacing of ν_2 (7.3 kJ/mol),[70] indicating inefficient partitioning of the available energy (E_{avail}) to $E_{trans}^{CH_3}$.

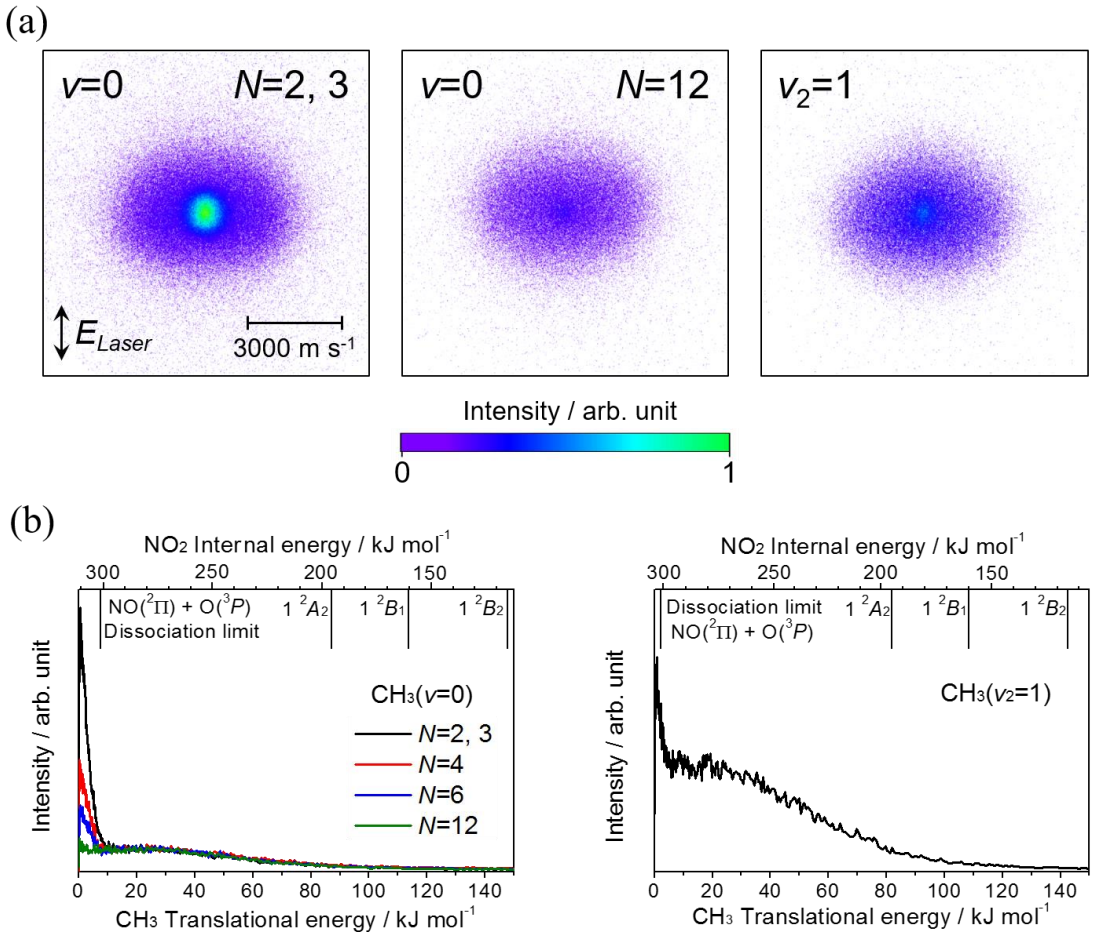

Figure 4.3 (a) State-resolved scattering images of the CH_3 photofragment at 213 nm. The polarization of the photolysis laser is vertical in the images. (b) Translational energy distributions of the CH_3 fragment obtained from the scattering images. The intensity plot in the left hand side is normalized at the maximum around the translational energy of 40 kJ/mol to show the rotational state dependence in the v=0 state. The upper bar is a scale for the internal energy of the NO_2 counter-product calculated by neglecting the internal energy of the measured CH_3 product.

Table 4.1 Translational energies and anisotropy parameters of the CH_3 photofragment.

State	Component	E_{trans} peak (kJ/mol)	$\langle E_{trans} \rangle$ (kJ/mol)	β
$X\,^2A_2''$; $v = 0$	Slow	0.7	2.0	0.2
	Fast	19.8	26.7	–0.5
$X\,^2A_2''$; $v_2 = 1$	Slow	1.2	1.7	0.1
	Fast	16.6	24.0	–0.3

By simply assuming that the production origin of CH_3 is the two-body dissociation to CH_3 + NO_2, the nascent internal energy of the NO_2 counter-product can be related to the state-resolved $E_{trans}^{CH_3}$ value by Eq. (2.1). The upper scale in Figure 4.2 (b) indicates $E_{int}^{NO_2}$ calculated by Eq. (2.1) for the $v = 0$ and $v_2 = 1$ states. As a guide for the internal energy scale, the term energies of the low-lying electronic excited states of NO_2 ($1\,^2B_2$, $1\,^2B_1$, $1\,^2A_2$) and the decomposition threshold to NO($X\,^2\Pi$) + O(^3P) were superimposed.[71, 72] The NO_2 product associated with the fast CH_3 fragment has a broad range of $E_{int}^{NO_2}$ from about 150 kJ/mol to 300 kJ/mol, whereas NO_2 co-produced with the slow CH_3 fragment has a limited range of $E_{int}^{NO_2}$ from 298 kJ/mol to 311 kJ/mol. Almost all of the NO_2 products are energetically populated above the $1\,^2B_2$, $1\,^2B_1$, and $1\,^2A_2$ states. Electronically excited NO_2 generation was evidenced by chemiluminescence detection in the 193 nm photodissociation study.[59] The nascent $E_{int}^{NO_2}$ distribution obtained in the present investigation further confirms the

formation of the significantly energized NO_2 at 213 nm. There is no clear evidence for the NO_2 production in the electronic ground state ($\widetilde{X}\ ^2A_1$), which would be given by a population with $E_{int}^{NO_2} < 116$ kJ/mol ($\widetilde{A}\ ^2B_2$). It is noted that the sharp peak in the higher $E_{int}^{NO_2}$ region is located near the dissociation threshold of NO($X\ ^2\Pi$) + O(^3P).

The β values obtained separately for the fast and slow CH_3 fragments in the $v = 0$ and $v_2 = 1$ states are shown in Table 4.1. Those of the slow components of the CH_3 fragment are small and positive, whereas the fast components show negative β values in both vibrational states. The β values were measured in the previous studies at 193 nm without selecting the final state,[59] and with selecting both final state and recoil velocity.[63] Our results for the angular distribution at 213 nm are qualitatively in good agreement with these data of these 193 nm photodissociation studies,[59, 63] reflecting both photolysis wavelengths are responsible for the $\pi \rightarrow \pi^*$ transition.

4.3.2 NO ($X\,^2\Pi_\Omega$; v = 0, 1, 2) Fragment

The spectra of the NO($X\,^2\Pi_\Omega$) fragments of the vibrational ground (v = 0) and excited (v = 1 and 2) states were measured by [1+1] REMPI spectroscopy via the $A\,^2\Sigma^+ \leftarrow X\,^2\Pi_\Omega$ transition. The spectrum of NO(v = 0) observed in the 225−227 nm region is shown in Figure. 4.4 (a). The band head structure of the Ω = 1/2 and 3/2 spin-orbit manifolds are clearly exhibited in the spectrum, enabling assignment of each rotational line. The rotational state population obtained by calibrating the line intensity was not satisfactorily reproduced by applying a Boltzmann distribution. The best fit of the analysis using a Boltzmann distribution yielded a rotational temperature of 500 K, where deviation between the observed and simulated spectra (Figure 4.4 (b)) is perceptible in the middle J region. Although this rotational temperature yields a rough evaluation of the rotational energy partitioning, it was further analyzed, as will be discussed.

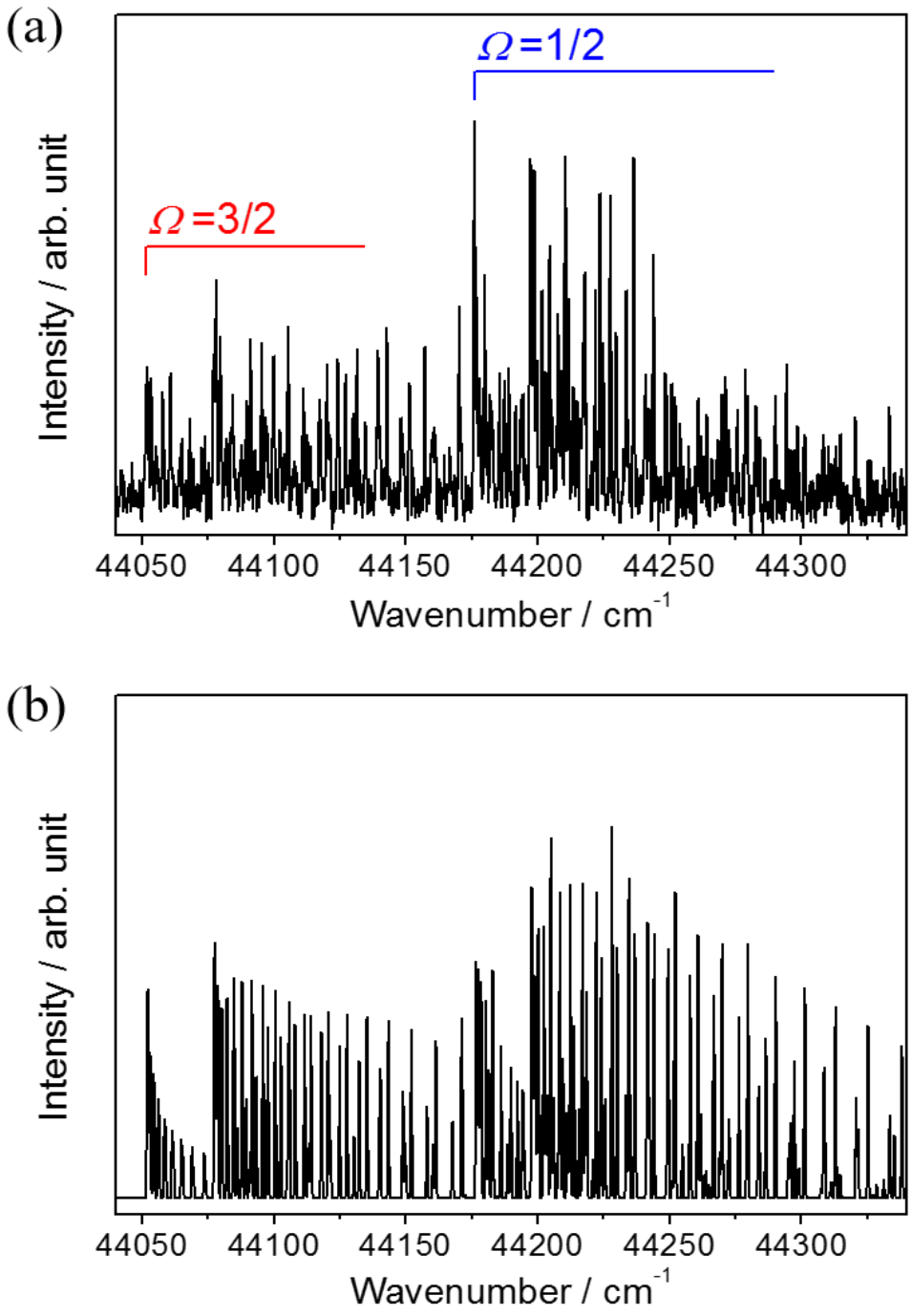

Figure 4.4 (a) Observed and (b) simulated [1+1]REMPI spectra of the NO photofragments generated in the v=0 state. The simulated spectrum is calculated by assuming the Boltzmann distribution with a rotational temperature of 500 K

The scattering images and the translational energy distribution of the NO fragment ($P(E_{trans}^{NO})$) for several ($v = 0$, J, $\Omega = 1/2$, $3/2$) states are shown in Figure 4.5. The NO($v = 0$) fragment exhibited two translational energy components. For both Ω spin-orbit states, the slower NO($v = 0$) fragment with $E_{trans}^{NO} < 10$ kJ/mol decreases in intensity as the rotational energy increases. The slower NO($v = 0$) fragment in the $\Omega = 1/2$ state appears more clearly than that of the $\Omega = 3/2$ state (spin-orbit splitting of 1.4 kJ/mol), indicating that the intensity of the slower component varies with the total internal energy. The energy dependences of the fast and slow components are also observable in the CH_3 photofragment results.

The REMPI spectra of the NO fragments in the vibrationally excited states ($v = 1$, 2), which were probed in the 226−238 nm and 238−248 nm regions, are shown in Figure 4.6 (a) and (b), respectively. The observed NO($v = 1$, 2) fragments show much more highly rotational excitations than the $v = 0$ state exhibits. The rotational levels up to about $J = 60.5$, which would have a Boltzmann factor of < 0.01 at 1000 K, are discernible in the spectra of both of the vibrational excited states. The nascent rotational state distribution of the NO($v = 1$) product was measured by Guo *et al*.[62] at a photolysis wavelength of 226 nm; their spectrum was reproduced by a Boltzmann distribution at a rotational temperature of 600 K. Although the REMPI spectra of the NO($v = 1$, 2) fragments at 213 nm that were obtained in this investigation exhibit non-Boltzmann distributions, the NO($v = 1$, 2) fragments show rotational excitation much greater than those obtained at 226 nm.

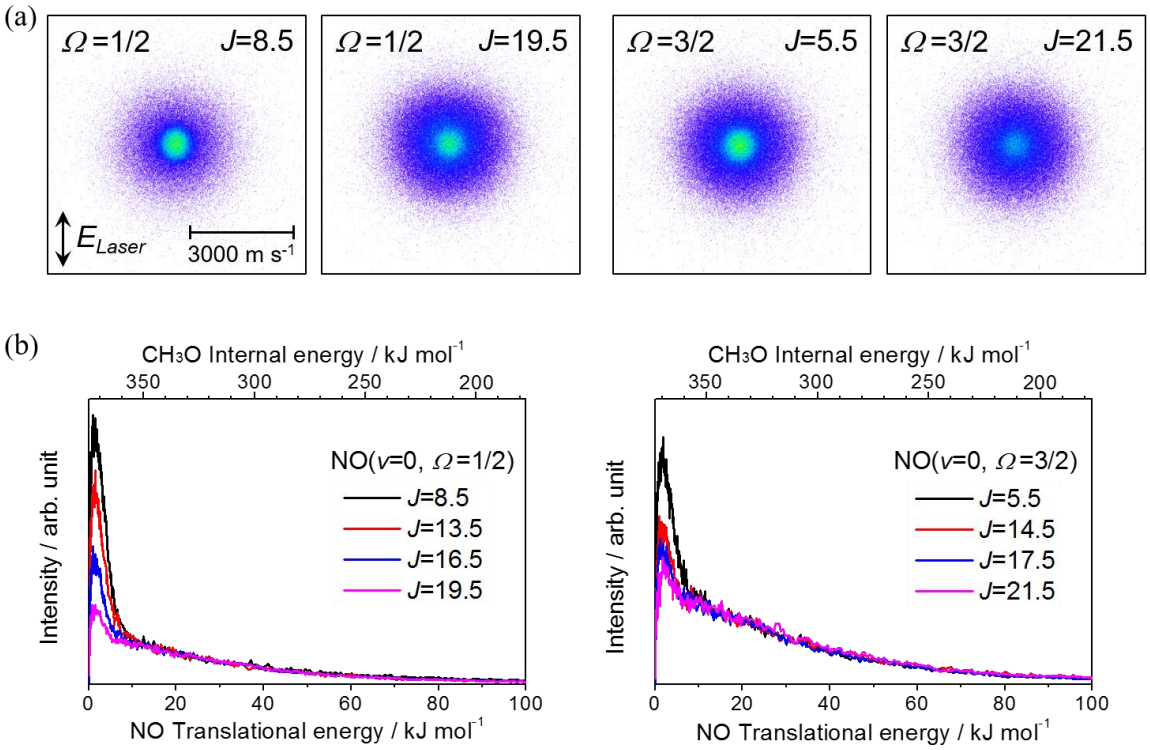

Figure 4.5 (a) State-resolved scattering images of the NO photofragment generated in the $v = 0$ state. (b) Translational energy distribution of the NO fragment obtained from the (J, Ω) state-resolved scattering images. The intensities of the plots are normalized at the higher translational energy region to show the variation of the lower energy part with respect to J in each Ω state. The internal energy of the CH_3O counter-product assuming the CH_3O + NO pathway is shown at the upper bar.

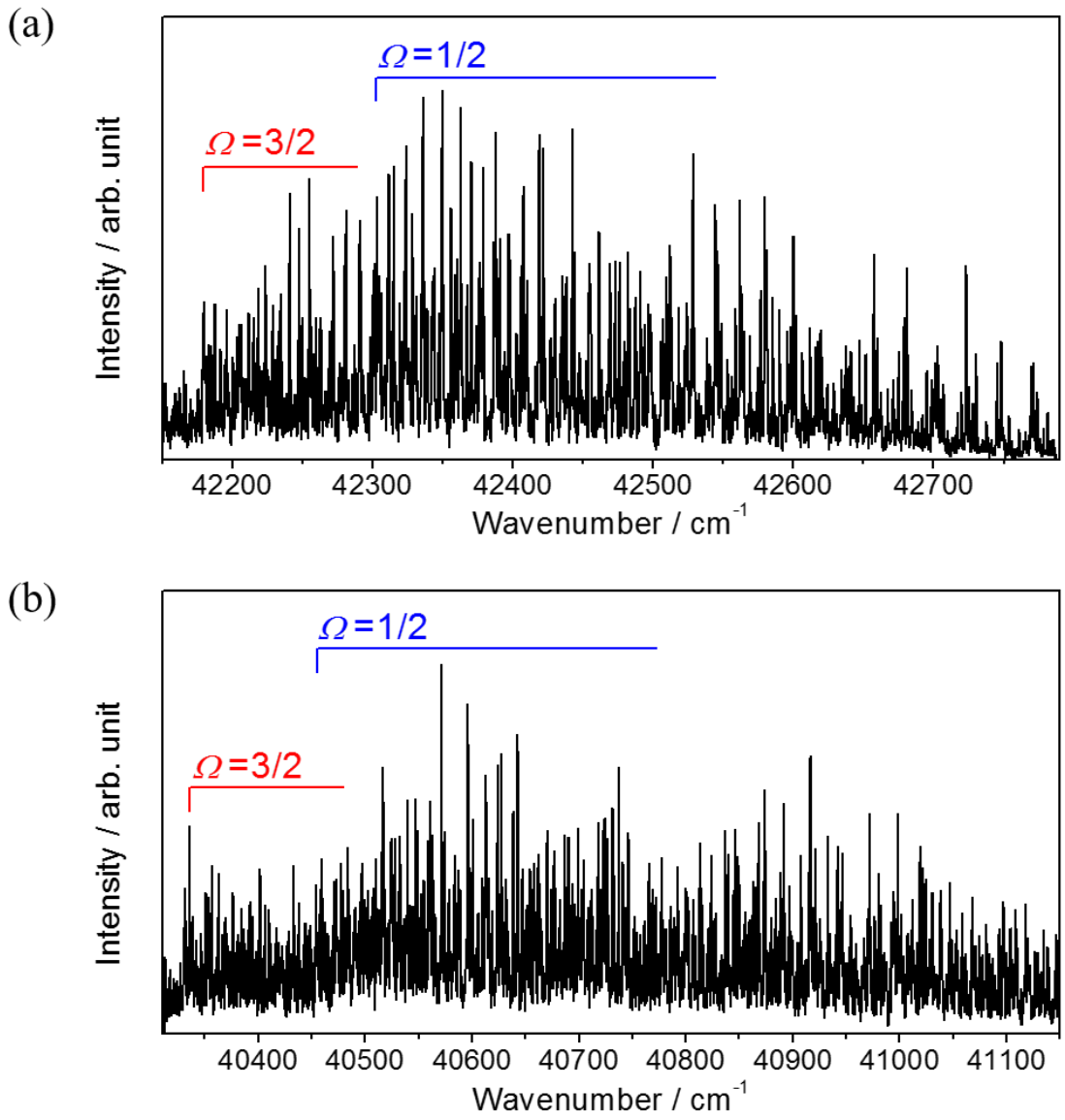

Figure 4.6 [1+1]REMPI spectra of the NO photofragments generated in the (a) $v = 1$ and (b) $v = 2$ vibrational excited states.

The scattering distribution and the $P(E_{trans}^{NO})$ of the NO(v = 1, 2) fragments are shown in Figure 4.7 (a) and (b), respectively. The $P(E_{trans}^{NO})$ of the NO(v = 1, 2) fragments shows a broad distribution without the low E_{trans}^{NO} peak, which was characteristically observed in the NO(v = 0) and CH_3 fragments (Figure 4.5 and 4.3, respectively). I observed the scattering distribution of the NO(v = 1, 2) fragment at several lines among those associated with the J = 7.5−60.5 rotational states. However, no significant differences were observed within the same vibrational level. The peak and average E_{trans}^{NO} values are similar in the v = 1 and 2 states and are also similar to that of the faster NO(v = 0) fragment component (shown in Table 4.2). The angular distributions of NO(v = 1, 2) and the faster NO(v = 0) fragment are almost isotropic and have similar β values (Table 4.2). Thus, the NO(v = 1, 2) and the faster NO(v = 0) were found to exhibit nearly identical scattering distributions.

Table 4.2 Translational energies and anisotropy parameters of the NO photofragment.

State	Component	E_{trans} peak (kJ/mol)	$\langle E_{trans} \rangle$ (kJ/mol)	β
$X\ ^2\Pi_\Omega$; $v = 0$	Slow	1.8	2.2	0.1
	Fast	10.3	23.5	0.0
$X\ ^2\Pi_\Omega$; $v = 1$	(Single)	10.4	24.6	0.1
$X\ ^2\Pi_\Omega$; $v = 2$	(Single)	12.5	26.1	0.1
$A\ ^2\Sigma^+$	(Single)	12.2	24.4	0.1

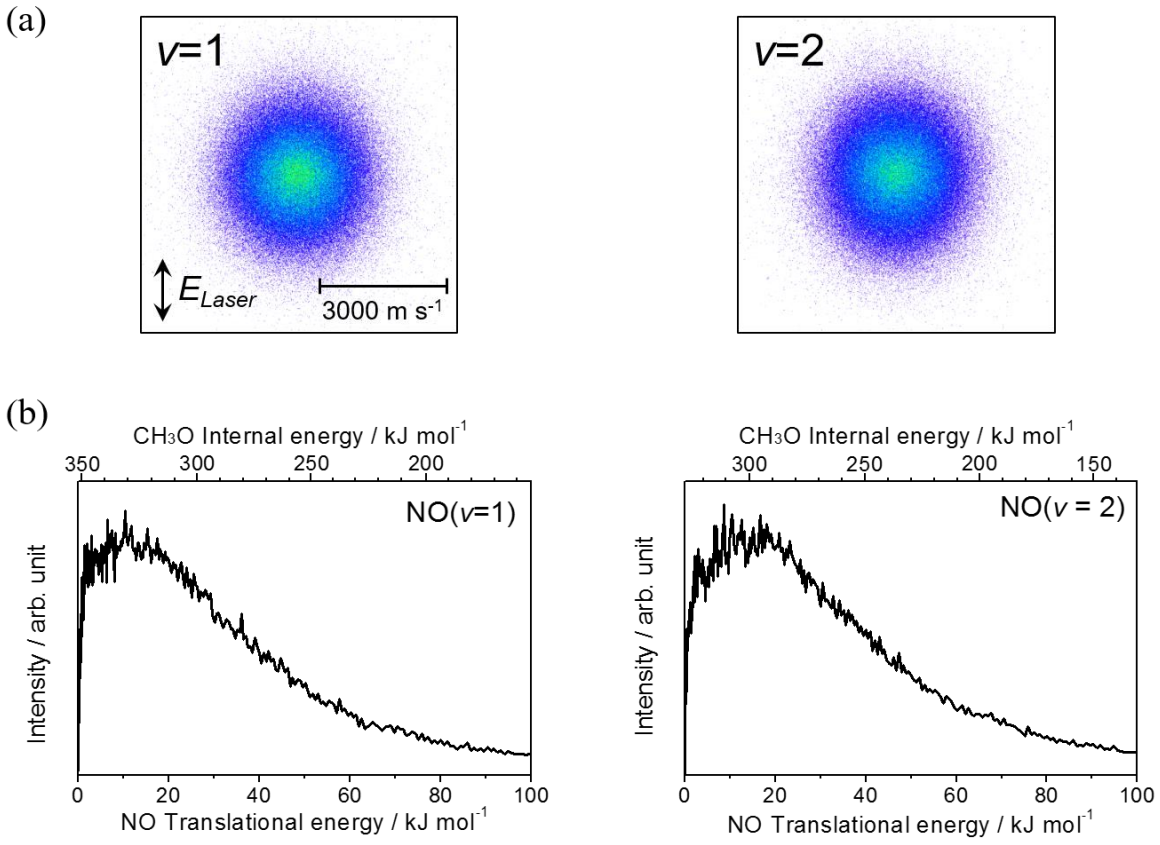

Figure 4.7 (a) State-resolved scattering images and (b) translational energy distributions of the NO photofragment generated in the $v = 1$ and 2 vibrational excited states .

4.3.3 NO ($A\ ^2\Sigma^+$) Fragment

I performed pump-probe measurements for the electronically excited NO($A\ ^2\Sigma^+$) product. The NO($A\ ^2\Sigma^+$) fragment was probed by [1+1]REMPI spectroscopy via the Rydberg states ← $A\ ^2\Sigma^+$ bands in the 330−340 nm region. The observed REMPI spectrum is shown in Figure 4.8. The band positions in this spectrum are identical to those measured in a previous study for photolysis at 193 nm,[61] which was assigned by using a standard formula for the Rydberg series with appropriate molecular constants. The REMPI spectrum of the NO($A\ ^2\Sigma^+$) fragment has a complex rovibrational structure due to photodissociation, which limited our ability to accurately determine the final state distributions. The signal appeared only when the pump-probe delay time was adjusted properly. By varying the delay between the pump and probe laser, I confirmed that the signal exponentially decayed with a time constant of 67 ns ± 5 ns, which corresponds to the radiative lifetime of the $A\ ^2\Sigma^+$ state with substantial rovibrational excitation. The scattering distribution (Figure 4.9 (a)) visibly verifies that the NO($A\ ^2\Sigma^+$) product has a recoil velocity. These results confirm that the 213 nm photodissociation produces NO in the $A\ ^2\Sigma^+$ state.

The $P(E_{trans}^{NO})$ of the NO($A\ ^2\Sigma^+$) fragment (Figure 4.9 (b)) spreads to relatively high E_{trans}^{NO} values of over 80 kJ/mol, which is analogous to those of the NO($X\ ^2\Pi$; $v = 1, 2$) fragment (Figure 4.7 (b)) and the fast component of the NO($X\ ^2\Pi$, $v = 0$) fragment (Figure 4.5 (b)). The peak and average $P(E_{trans}^{NO})$ values of the $A\ ^2\Sigma^+$ and $X\ ^2\Pi$ states (Table 4.2) are accordingly identical to each other within experimental error. The similarity between the NO($A\ ^2\Sigma^+$) and NO($X\ ^2\Pi$) fragments is also observable in their anisotropy parameters, which

exhibit almost isotropic character (Table 4.2).

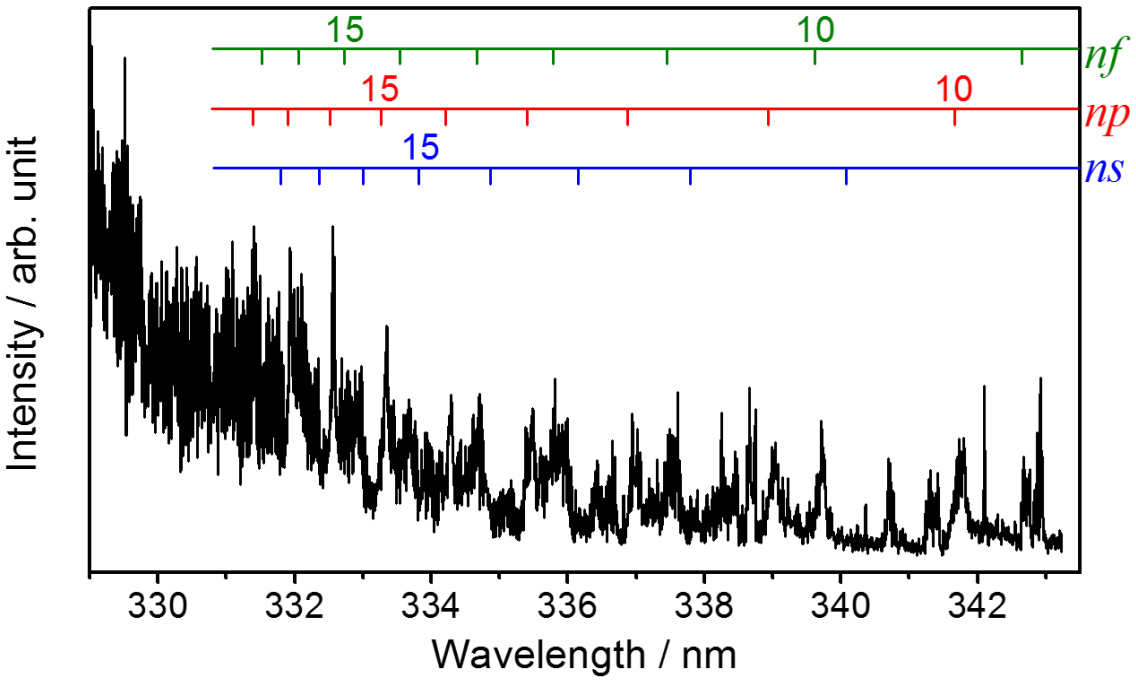

Figure 4.8 [1+1] REMPI spectrum of the NO photofragment generated in the $A\ ^2\Sigma^+$ electronic excited state. The $A\ ^2\Sigma^+ \rightarrow$ Rydberg series transition in the 330 nm region is employed for state-resolved ionization. The shorter wavelength of the spectrum approaches to the ionization continuum.

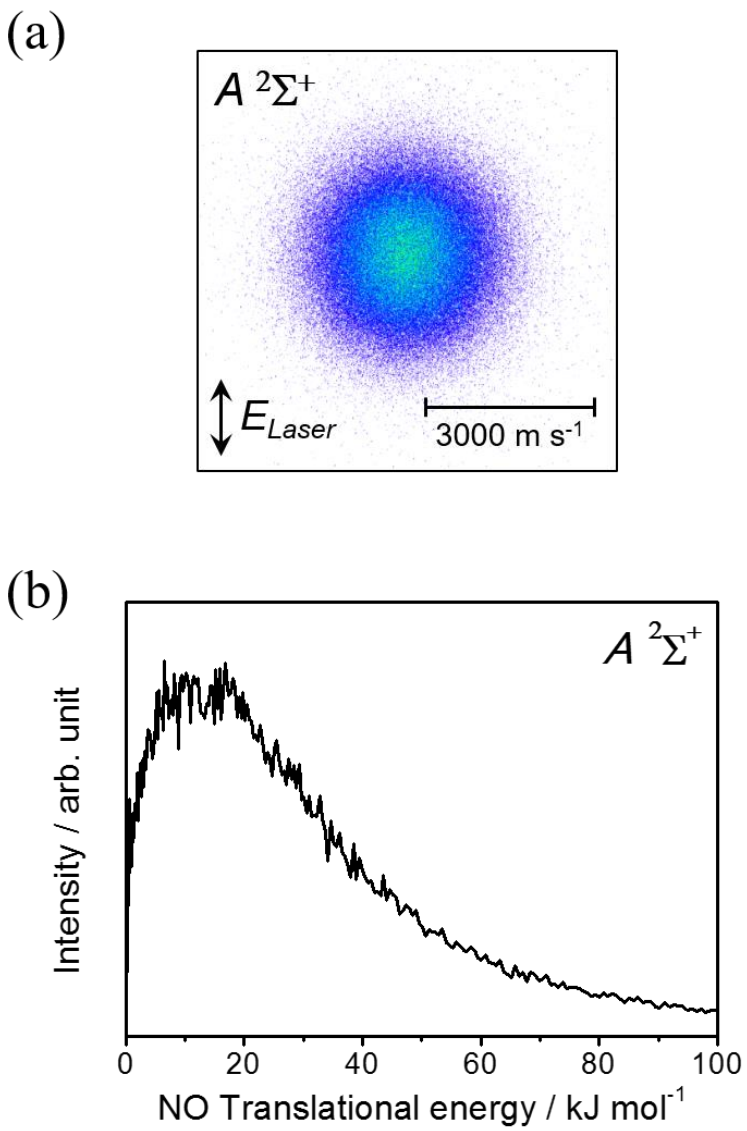

Figure 4.9 (a) Scattering distribution and (b) the translational energy distribution of the NO($A\ ^2\Sigma^+$) photofragment at 213 nm

4.3.4 O(^3P) Atom

The O(^3P_J) photofragments were probed by the [2+1] REMPI scheme via $3p\ ^3P_{J'} \leftarrow 2p\ ^3P_{J''}$ resonant transitions at 225.66 nm for $^3P_2$, 226.06 nm for $^3P_1$, and 226.24 nm for $^3P_0$, in which slightly separated resonance lines (< 0.8 cm^{-1}) associated with the spin-orbit manifold of the upper states were involved in the Doppler broadening. I continuously scanned the probe laser wavelength over all of the Doppler components to obtain the scattering image of the O(^3P_J) photoproduct for each J state.

The scattering images of O(^3P_J) and the $P(E^O_{trans})$ values are shown in Figure 4.10. Using the N−O bond dissociation energy of 418 kJ/mol,[73] the maximum E^O_{trans} value in one-photon (213 nm) dissociation was calculated to be 106 kJ/mol for O($^3P_2$). A large portion of the O(^3P_J) fragment was found within E^O_{trans} < 50 kJ/mol^{-1}. The weak signal with E^O_{trans} > 106 kJ/mol, which was more prominent in the J = 1 and 0 state, clearly represents two-photon dissociation. The angular distribution of the faster O(^3P_J) fragment did not fit to the standard formula for one-photon dissociation (Eq. (2.2)). The anisotropy parameters up to the fourth-order (β_4), which were separately obtained for the slow and fast O(^3P_J) fragment, are shown in Table 4.3.

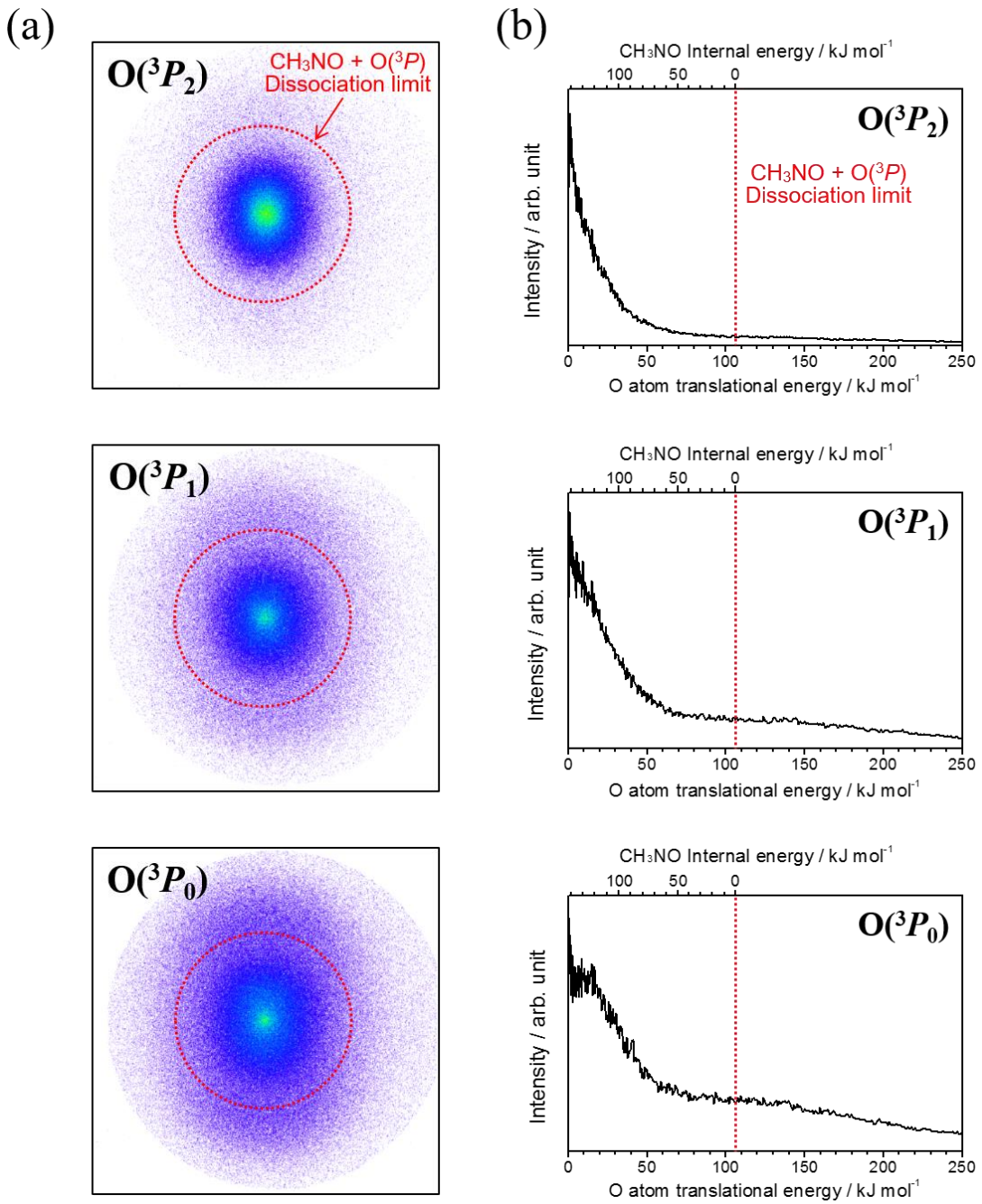

Figure 4.10 (a) State-resolved scattering images of the O($^3P_{J=0,1,2}$) photofragments. The dotted circles indicate the maximum velocity assuming the CH_3NO + O($^3P_{J=0,1,2}$) pathway with one-photon dissociation. (b) Translational energy distributions of the O($^3P_{J=0,1,2}$) photofragments. The upper scales show the internal energy of the CH_3NO counter-product by assuming one-photon dissociation.

Table 4.3 Translational energies and anisotropy parameters of the atomic oxygen O(^3P_J) photofragment

$\lambda_{photolysis}$ (nm)	State	Component	E_{trans} peak (kJ/mol)	$<E_{trans}>$ (kJ/mol)	β_2	β_4
213	$^3P_2$	Slow	7.3	12	0.2	0
		Fast	–	84	0.6	0.5
	$^3P_1$	Slow	5.9	14	0.2	0
		Fast	103	114	0.9	0.2
	$^3P_0$	Slow	10	16	0.2	0
		Fast	91	105	0.9	0.2
226	$^3P_2$	Slow	7.1	11	0.3	0
		Fast	–	73	0.9	0.9
	$^3P_1$	Slow	8.2	11	0.3	0
		Fast	104	116	1.3	0.5
	$^3P_0$	Slow	13.4	18	0.4	0
		Fast	109	115	1.2	0.2

4.4 Discussion

The photochemical processes relevant to the present experimental results are enumerated below.

- C−N bond cleavage

  $CH_3NO_2 + h\nu \rightarrow CH_3 + NO_2$

- Nitrosomethane channel

  $CH_3NO_2 + h\nu \rightarrow CH_3NO + O(^3P_J)$

- Methoxy channel

  $CH_3NO_2 + h\nu \rightarrow CH_3O + NO(X\,^2\Pi)$

- Three-body dissociation

  $CH_3NO_2 + h\nu \rightarrow CH_3 + NO(X\,^2\Pi) + O(^3P_J)$

- Second photodissociation of the primary NO_2 product

  $NO_2 + h\nu \rightarrow NO(X\,^2\Pi) + O(^3P_J)$

- Photoexcitation of the NO product

  $NO + h\nu \rightarrow NO(A\,^2\Sigma^+)$

The energy diagram relating to generation of CH_3, $NO(X\,^2\Pi, A\,^2\Sigma^+)$ and $O(^3P)$ detected in the 213 nm photodissociation is shown in Figure 4.11, where the bond dissociation energies for $CH_3 + NO_2$ referred from the thermochemical data ($\Delta H°$) by Benson,[73] for $CH_3O + NO$ and $CH_3NO + O(^3P)$ in a recent theoretical studies,[65, 66] and for $NO + O(^3P)$ in precise experimental data,[74] are used.

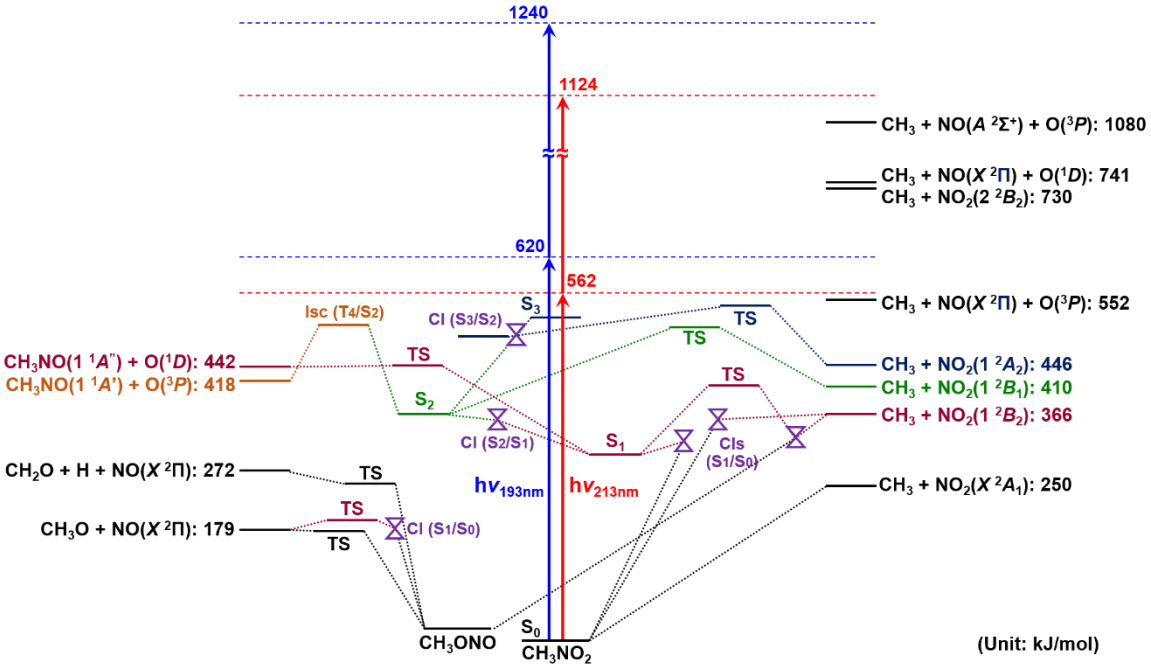

Figure 4.11 Energy diagram for photodissociation of nitromethane

4.4.1 C-N Bond Cleavage Channel ($CH_3 + NO_2$)

Based on the results of early photodissociation studies at 193 nm, the faster CH_3 product has been considered to be the counter-product of electronically excited NO_2 in the primary C−N bond cleavage,[58, 59, 61] although identification of the NO_2 state from among the low-lying excited states (1 $^2B_2$, 1 $^2B_1$, and 1 $^2A_2$) has not been established. The nascent NO_2 exhibits a sufficiently large $E_{int}^{NO_2}$ (shown in the upper scale in Figure 4.3 (b)) to populate any of these excited states, and even the ground ($\widetilde{X}$ $^2A_1$) state. Although the $E_{int}^{NO_2}$ distribution obtained in the imaging results, similar to those of the previous 193 nm studies, is not sufficiently conclusive to identify the states of NO_2, the angular distribution provides insight into the C−N bond cleavage. I examined the differences between of the β values at 193 nm and 213 nm. The β value at 193 nm which was determined to be −0.6 in the state-unresolved experiment[59] and the maximum value of −0.74 that was obtained from the velocity-resolved measurement,[63] are consistent if they are averaged over the velocity. The β value of −0.5 for $CH_3(v = 0)$ at 213 nm is slightly but discernibly larger than the β values at 193 nm. Recent theoretical studies revealed that the photoinitiated state in the $\pi \rightarrow \pi^*$ band is the S_3 state, which was thought to exhibit significantly faster electronic relaxation after photoabsorption;[64-66] the conical intersection was ascribed to the cascading relaxation from the photoinitiated S_3 state to the lower (S_2, S_1, and S_0) states, which correlate to various product pathways.[65, 66] Decrease of anisotropy was explained to be due to the nuclear motions passing the conical intersection.[63] In other words, the variation of β at from 193 nm to 213 nm implies contributions from the $CH_3 + NO_2(1\ ^2B_2)$ or

$CH_3 + NO_2(1\ ^2B_1)$ product pathways, which are adiabatically correlated with the S_1 and S_2 PESs, respectively. Theoretical calculations have indicated that direct dissociation on the S_3 PES, which correlates with $CH_3 + NO_2(1\ ^2A_2)$, is unlikely because the Franck−Condon region of the $S_0 \rightarrow S_3$ photoabsorption is located near the conical intersection of the S_3/S_2 surfaces (CI(S_2/S_3)), which is expected to enable efficient transitions to the lower electronic states.[65, 66] In addition, the high barrier heights calculated for the S_3 (541.4 kJ/mol[65]) and S_2 (506.3 kJ/mol,[66] 435.1 kJ/mol[65]) PESs were considered to make C−N bond cleavage on these PESs less probable. Based on these theoretical considerations, C−N bond cleavage most likely occurs on the S_1 PES and is followed by the $S_3 \rightarrow S_2 \rightarrow S_1$ sequential transitions, as predicted by Isegawa *et al.*[66] The excess energy above the CI(S_2/S_3) is reduced from 136 kJ/mol at 193 nm to 78 kJ/mol at 213 nm using the theoretical energy of the CI(S_2/S_3) (483.7 kJ/mol[66]). The experimental results for the β values at 213 nm and 193 nm indicate that the reduced kinetic energy passing through the CI(S_2/S_3) is preferable for the $S_3 \rightarrow S_2 \rightarrow S_1$ transition. This kinetic energy dependence is not a general attribute to non-adiabatic transitions, implying the significance of the nuclear dynamics involving the $S_3 \rightarrow S_2 \rightarrow S_1$ transition. If the decrease of anisotropy is due to nuclear motions accompanied by electronic relaxation through the CI, the more isotropic angular distribution ($\beta = -0.3$) of the ν_2 excited CH_3 fragment is a reasonable explanation for the significant structural deformation. Although the nuclear dynamics on these PESs are not theoretically supported, this inspection of the angular distributions based on the structures of the calculated PESs indicates that C−N bond cleavage proceeds on the S_1 PES, leading to $CH_3 + NO_2(1\ ^2B_2)$. It is noted that the photon energy given by 193 nm (619.7

kJ/mol) is higher than the calculated barrier heights, allowing participation of the S_2 and S_3 states in the dissociation. A recent result of the speed-dependent bipolar moment recently measured by Rodriguez *et al*. at 193 nm was explained as an evidence of a partial contribution of the S_3 direct dissociation to the $CH_3 + NO_2(1\ ^2A_2)$ pathway.[63]

4.4.2 Nitrosomethane Channel ($CH_3NO + O$)

A fast electronic relaxation cascade, as indicated by theoretical studies, can open the nitrosomethane and methoxy channels. The theoretical study by Arenas *et al*. predicted that the nitrosomethane pathway ($CH_3NO + O(^3P)$) following intersystem crossing from the S_2 state to the T_4 state (ISC(T_4/S_2)), was expected to have an efficient transition probability in spite of its high energy location (510.0 kJ/mol).[65] The available energy for the $CH_3NO + O(^3P)$ pathway has been estimated to be 144 kJ/mol. The $P(E_{trans}^{O})$ of the slower component that extends to E_{trans}^{O} = 50 kJ/mol is reasonably matched with that of the nitrosomethane channel, which should have E_{trans}^{O} < 106 kJ/mol. The internal energy of nitrosomethane product ($E_{int}^{CH_3NO}$), calculated by a formula similar to Eq. (2.1), is indicated by the upper scale in Figure 4.10 (b), providing the internal energy distribution for CH_3NO, $P(E_{int}^{CH_3NO})$. The $P(E_{int}^{CH_3NO})$ distribution indicates that the slower component of the $O(^3P)$ fragment is produced with CH_3NO with $E_{int}^{CH_3NO}$ = 80−140 kJ/mol. This $E_{int}^{CH_3NO}$ region is likely to the CH_3NO photoproduct.

The $O(^3P)$ fragment observed in the 193 nm photodissociation study was attributed to the stepwise three-body dissociation ($CH_3NO_2 + h\nu(193nm) \rightarrow CH_3 + NO_2 \rightarrow CH_3 + NO + O(^3P)$) and the secondary photodissociation of the primary NO_2 product ($CH_3NO_2 + h\nu(193nm) \rightarrow CH_3 + NO_2$, $NO_2 + h\nu(193nm) \rightarrow NO + O(^3P)$).[58, 59, 61] The latter should produce the fast $O(^3P)$ fragment because of the two-photon energy involved, which will be discussed later. For

either the concerted or stepwise three-body dissociation to occur by one-photon at 213 nm, the summation of the translational and internal energies of all of the products should be restricted to the available energy of approximately 10 kJ/mol. Even the slower O(^3P) component in Figure 4.10 is too fast to be explained by the three-body dissociation. Thus, it is reasonable to ascribe to the slower O(^3P) fragment to the CH_3NO + O(^3P) pathway. The CH_3NO product was detected by mass spectrometry in the 193 nm photodissociation study by Guo *et al*.[62] Although the branching ratio was smaller than those of the other pathways, their results furnished experimental evidence of the O atom elimination (*i.e.* CH_3NO channel) in the $\pi \rightarrow \pi^*$ transition. Although the CH_3NO radical was not measured in the present study, the obtained translational energy distribution of the O(^3P) counter-product provides a further confirmation of the CH_3NO + O(^3P) pathway.

4.4.3 Methoxy Channel (CH_3O + NO)

The methoxy pathway (CH_3O + NO) is not a simple bond cleavage but rather a complex process involving a C−N bond cleavage, formation of a new C−O bond, and N−O bond dissociation. The available energy of this pathway is 383 kJ/mol. The faster NO component in the v = 0 state displays a similar E_{trans}^{NO} distribution to those of the v = 1 and 2 states, which exhibit single peaks extending to E_{trans}^{NO} = 80 kJ/mol. The calculated internal energy of the methoxy product ($E_{int}^{CH_3O}$) is shown by the upper scales in Figure 4.5 (b) and 4.7 (b), which show the highly internal excitation (> 250 kJ/mol for v = 0) of the CH_3O product. Although the vibrational and rotational state distributions of the fast NO product were not quantitatively determined, the vibrational excitation (v_{NO} = 22.4 kJ/mol) and the highly rotational excitation in the observed spectrum imply that a fairly large portion of the available energy is partitioned into NO internal energy. The large energy partitioning into the internal energy of the CH_3O and NO products is expected to result from the multiple bond dissociation/formation of the methoxy channel. A theoretical study by Isegawa *et al*. predicted that the CH_3O radical is generated through isomerization and roaming on the ground state PES achieved by cascading electronic relaxation from the S_3 state.[66] The proposed dissociation mechanism that contains multi-stage nuclear motion may show an isotropic angular distribution such as that observed for the faster NO product. It is worth noting that the methoxy channel under collisionless conditions in the $\pi \rightarrow \pi^*$ transition was ruled out by Guo *et al*, who attributed the NO product to the second photodissociation of the primarily produced NO_2 in the 1 $^2B_2$ excited state.[62] This assignment cannot be

excluded based on our experimental results, since the internal and translational energy distributions expected for the NO fragment produced with CH_3O overlap energetically with those of the NO product in the second photodissociation. The faster NO product shows an apparently singly peaked energy disposal without structure, restricting further discrimination of its origin. Direct detection of the CH_3O fragment with spectroscopic methods is desired for complete identification of the methoxy channel.

4.4.4 Three-body Dissociation (CH_3 + NO + O)

The origin of the slower CH_3 product has been long supposed to be a *minor* mechanism of the C−N bond cleavage. In early experimental studies at 193 nm, the peak at low CH_3 translational energy was presumed to be due to the production with a vibronically excited state of NO_2,[59, 61] which was tentatively assigned to be the 2 $^2B_2$ state and was theoretically proposed to be 1 $^2A_2$ state by Arenas *et al*.[64] Also at 213 nm, a slow CH_3 peak with a narrow kinetic energy distribution was obtained in this study (Figure 4.3 (b)). However, the kinetic energies of the slow CH_3 fragment at 213 nm and 193 nm are nearly identical (peaked at 1 kJ/mol and 6 kJ/mol, respectively) compared to the energy difference between these photon energies (hν(193nm) – hν(213nm) = 58 kJ/mol), indicating no particular vibronic state of NO_2 that can be commonly ascribed as a counter-product of the slow CH_3.

Alternatively in our previous study, I tentatively proposed the concerted three-body dissociation as the origin of the slow CH_3, NO and O(^3P) products, whose threshold energy is estimated to be 552 kJ/mol.[73, 74] The concerted dissociation of the non-equivalent bonds (*i.e.,* C−N and N−O) is atypical, requiring a specific PES geometry. Butler *et al*. indicated the possibility that the internal conversion to the ground state can produce the slow CH_3 fragment.[59] The fast electronic relaxation through conical intersections was recently illustrated by the high-level *ab initio* calculations.[65, 66] A large excess energy given to the nuclear motions by the relaxation would enable the wide dispersion of the trajectories on the S_0 PES leading to various pathways. Although indirect, preconditions of the concerted three-body dissociation was theoretically indicated.

The present rovibrationally state-resolved measurement results show that CH_3 with low kinetic energy is generated in the low internal states (shown in Figure 4.3 (b)). The slower component of the NO fragment was observed only in the $v = 0$ state (Figure 4.5). Although the rotational structure of the REMPI spectrum is a mixture of both fast and slow components, the dominance of the slower part in the NO scattering images of the lower rotational states (Figure 4.5 (a)) implies that the NO product with low kinetic energy has a relatively colder internal energy distribution. However, the slower O(^3P) fragment with E_{trans}^{O} < 10 kJ/mol which would be produced with the slower CH_3 and NO fragments in the concerted three-body dissociation was not discernible in the present data. This result can be interpreted in two ways: (1) since the branching ratio of the concerted three-body dissociation is much smaller than that of the nitrosomethane channel, the sharp peak due to the concerted three-body dissociation is hidden within the large signal of the slower O(^3P) fragment of the nitrosomethane channel; (2) the slower CH_3 and NO fragments are generated in the stepwise three-body dissociation via the nitrosomethane channel, *i.e.*, $CH_3NO_2 + h\nu \rightarrow CH_3NO + O \rightarrow CH_3 + NO + O$. In this pathway, the CH_3NO product with an internal energy higher than the C−N bond dissociation barrier decomposes into CH_3 and NO($X\,^2\Pi$), which is consistent with the fact that no sharp, slow peaks appear in the observed $P(E_{trans}^{O})$. Arenas *et al*. theoretically predicted that due to the low barrier, the CH_3NO ($1\,^3A''$) photoproduct spontaneously dissociates into CH_3 + NO.[65]

The accuracy of the energy threshold data is crucial for our proposal of the three-body dissociation, in which the sum of the translational and internal energies of all of the slow products should exactly fall within the available

energy. Although calculation using the enthalpy of formation in standard conditions ($\Delta_f H°$) yielded 566.16 kJ/mol as the threshold energy for the CH_3 + NO + O(^3P) pathway, $\Delta_f H°(NO_2 \rightarrow NO + O)$ overestimated the corresponding bond dissociation energy (D_0) by 5.8 kJ/mol. By using experimental data for D_0(NO−O)[74] and the thermochemical data of Benson,[73] the threshold energy was evaluated to be 552 kJ/mol. This evaluation yielded E_{avail} = 10 kJ/mol for the CH_3 + NO + O(^3P) pathway at 213 nm, giving a consistency between the experimental data obtained in this study and our interpretation. The slow component of the CH_3 fragment decreases with higher N rotational states and nearly vanishes in states higher than the (v = 0, N = 12) state, whose internal energy is 9.5 kJ/mol, as shown in Figure 4.3 (b). The energy constraint of the three-body dissociation more strictly excludes the NO(v = 1) product, whose vibrational energy is 22.4 kJ/mol. The observed scattering distributions of the NO(v = 1) state (Figure 4.7) consistently exhibits no slow component.

The slower CH_3 fragment was attributed to the parent cluster dissociation by multiphoton absorption in the photodissociation study at 193 nm by Rodriguez *et al.*[63] This conclusion was made based on their experimental results at different pump laser intensities and molecular beam temperatures. The experimental data at 193 nm were measured with a sample gas concentration of 10 %, whereas I used a much more diluted sample with a gas concentration of 0.5 %, which may be less favorable for cluster formation. The pulse energy of the pump laser in our experiment was comparable to or lower than that of the experiment at 193 nm. In order to examine the effects of the different experimental conditions, I performed the measurements while varying the stagnation pressure and the delay time between the pulsed valve and pump laser

pulses; the results demonstrated that the ratio between the intensities of the slower and faster CH_3 was hardly affected. Thus, I did not attributed the sharp peak of the slower CH_3 component at 213 nm to the parent cluster dissociation but rather to another dissociation pathway that produces the faster CH_3 component. The similar isotropic angular distributions of the slow CH_3 and NO products are consistent with their identical production origin, supporting the concerted three-body dissociation process of $CH_3 + NO(X\,^2\Pi) + O(^3P)$.

4.4.5 Second Photodissociation of the Primary NO_2 Product

The translational energies of a portion of the observed O(^3P) fragments exceeded the maximum value in the nitrosomethane channel (106 kJ/mol), which should produce the fastest O(^3P) assuming one-photon dissociation. The two-photon process was first elucidated by Butler *et al.* in the 193 nm photodissociation study;[59] the first photon produces NO_2, and the second photon is absorbed by the primary NO_2, leading to second photodissociation ($CH_3NO_2 + h\nu \rightarrow CH_3 + NO_2$ followed by $NO_2 + h\nu_{2nd} \rightarrow NO + O(^3P)$ within the same laser pulse). Although this successive photodissociations of the parent and product may be an experimental artifact, the extremely large absorption cross-section of the vibronically excited NO_2 product (NO_2^{**}) in the primary C−N bond cleavage inevitably causes the second photodissociation. Moss *et al*.[61] first proposed that the electronic state of the primary NO_2^{**} product which strongly absorbs the second photon is 2 $^2B_2$. However, the theoretical investigation by Arenas *et al*. indicated that 1 $^2A_1$ electronically (or optically) relaxed from 1 $^2B_1$ is a possible candidate for the initial state of the second photodissociation.[64] The fast O(^3P) fragment with E_{trans}^{O} = 70−250 kJ/mol observed at 213 nm exhibits a peculiar angular distribution that could not be fitted by Eq. (2.2). This discrepancy is considered as a result of composite photodissociations. Since the angular distribution of the nascent NO_2 fragment must be identical to the perpendicularly biased distribution of the CH_3 counter-product (Figure 4.3) in the C−N bond cleavage, the apparent parallel distribution is attributable to the second photodissociation ($NO_2^{**} + h\nu_{2nd} \rightarrow NO + O(^3P)$). The observed anisotropy of the second photodissociation would be useful for identifying the primary NO_2^{**} pathway among the possible states: the ground and

low-lying excited (1 $^2A_2$, 1 $^2B_1$, 1 $^2B_2$) states, if the scattering data of the electronically excited NO_2 are available for reference.

Guo *et al*. ascribed the absorbing state of NO_2^{**}, which is the nascent state of the C−N bond cleavage, to NO_2(1 $^2B_2$).[62] The rotational temperature of the thus generated NO(v = 0) fragment was determined to be 600 K in the 226 nm study, which is comparable to that determined in this study at 213 nm. However, the rotational temperature is not conclusive enough to identify the nascent state of NO_2^{**}. The theoretical study suggested that the second photon absorption occurs after electronic relaxation via conical intersection,[65] implying the significance of the preceding electronic dynamics. Determination of the temporal properties of the transient NO_2^{**} is beyond the present study. These properties will be clarified by time-resolved experiments as well as dynamics calculations, yielding a full characterization of the primary C−N bond cleavage and the subsequent second photodissociation.

4.4.6 Production of NO($A\ ^2\Sigma^+$)

It is clear that the NO($A\ ^2\Sigma^+$) fragment is also generated by a two-photon process since the term energy of the $A\ ^2\Sigma^+$ state of 529 kJ/mol is too large for one-photon dissociation at 213 nm (hν(213 nm) = 562 kJ/mol). I found that the translational energy distributions and anisotropy parameters of the NO($A\ ^2\Sigma^+$) and the faster components of the NO($X\ ^2\Pi$) photofragments are similar. The latter is ascribed to the methoxy channel as discussed above. This similarity suggests that the products are generated through the same dissociation process. I suggest that the NO($A\ ^2\Sigma^+$) product is generated by the photoexcitation of the NO($X\ ^2\Pi$) fragment with an additional 213 nm photon within a single laser pulse. Because no kinetic energy is released by an optical excitation, the NO($A\ ^2\Sigma^+$) fragment is thought to exhibit a translational energy distribution identical to that of the NO($X\ ^2\Pi$) fragment. The 213 nm wavelength is located in the $A\ ^2\Sigma^+$, $v - 1 \leftarrow X\ ^2\Pi$, v transition region. Highly rotational excitation of the NO($X\ ^2\Pi$; $v = 0, 1, 2$) product as well as the strong absorption of the $A\ ^2\Sigma^+ \leftarrow X\ ^2\Pi$ band can contribute to this accidental transition.

The NO($A\ ^2\Sigma^+$) product in the laser photodissociation of CH_3NO_2 was first detected at 193 nm by Moss *et al*.[61] They proposed that the NO($A\ ^2\Sigma^+$) product originated from the second photodissociation of the primary NO_2^{**} ($NO_2^{**} + h\nu_{2nd} \rightarrow NO(A\ ^2\Sigma^+) + O$) within a single laser pulse. Since the relevant photoabsorption was not theoretically confirmed, others have suggested that the secondary photodissociation of the CH_3NO radical is the origin of NO($A\ ^2\Sigma^+$) product, *i.e*., $CH_3NO + h\nu_{2nd} \rightarrow NO(A\ ^2\Sigma^+) + CH_3$.[65] However, the corresponding signal was not found in the scattering distribution of the CH_3 counter-product in our investigation. In addition, the observed velocity of the NO(A

$^2\Sigma^+$) product velocity was too fast to verify the $CH_3NO + h\nu_{2nd} \rightarrow NO(A\ ^2\Sigma^+) + CH_3$ pathway; the total available energy in the $CH_3NO_2 + 2h\nu \rightarrow NO(A\ ^2\Sigma^+) + CH_3 + O(^3P)$ pathway is estimated to be 44 kJ/mol irrespective of the intermediate step, which is too small to produce $NO(A\ ^2\Sigma^+)$ fragments with translational energies as high as 80 kJ/mol (shown in Figure 4.9 (b)).

4.5 Conclusion

I measured the REMPI spectrum and the state-resolved velocity and angular distributions of the CH_3, NO($X\,^2\Pi$, $A\,^2\Sigma^+$) and O(^3P) fragments generated by the photodissociation of CH_3NO_2 at a photolysis wavelength of 213 nm. The internal and translational energy distributions of these photofragments corroborate the existence of several competing product pathways in the $\pi \rightarrow \pi^*$ transition. The CH_3 fragment showed two energy components. The fast CH_3 fragment with a negative β parameter is ascribed to the C−N bond cleavage on the S_1 PES producing to $CH_3 + NO_2(1\,^2B_2)$. I propose the three-body dissociation, $CH_3NO_2 + h\nu \rightarrow CH_3 + NO + O(^3P)$, as the origin of the slow and internally cold CH_3 product. The detection of the slow and cold NO fragment in this study is attributed to the second product of the three-body dissociation. Due to the absence of the slow O(^3P) fragment as the third product in the measurement, a stepwise or concerted way in the three-body dissociation was not determine. The energy partitioning obtained from the state-resolved scattering data of the O(^3P) fragment is reasonably understood to result from the nitrosomethane channel, *i.e.*, $CH_3NO_2 + h\nu \rightarrow CH_3NO + O(^3P)$. The large internal excitations of the NO products found in the $v = 1$ and 2 states and the faster NO($v = 0$) component indicate that the reaction occurs through the methoxy channel, *i.e.*, $CH_3NO_2 + h\nu \rightarrow CH_3O + NO$. Since the translational energy distribution of the fast NO fragment overlapped with the energy region due to a different origin of NO (*i.e.* second photodissociation), I cannot uniquely assign the fast NO to the methoxy channel. However, the internal energy distribution of the hot products is reasonably interpreted as the mechanism of the methoxy

channel that should involve a multiple bond dissociation/formation. The second photodissociation of the primary NO_2 product, $NO_2^{**} + h\nu_{2nd} \rightarrow NO + O(^3P)$, which was argued in the data analysis of the previous 193 nm photodissociation studies, is also observed here in the 213 nm experiment. The translational energy of the faster $O(^3P)$ component was too large to be ascribed to the one-photon dissociation pathway. The angular distribution, which was not well fitted with the Legendre function, supports the two-stage dissociation to produce the fast $O(^3P)$ fragment. Generation of the NO fragment in the $A\ ^2\Sigma^+$ electronic excited state also requires two-photon energy. I measured the REMPI spectra of the Rydberg $\leftarrow A\ ^2\Sigma^+$ bands, which reproduced the previous measurements performed at 193 nm. Since the NO($A\ ^2\Sigma^+$) product yielded a scattering distribution similar to those of the NO($X\ ^2\Pi$) fragments, the NO($A\ ^2\Sigma^+$) fragment may be generated by the $A\ ^2\Sigma^+ \leftarrow X\ ^2\Pi$ photoabsorption of the NO($X\ ^2\Pi$) fragment within the same laser pulse.

Chapter 5.

S_2 Photodissociation Dynamics of Methyl Nitrite: Internal State and Velocity Distributions of Photoproducts

5.1 Introduction

Dissociation dynamics of a polyatomic molecule is drastically influenced by potential energy surface (PES) structure and interaction. As shown in Figure 5.1[75], methyl nitrite (CH_3ONO) has two photoabsorption bands in near-UV region which correlate to the transitions to two different electronic excited states, S_1 and S_2 states, respectively. Since the S_1 and S_2 states involve significantly different dissociation mechanisms, great attention has been paid to both experimental[76-104] and theoretical[105-109] researches on the photodissociation dynamics of CH_3ONO to get deep insight into the dynamical interactions in the polyatomic molecular dissociation. The weak structured band in the 300-400 nm region is assigned to the $S_0 \rightarrow S_1$ transition with $n\pi^*$ character, which is out-of-plane and localized on the N=O moiety. In contrast, the strong unstructured band centered near 210 nm is assigned to the $S_0 \rightarrow S_2$ transition with $\pi\pi^*$ character, which is in-plane and delocalized. Although the electronic character of the S_1 and S_2 is significantly different, both the electronic excited states give rise to the same dissociation reaction,

$$CH_3ONO + h\nu \rightarrow CH_3O + NO$$

after a photoexcitation and produce a methoxy radical (CH_3O) and a nitrogen oxide (NO) fragments.

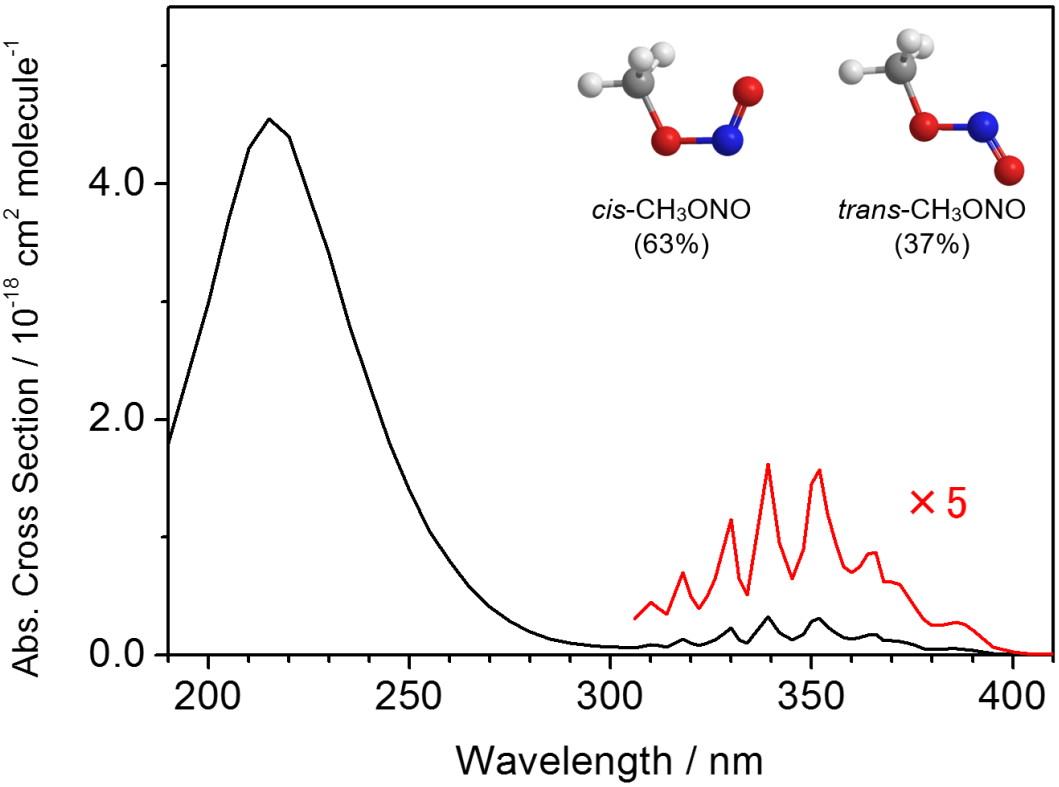

Figure 5.1 UV photoabsorption spectrum of CH_3ONO. Red line indicates the same absorption spectrum as black line with a 5-fold enlarged scale.

A number of experimental[76-96] and theoretical[105-109] groups have extensively investigated the photodissociation dynamics of CH_3ONO at the $S_0 \rightarrow S_1$ absorption band, which is regarded as a prototype model for studying the vibrational predissociation in an excited electronic state. The vibrational progression observed in the $S_0 \rightarrow S_1$ absorption band of nitrous acid (HONO) and its alkyl ester derivatives (RONO) were ascribed to the local excitation of the N=O stretching mode[76]. Radhakrishnan and Estler[85] observed the non-thermal rotational distribution of the NO fragment at 383 nm by using a multiphoton ionization technique. Inoue and coworkers[86] measured the translational energy and angular distributions of the NO fragment at 348-368 nm and pointed out

that the transition moment lies perpendicular to the O–N bond to be dissociated. Lahmani and coworkers[87-90] measured the two-photon laser-induced fluorescence (LIF) spectrum of the NO fragment at the several photoexcitation peaks between 314-368 nm assigned to the specific N=O stretching vibrational levels. They also conducted the polarization experiment and found the stereospecific behavior of the O–N bond dissociation of CH_3ONO. Hippler and coworkers[91-94] employed LIF and REMPI spectroscopy and measured the vibrational state distributions of the NO fragments produced by the photodissociation of CH_3ONO in a supersonic free-jet expansion at 355, 380, 387 nm. Their experimental results indicate that the photoinitiated N=O stretching motion of CH_3ONO in the S_1 state is preferentially retained during the O–N bond dissociation and influences the final vibrational state distribution of the NO fragments. Reid and coworkers[95] measured the state specific photofragment yield (PHOFRY) spectra of jet-cooled CH_3ONO. The spectral peak width independence of the monitored NO rotational level implied that non-adiabatic vibrational predissociation proceeded. Mestdagh and coworkers[96] carried out the photodissociation experiment at 351 nm by using a time-resolved LIF technique with ultrashort laser pulses. They detected the NO product and determined the dissociation time (125 fs) of the parent molecule in the S_1 state. Huber and his group[77-84, 105-109] performed a number of experiments on the S_1 photodissociation and calculations on the S_1 potential energy surface (PES). They measured the translational energy and angular distributions of the photofragments and internal state distribution of the NO photoproduct at the $S_0 \rightarrow S_1$ absorption band and carried out the polarization experiment. They also per-

formed calculations of the S_1 PES and dynamical calculations with for investigating the vibrational predissociaiton process of CH_3ONO in S_1 state. It has been concluded that the dissociation of CH_3ONO on the S_1 PES which has a shallow minimum near the Franck-Condon region, as shown in Figure 5.2, is governed by vibrationally nonadiabatic predissociaiton, and consequently the NO fragment is produced with small vibrational energy but high rotational and translational energy.

The $S_0 \rightarrow S_2$ photodissociation has been investigated by less number of researches[97-104] than the $S_0 \rightarrow S_1$ photodissociation. Contrast to the indirect photodissociation dynamics in the S_1 state, the dynamics in the S_2 state is characterized as a rapid direct dissociation. Winniczek and coworkers[97] employed REMPI spectroscopy and measured the NO fragment rotational state distribution at the photolysis wavelength ranging 223-227 nm region. The NO fragments were found to be produced in their ground electronic states but with high rotational and translational energy. They also investigated the spatial alignment by the circularly dichroic angular distribution techniques and pointed out that the angular momentum vector is perpendicular to the photolysis transition dipole moment. Farmanara and coworkers[98] directly determined the lifetime of CH_3ONO photoexcited to the S_2 state as (25 ± 15) fs in the ultrafast pump-probe experiment with 125 fs laser pulses. Yin and coworkers[99] measured the relative internal state distribution of the NO($X\,^2\Pi$; v=0, 1, 2, 3) fragment produced by the 266 nm photolysis of CH_3ONO by using LIF spectroscopy. They found that the NO($X\,^2\Pi$) fragments were mainly populated in the ground vibrational state and exhibited considerably hot rotational distributions in each vibrational level. They also investigated the rotational alignment of the NO(X

$^2\Pi$) fragments by the polarized LIF spectroscopy. Their polarization experiment indicated that the angular momentum vector of the recoiling NO($X\,^2\Pi$) fragments was aligned perpendicularly to the transition moment of the parent molecule. Yue and coworkers[100, 101] conducted the CH_3ONO photodissociation experiment under bulk condition at 266 nm and observed a LIF spectrum of OH($X\,^2\Pi$) fragment. They has performed density functional theory (DFT) calculations for CH_3ONO molecule and proposed a photodissociation mechanism involving an intramolecular hydrogen atom transfer process for the OH product pathways. Huber and his group[102, 104] measured photofragment translational energy and angular distributions of series of alkyl nitrites (RONO) at 248 and 193 nm with a molecular beam time-of-flight (TOF) apparatus. The large positive anisotropy parameter which was determined by the angular distribution implied that the transition moment is almost parallel to the fragment recoil direction and dissociation occurs on a strongly repulsive potential energy surface. They also calculated the S_2 potential energy surface of CH_3ONO for the N=O bond length, $R_{N=O}$, and the O–N bond length, $R_{O–N}$, coordinates using the MCSCF ab initio method.[103] It has been concluded that the fast direct photodissociation occurs on a repulsive S_2 PES, which is a steeply decreasing function along $R_{O–N}$, as shown in Figure 5.2, and has the same minimum for $R_{N=O}$ as the S_0 state near the Franck-Condon region. They also predicted an anticorrelation between the internal energies of a fragment pair to explain the decrease of the widths of the photofragment translational energy distributions with increasing size of the alkyl (R–) group.

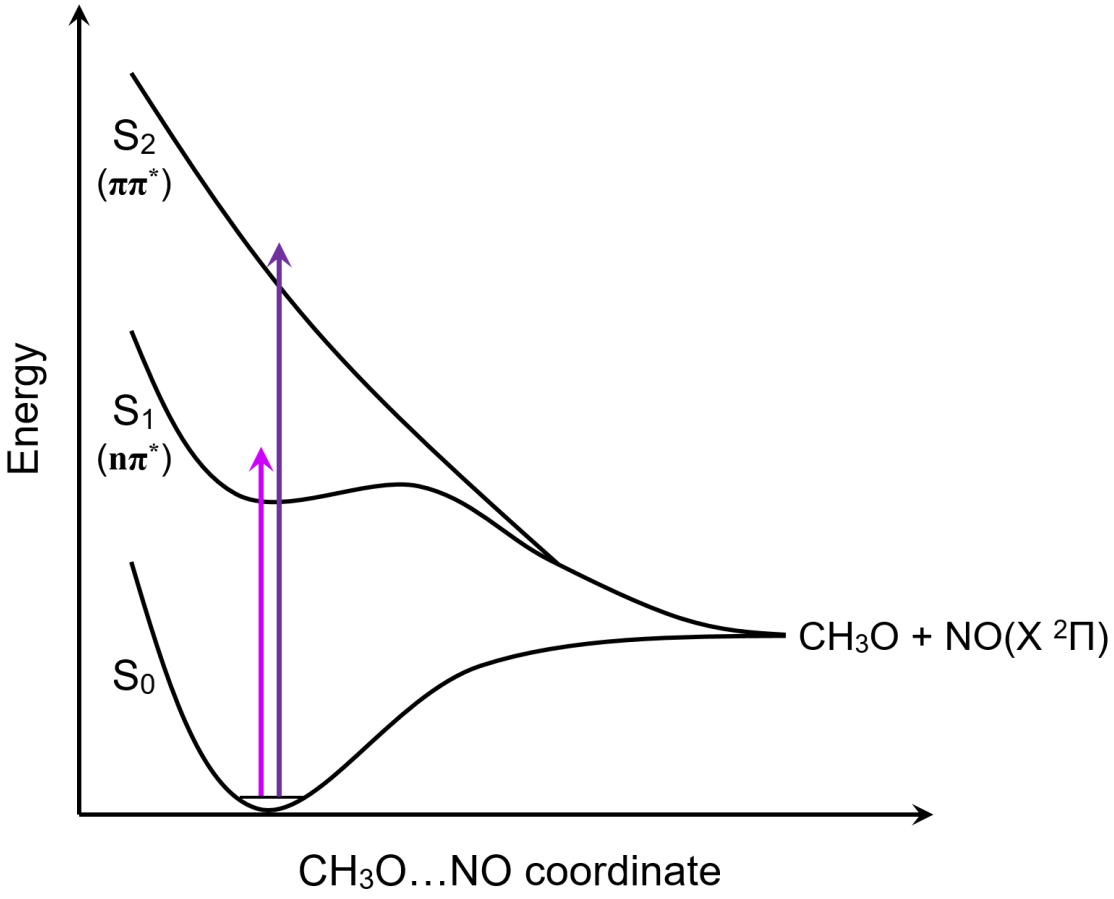

Figure 5.2 Schematic view of the PESs of CH_3ONO

In the present study, I have carried out the pump-probe experiments on the CH_3ONO photodissociation at photolysis wavelength of 213 nm, which is near the absorption peak of the $S_0 \rightarrow S_2$ transition. The internal state distributions of the NO($X\,^2\Pi$) fragment and CH_3O($X\,^2$E) fragment were measured using a REMPI and a single photon LIF techniques, respectively. The scattering distributions of the NO($X\,^2\Pi$) fragments in several rovibrational states were state-selectively observed by VMI method. On the basis of the energy conservation law, the internal energy distribution of the CH_3O counter product has been calculated, and then the internal energy correlation between the NO and CH_3O photoproducts has been investigated. Furthermore, the alignment effects of the recoiling photofragments were investigated with a circularly polarized laser for probing the NO($X\,^2\Pi$) fragment in a highly excited rotational state.

5.2 Experimental

The experimental apparatus and laser setup were explained in detail in Section 2.1. CH_3ONO was prepared by a standard organic synthesis. Under stirring, a solution of H_2SO_4 (50% in water) was slowly added into a saturated solution of sodium nitrite ($NaNO_2$) in methanol (CH_3OH). The formed CH_3ONO, which is gaseous at room temperature, was diluted to 0.5 % and 2 % with helium gas without further purification for using in an ion detection experiment and a LIF experiment, respectively. The sample gas was used at a stagnation pressure of 2 atm. During introducing the sample gas into the source chamber, the inner pressure in source chamber was kept at 4×10^6 Torr and 1×10^5 Torr in an ion detection experiment and in a LIF experiment, respectively, while the inner pressure in the detector chamber was kept in the range of 10^7 Torr in both experiments.

In the ion detection experiment, both a pump and probe lasers were focused with quartz lenses (f = 350 mm). The pulse energy of the photolysis laser was varied from 10 μJ/pulse to 30 μJ/pulse, while that of the probe laser was less than 10 μJ/pulse for ionizing the NO fragment by [1+1] REMPI spectroscopy via the $A\ ^2\Sigma^+ \leftarrow X\ ^2\Pi_\Omega$ transition. When the REMPI spectrum was measured, the pulse energies of the pump and probe laser were monitored with a photodiode for confirming them kept sufficiently constant in a measurement. When the scattering distribution was measured, the probe laser wavelength was repetitively scanned over the Doppler width of the photofragment rotational line as the line profile and the images were recorded. The probe laser was circularly polarized using a Berek polarization compensator (New Focus, Model 5540) to examine rotational alignment effects of the recoiling NO fragment.

The probe laser wavelength for detecting NO(v = 0-3) was located in the range of 218-258 nm, which was considerably overlapped with the $S_0 \rightarrow S_2$ absorption bands of CH_3ONO. This made the experimental conditions and analysis difficult. The total NO ion signal contained 30-50% one-color laser component, which was originated by only the probe laser. In addition, the scattering distribution of the NO fragment produced by only the probe laser was considerably overlapped with that produced by the pump and probe lasers. If the laser power of the pump pulse had been strong for increasing the total signal with respect to one-color signal, the NO fragment would has been excited to the $A\ ^2\Sigma^+$ state by absorbing another pump laser photon since the pump laser wavelength was located in the region of the $A\ ^2\Sigma^+, v - 1 \leftarrow X\ ^2\Pi_\Omega, v$ transition. Therefore, the power balance between the pump and probe laser pulse was crucial in the experiment. Since the one-color signal was not negligible, I needed to record the ratio of one-color signal to total signal and evaluate the REMPI spectrum and the recoil velocity distribution of the NO fragment by subtracting the one-color signal weighted by the ratios from the total signal.

In a LIF experiment, both pump and probe laser beams were introduced into the source chamber without focal lenses. The CH_3O fragment was resonantly excited via the $\tilde{A}\ ^2A_1 \leftarrow \tilde{X}\ E_2$ transition. The fluorescence from the photoexcited CH_3O fragment was collected by a focal lens (f = 30 mm) and passed through a B460 glass filter and U330 glass filter (HOYA) to a PMT. The pulse energy of the photolysis laser was varied from 600 μJ/pulse to 800 μJ/pulse, while that of the probe laser was varied 200 μJ/pulse to 600 μJ/pulse in the measurement.

5.3 Results and Discussion

5.3.1 Final State Distributions

Figure 5.3 (a) shows observed [1+1] REMPI spectra of the NO photofragment in the v = 0-3 states. Further stronger signal intensity was observed in the $0^{'}$-$1^{''}$ band than other bands. This result clearly indicates that the v = 1 level is preferentially populated among the v = 1-3 levels due to the small difference between the Franck-Condon factors[110] of those bands, which is shown in Table 5.1. The REMPI signal of the NO(v = 0) photofragment was not sufficiently enhanced by the pump and probe laser pulses probably due to the overlap of the probe laser wavelength required to ionize NO(v = 0) with the peak region of the $S_0 \rightarrow S_2$ absorption band of CH_3ONO. However, the intensity of the v = 1 is estimated to be at least six times stronger than that of the v = 0. This suggests the inverted population between the v = 0 and 1 levels due to small difference of the Franck-Condon factors between the $0^{'}$-$0^{''}$ and $0^{'}$-$1^{''}$ bands. The REMPI spectrum of each state was repetitively measured more than three times and averaged for decreasing measurement errors originating from the fluctuation of the laser pulse intensity. For evaluating the one-color laser signal ratio to total signal, $I_{1\ color}/I_{total}$, in each REMPI spectrum, the REMPI spectra were measured in both pump-probe and probe-only experiments under the same other conditions. The value of $I_{1\ color}/I_{total}$ was dependent on both the pump and probe laser powers. The area intensity, S(v), of each vibrational band was weighted by a one-color laser signal ratio to obtain a pure two-color laser signal intensity. Then, based on Franck-Condon considerations, the relative vibrational state populations, P(v), in the v = 1-3 states were determined as 0.73, 0.21 and 0.06, which are also summed in Table 5.1. Table 5.2 shows the P(v)

measured at several photolysis wavelengths[99, 103] in the $S_0 \rightarrow S_2$ absorption band. At the photolysis wavelengths of 248 and 266 nm, which are located at the red tail in the $S_0 \rightarrow S_2$ absorption band, more than half of the NO photoproducts were populated in the $v = 0$ state. Although the accurate P(0) value cannot be estimated at 213 nm, which located at the peak in the $S_0 \rightarrow S_2$ absorption band, the stronger signal of the $0^{'}$-$1^{''}$ band than $0^{'}$-$0^{''}$ band implies the inverted population between the $v = 0$ and 1 levels. It suggests that the amount of the excess energy increase on the S_2 PES by the increase of the photon energy is preferentially deposited into the N=O bond stretching motion. Huber and coworkers[103] predicted that the S_2 PES induces small N=O bond oscillation as the increase of the O–N bond length from the Franck-Condon region.

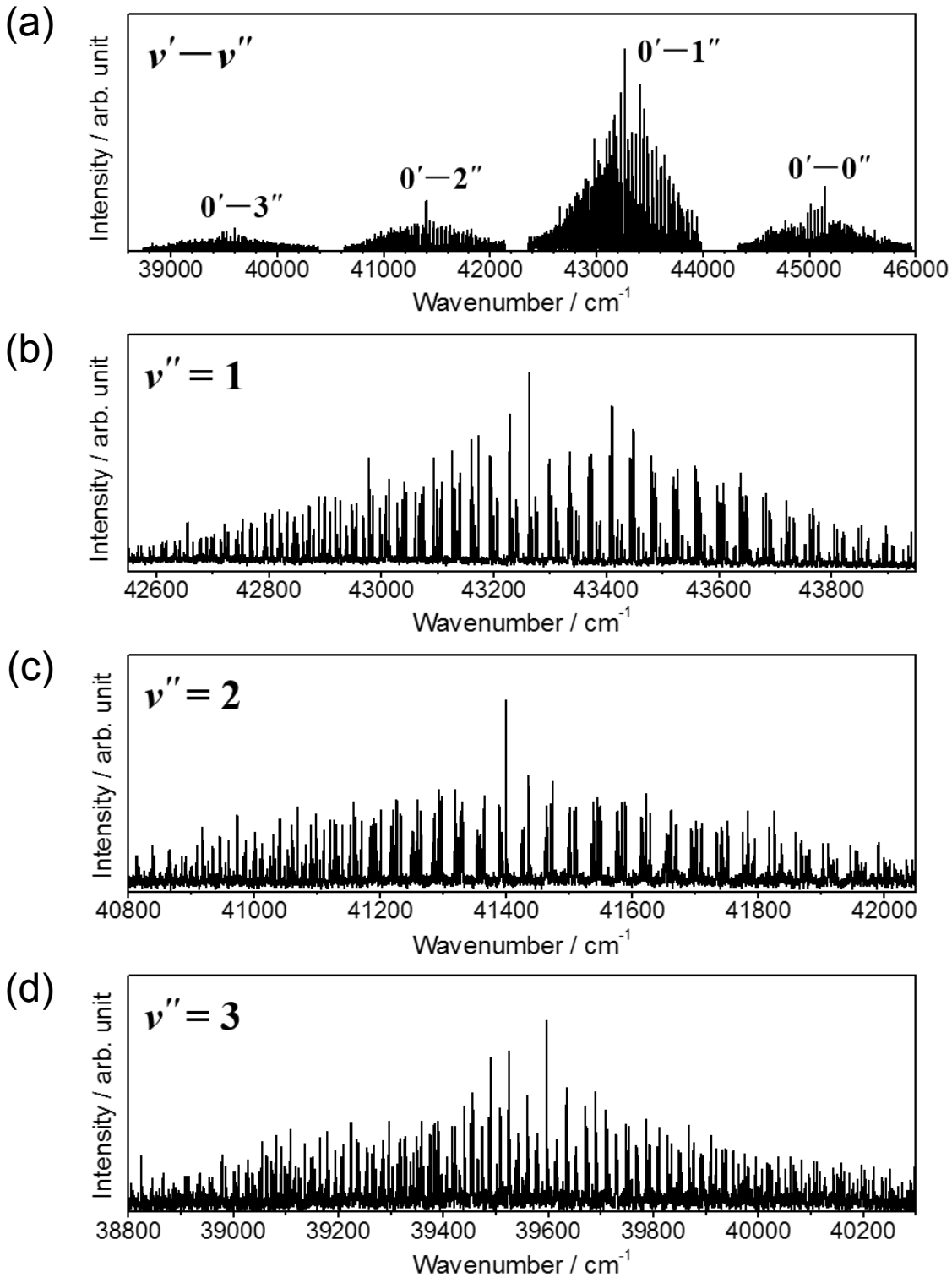

Figure 5.3 (a) [1+1] REMPI spectra of the NO photofragment in $v = 0$-3 states. The REMPI spectral intensity of each vibrational state was normalized with that of the $v = 1$ state. The REMPI spectra with an enlarged wavenumber scale of the NO photofragment in (b) $v = 1$ (c) $v = 2$, and (d) $v = 3$ state were shown.

Table 5.1 The value of the S(v = 1, 2, 3) and the P(v=1, 2, 3) of the NO photo-fragment at 213 nm.

	S(v)	$I_{1\ color}/I_{total}$	Franck-Condon factor [a]	P(v)
v = 0			0.167	
v = 1	1.00	0.39	0.265	0.73
v = 2	0.219	0.30	0.237	0.21
v = 3	0.118	0.75	0.160	0.06

[a] Reference 110.

Table 5.2 The P(v) value measured at the photolysis wavelengths of 213, 248, and 266 nm, which located in the $S_0 \rightarrow S_2$ absorption band.

	v = 0	v = 1	v = 2	v = 3
266 nm [a]	0.50	0.22	0.16	0.12
248 nm [b]	0.76	0.24	0	
213 nm [c]		0.73	0.21	0.06

[a] Reference 99.

[b] Reference 104.

[c] This work.

The REMPI spectra of the NO fragment in the v = 1-3 states were shown in Figures 5.3 (b)-(d) with enlarged wavenumber scales. All rotational lines were broadened by the Doppler effect, but they were sufficiently separated each other to allow one to assign each peak and obtain a peak area intensity by fitting with a Gauss function. The intensity of each peak assignable to transition from a single J state is divided by a transition intensity for determination of the relative rotational state populations, P(J), for the v = 1-3 states. The rotational peaks in the $Q_{11} + P_{21}$ branch were used for determining the P(J) values due to its stronger transition intensity than other branches.

Figure 5.4 shows the P(J) values for the v = 1-3 states measured in both a two-color and a one-color laser experiments together with Gauss-type fitting curves. For evaluating the pure P(J) produced by a pump and probe lasers, one-color P(J) values weighted by the $I_{1\ color}/I_{total}$ were subtracted from two-color P(J) values. The Gauss-type fitting curves for the difference between the one-color and two-color P(J) values were shown in Figure 5.4 as a green line. The peak values of the P(J) for the v = 1-3 states were determined and summed in Table 5.3 together with the average NO rotational energies, $<E_{rot}(NO)>$, for each v state, and the fraction, $F_{rot}(v, \Omega)$, of the $<E_{rot}(NO)>$ to the available energy (E_{avail} = 388.7 kJ/mol). The E_{avail} is defined as the difference between the photon energy at 213 nm ($h\nu_{213\ nm}$ = 562.2 kJ/mol) and the O–N bond dissociation energy (D_0(O–N) = 173.5 kJ/mol). I determined P(J) of the v = 1, 2 for both the Ω = 1/2 and 3/2 states, but P(J) of the v = 3 for only the Ω = 1/2 state because considerable inclusion of the one-color laser signal in the total signal disturbed me to obtain the pure two-color signal by the subtraction. The peak P(J) values decreased from J = 60.5 to 56.5 by the increase of v level from v =

1 to 2, but the rotational energy difference between the $J = 56.5$ and 60.5 levels, 9.19 kJ/mol, is smaller than the difference between $v = 1$ and 2 levels, 22.1 kJ/mol, indicating that the P(J) does not much depend on the v level. Huber and coworkers[103] measured the rotational state distributions for the $v = 0$ and 1 states at 250 nm and also found that the J peak value, shown in Table 5.4, was unchanged in two vibrational states. These results imply that the motion correlating to the rotational excitation of the NO fragment does not couple to the N=O bond stretching motion. Consequently, the excess energy in the $S_0 \rightarrow S_2$ photodissociation would be distributed into the NO fragment rotational energy independently of the NO fragment vibrational energy.

Table 5.4 shows the comparison of the J peak values and F_{rot} values among several photolysis wavelengths. The J peak value is found to increase as the photon energy of photolysis laser increases. In addition, the F_{rot} values at 266 nm and 250 nm were determined as 0.13 and 0.17, using non-state-selective detection.[99, 103] In the present study using state-selective detection, the F_{rot} values averaged over $v = 1$-3 states were determined as 0.18 and 0.16 for $\Omega = 1/2$ and 3/2 states, respectively. These values are slightly larger than that at 250 nm. The increase of the J peak and the F_{rot} with an increase of photon energy of photolysis laser suggests the internal energy of a photoinitiated CH_3ONO at the $S_0 \rightarrow S_2$ band is likely transformed into the NO fragment rotational energy as the photon energy of a photolysis light increases.

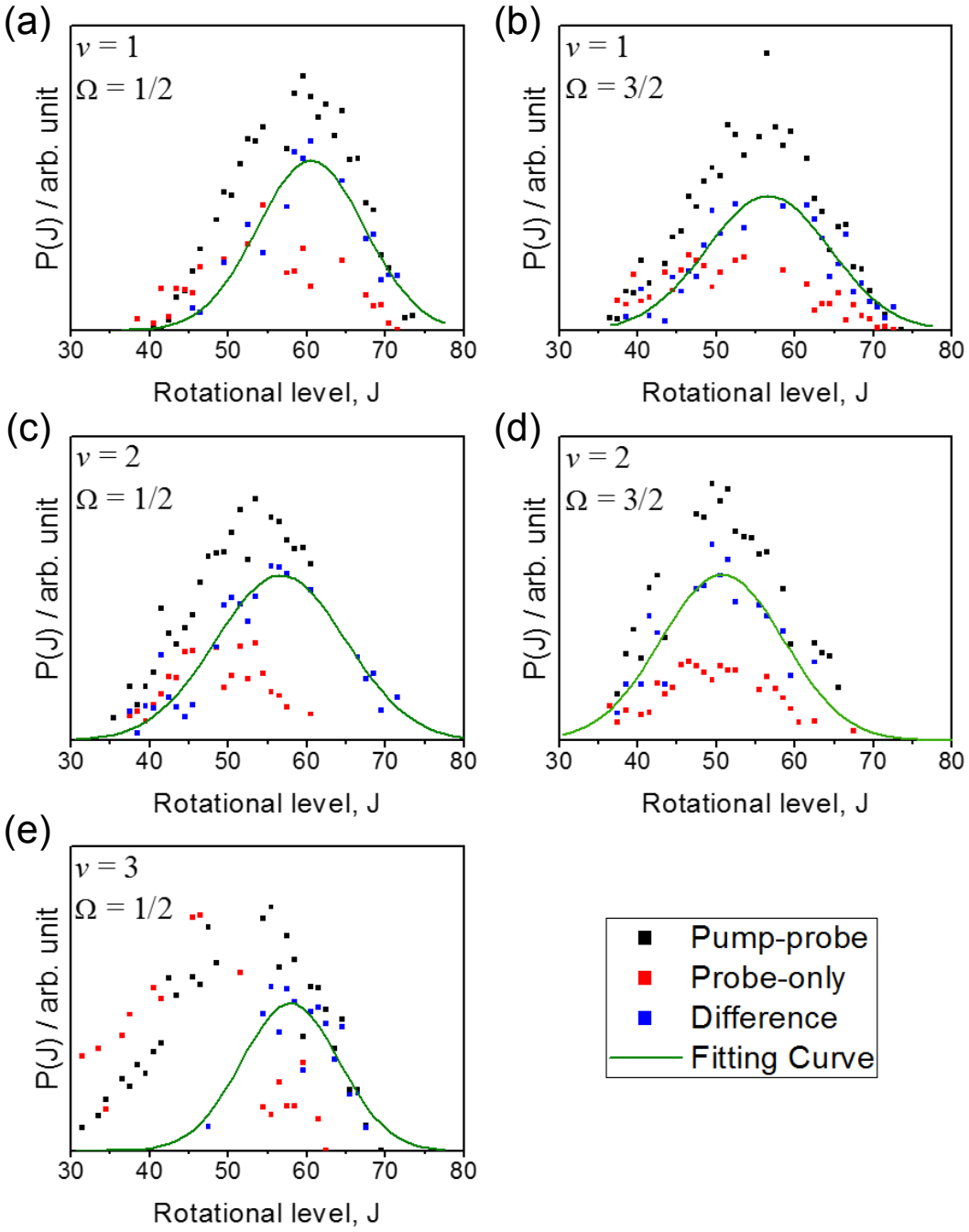

Figure 5.4 The P(*J*) of the NO photofragment generated by the 213 nm photo-dissociation of CH_3ONO. The P(*J*) for $v = 1$, (a) $\Omega = 1/2$ and (b) 3/2 states, for $v = 2$, (c) $\Omega = 1/2$ and (d) 3/2 states, and for $v = 3$, (e) $\Omega = 1/2$ state were shown. Black squares indicate the P(*J*) measured by pump and probe lasers, while Red squares indicate the P(*J*) measured by only probe laser. Blue squares indicate the difference between the pump-probe and the probe-only signals. Green lines indicate the gauss type fitting curves for the blue square.

Table 5.3 Rotational state distributions of the NO (v = 1-3) photofragment at 213 nm.

v	Ω	J peak	FWHM	$\langle E_{rot}(NO)\rangle$ / kJ mol^{-1}	$F_{rot}(v, \Omega)$
v = 1	1/2	60.5	16.0	74.0	0.19
	3/2	56.5	18.5	66.5	0.17
v = 2	1/2	56.5	19.5	64.9	0.17
	3/2	50.5	18.4	53.4	0.14
v = 3	1/2	57.5	14.7	66.3	0.17
	3/2				

Table 5.4 The J peak values of the NO photofragment at several wavelengths

	Ω	v = 0	v = 1	v = 2	v = 3	$F_{rot}(\Omega)$
213 nm [a]	1/2		60.5	56.5	57.5	0.18
	3/2		56.5	50.5		0.16
248 nm [b]	1/2, 3/2	51 ± 2				0.18
250 nm [c]	1/2	50.5	50.5			0.17
266 nm [d]	3/2		40-50			0.13

[a] This work.

[b] Reference 97.

[c] Reference 103.

[d] Reference 99.

Figure 5.5 shows the LIF spectrum of the CH_3O photofragment. As shown in Figure 5.5, a number of vibrational bands were observed. All bands in lower wavenumber region, shown in Figure 5.5 (a), were assigned to the transition from the vibrational ground state and exhibited similar rotational structures. The spectrum in higher wavenumber region was shown in Figure 5.5 (b). Although a number of bands were overlapped in this region, almost bands were also assignable to combination bands correlating to the electronic transitions from $CH_3O(\tilde{X}\ E_2)$ at the vibrational ground level. Figure 5.5 (c) shows with an enlarged wavenumber scale together with a simulated spectrum of the 3_0^2 band at 5 K calculated by Miller and coworkers.[111] In comparison to the simulation, the observed rotational lines were broadened by the Doppler effect as well as that of the NO photoproduct. Although the observed spectrum is slightly hotter than the simulation, all rotational lines in observed bands appear in similar positions of the simulated spectrum.

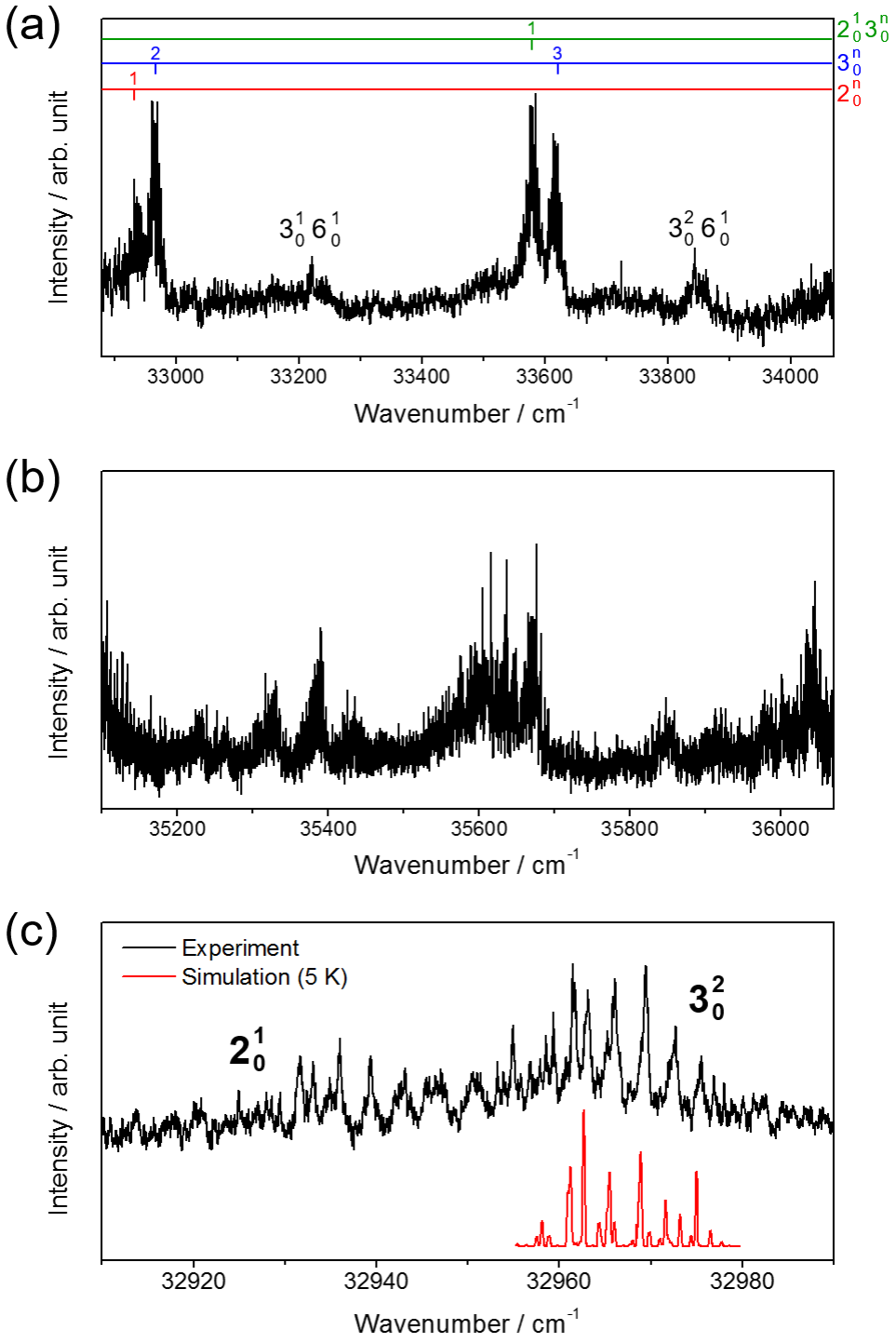

Figure 5.5 LIF spectra of the CH_3O photofragment generated by the 213 nm photodissociation of CH_3ONO; (a) in lower wavenumber region together with the assignments and (b) in higher wavenumber region. (c) A black line indicates the observed LIF spectrum in the range from 32910 cm^{-1} to 32990 cm^{-1}. A red line indicates simulation spectrum at 5 K calculated by Miller and coworkers.[111]

5.3.2 Fragments Internal Energy Correlation

The scattering distributions of the NO photofragments in several rovibrational states were observed. Figure 5.6 shows some of observed NO fragment images and Figure 5.7 shows corresponding recoil velocity distributions. The recoil velocity of the NO fragment was calibrated by using observed images of the NO fragments with around 2000 m/s, which were produced by the 230 nm photodissociation of nitrogen dioxide (NO_2). A linear extrapolation has been applied to determine the recoil velocity value in faster region than 2000 m s^{-1}. Figure 5.8 shows the comparison of the E_{trans} distributions at several photolysis wavelengths. The E_{trans} distribution at each photolysis wavelength has a Gauss-type distribution. Although the lower photon energy at 213 nm than at 193 nm, the NO(v = 1, 2) fragments observed in the present study with a 213 nm photolysis laser are found to be distributed in higher E_{trans} region than the NO fragments generated by the 193 nm photolysis wavelength, which was observed using non-state-selective detection by Huber and coworkers[104]. Differences of experimental apparatuses and calibration methods would be responsible for the inconsistence.

All scattering distributions include non-negligible amount of one-color laser components, which are generated by the photodissociation with smaller photon energy than 213 nm and therefore distributed in slower region than two-color laser components. The lower wavenumber the probe laser is tuned to for detecting the NO fragments in the higher vibrational levels, the slower recoil velocity distribution the one-color distribution becomes. Therefore, the NO fragment scattering distributions for the v = 2 and 3 state, shown in Figure 5.6 (c) and (d), respectively, consist of vaguely two ring-shaped distributions, while those for the v = 1 state, shown in Figures 5.6 (a) and (b), likely consist

of single fast ring-shaped distributions because the greater part of the one-color laser component overlaps with two-color laser component as the probe laser wavelength gets closer to the photolysis laser wavelength of 213 nm. By subtracting a one-color laser signal from a total signal for each internal state, I successfully extracted a pure pump-probe laser signal, which in each internal state has a single recoil velocity distribution (shown as a blue line in Figure 5.7).

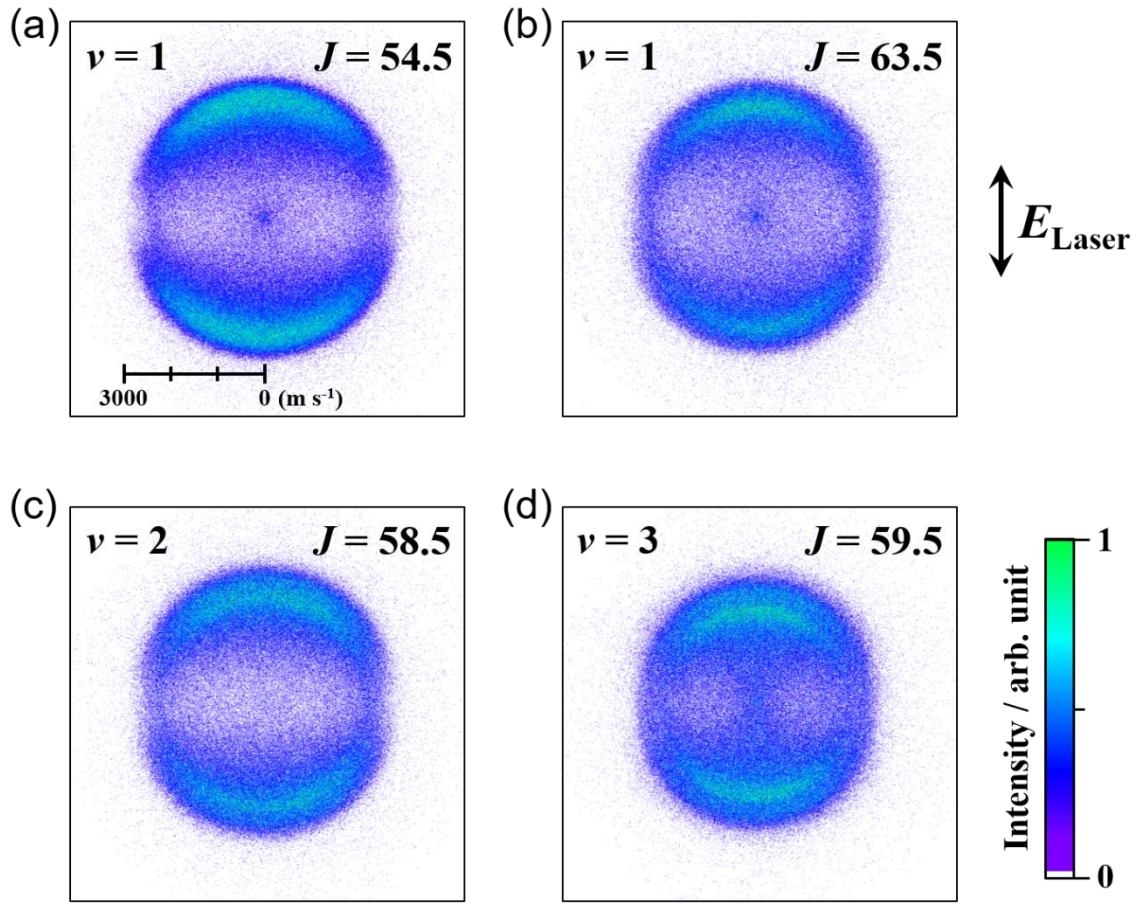

Figure 5.6 State-resolved scattering images of the NO (v = 1-3) photofragment at 213 nm. (a) The NO fragment in the J = 54.5 and Ω = 3/2 state and (b) in the J = 54.5 and Ω = 3/2 state at the v = 1 level, (c) in the J = 58.5 and Ω = 1/2 state at the v = 2 level, and (d) in the J = 59.5 and Ω = 1/2 state at the v = 3 level are shown.

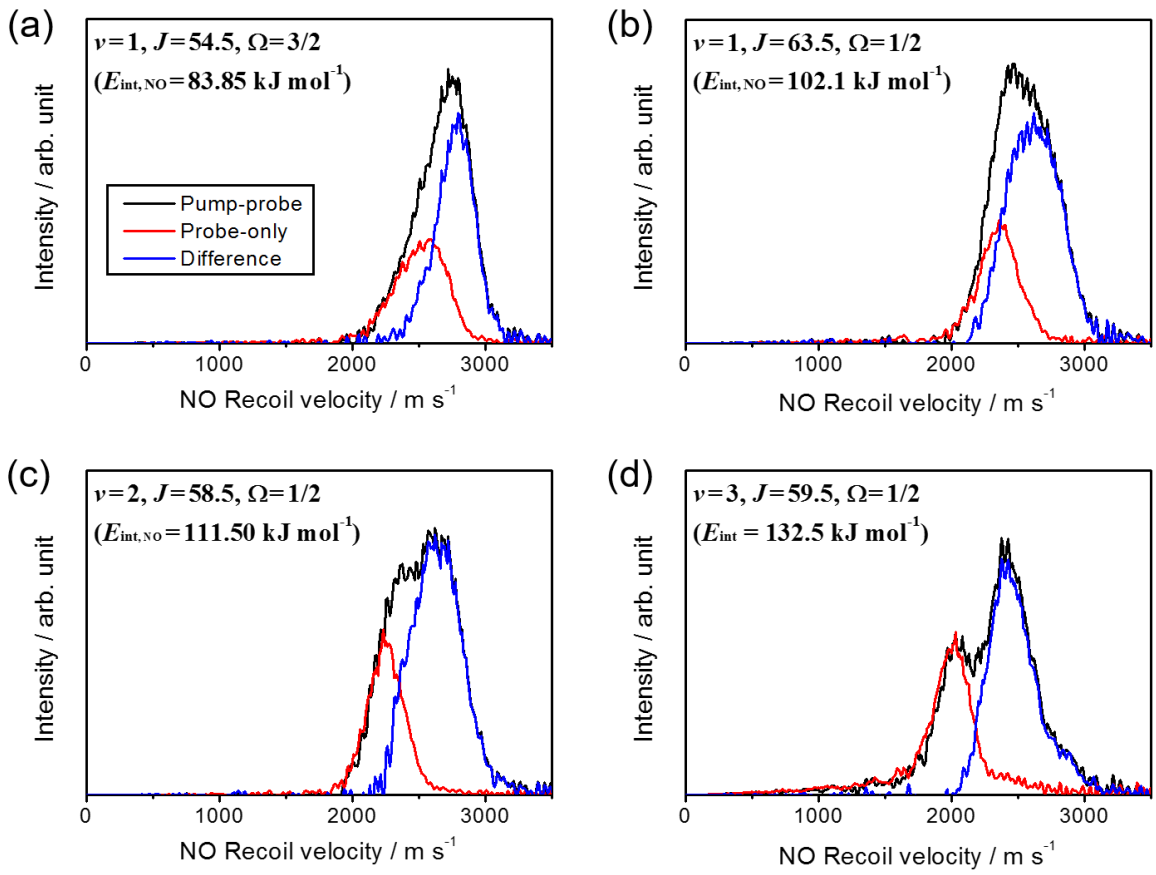

Figure 5.7 Recoil velocity distributions of the NO photofragments at 213 nm; (a) The NO fragment in the $J = 54.5$ and $\Omega = 3/2$ state and (b) in the $J = 54.5$ and $\Omega = 3/2$ state at the $v = 1$ level, (c) in the $J = 58.5$ and $\Omega = 1/2$ state at the $v = 2$ level, and (d) in the $J = 59.5$ and $\Omega = 1/2$ state at the $v = 3$ level are shown. Black lines indicate the pump-probe laser signals, while red lines indicate the probe laser-only signals. Blue lines indicate differences between the pump-probe laser signals and the probe laser-only signals.

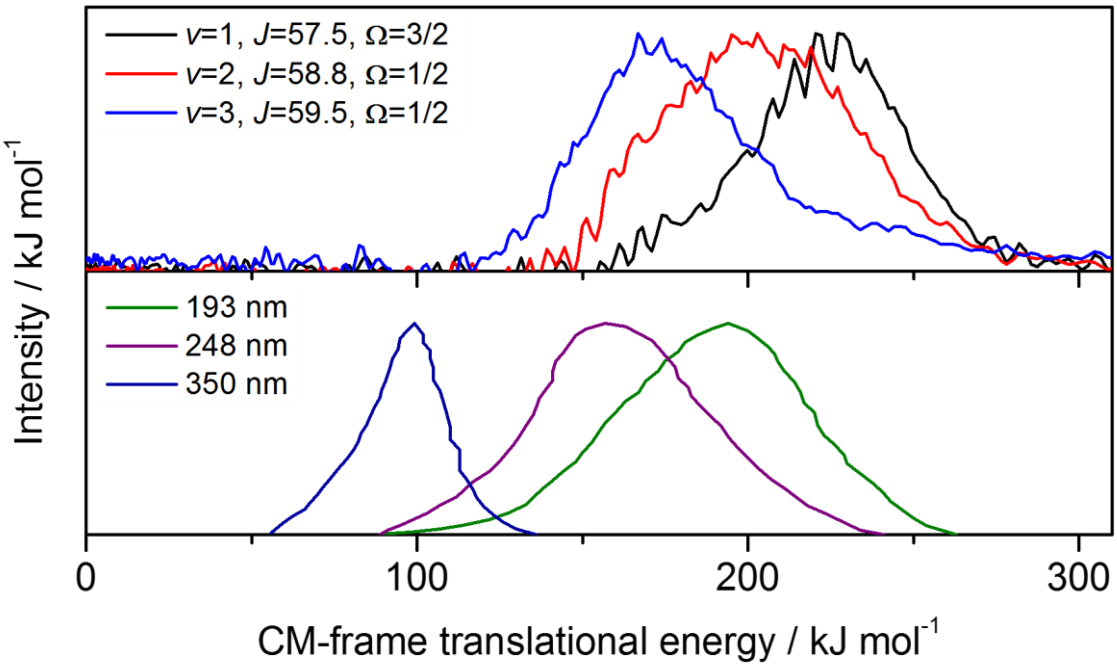

Figure 5.8 The total E_{trans} distributions for the photodissociation of CH_3ONO at several photolysis wavelengths. Upper figure shows the E_{trans} distributions of the NO(v = 1, 2, 3) photofragment at 213 nm observed in the present study. Lower figure shows the E_{trans} distribution of the NO photofragment at 193, 248, and 350 nm observed using non-state-selective detection by Huber and coworkers[104].

The fraction of the average E_{trans}, $<E_{trans}>$, to the available energy, F_{trans}, were determined. Nearly half of the available energy are distributed into the E_{trans}, which can be ascribed to the repulsive character of the S_2 PES. The F_{trans} are larger value than those of previous researches[81, 103, 104] due to the difference of the calibration method, as explained above, but qualitatively consistent with those values. The internal energy of the CH_3O counterproduct, $E_{int}(CH_3O)$, was calculated for each internal state of NO on the basis of the energy conservation law. The average $E_{int}(CH_3O)$ values, $<E_{int}(CH_3O)>$, corresponding to several internal states of the NO fragments were summed at Table 5.5 together with the internal energy of the NO fragment, $E_{int}(NO)$, the $<E_{trans}>$ and the F_{trans}. For comparing the $<E_{trans}>$ and the $<E_{int}(CH_3O)>$ values among the NO fragment internal states, these values are represented as a function of the $E_{int}(NO)$, as shown in Figure 5.9 (a) and (b), respectively. The $<E_{trans}>$ value simply decreased as the increase of the $E_{int}(NO)$ value. Although few data were measured for $v = 2$ and 3, the same trend would be shown independently of the vibrational levels but dependently on total NO internal energy, $E_{int}(NO)$. By the linear fitting, the slop was determined as –0.911, which is close to –1. This suggests that almost of the reduction amount for the $E_{int}(NO)$ is corresponding to the increase amount for the E_{trans}, namely, there is a strong correlation between the $E_{int}(NO)$ and E_{trans}. The $E_{int}(CH_3O)$ value fluctuates within ±10 kJ/mol as the variation of the $E_{int}(NO)$ but does not remarkably depend on the $E_{int}(NO)$. This results indicate that there is not a clear correlation between the $E_{int}(NO)$ and the $E_{int}(CH_3O)$. Huber and coworkers measured a non-state-resolved E_{trans} distribution and the NO and CH_3O photofragments final state distribution and then predicted an anti-correlation between the $E_{int}(NO)$ and the $E_{int}(CH_3O)$; an

internally cold NO fragment is preferentially produced in coincidence with a hot CH_3O fragment and vice versa. Contrary to their prediction, our state-resolved measurement has unveiled the non-internal energy correlation of a photofragment pair; internal energy of a CH_3O fragment is independent of internal energy of a NO fragment. The CH_3O fragment generated by the 213 nm photodissociation would has an average internal energy of around 80 kJ/mol whatever internal energy the NO counterproduct has.

As explained in Section 5.3.1, observed LIF spectrum of the CH_3O photofragment at 213 nm shows internally cold population. This result is inconsistent with the estimated $<E_{int}(CH_3O)>$ as large as around 80 kJ/mol from the NO fragment scattering distributions. One plausible explanation for the difference of the $E_{int}(CH_3O)$ is that the CH_3O photofragment is populated in the excited vibrational states with weak transition intensity to $\tilde{A}\ ^2A_1$ state in the wavenumber region observed in the present study, which is ranges of 32,900-34,000 cm^{-1} and 35,100-36,100 cm^{-1} as shown in Figures 5.5 (a) and (b). Thus the vibrational bands from the excited vibrational levels in the $\tilde{X}\ E_2$ state might be buried in stray light noise. Due to the rotationally cold distributions of the vibrational ground state shown in Figure 5.5, it is quite possible that the CH_3O photofragment in excited vibrational states has also been populated in lower rotational levels unlike the NO photofragment.

The $E_{int}(CH_3O)$ corresponding to each NO state is distributed with in a range of 20 kJ/mol to 140 kJ/mol. Cui and Morokuma[112] have performed ab initio MO calculations for the photodissociation of CH_3O and revealed that CH_3O needs an excess energy of 375.3 kJ/mol to dissociate into CH_2 and OH via isomerization into CH_2OH. Therefore, all CH_3O photofragment at 213 nm

cannot undergo further decomposition under the collisionless condition. Yue *et al.*[101] investigated the 266 nm photodissociation of CH_3ONO and detected OH radicals by using a LIF spectroscopy. They performed DFT calculations and ascribed the OH generation to an intramolecular hydrogen transfer process, in which CH_3ONO needs an excess energy of 302.8 kJ/mol. It is sufficiently lower than the internal energy of photoinitiated CH_3ONO at 266 nm photolysis (449.7 kJ/mol), also 213 nm photolysis (582.2 kJ/mol).

Table 5.5 Energy disposal in the 213 nm photodissociation of CH_3ONO.

NO state	E_{int}(NO) / kJ mol^{-1}	$\langle E_{trans} \rangle$ / kJ mol^{-1}	F_{trans}	$\langle E_{int}(CH_3O) \rangle$ / kJ mol^{-1}
$v = 1, J = 51.5, \Omega = 3/2$	77.5	228.7	0.588	83.8
$v = 1, J = 54.5, \Omega = 3/2$	83.9	227.6	0.586	78.6
$v = 1, J = 57.5, \Omega = 3/2$	90.6	224.9	0.579	74.6
$v = 1, J = 60.5, \Omega = 3/2$	97.6	215.4	0.554	79.9
$v = 1, J = 63.5, \Omega = 1/2$	102.1	201.7	0.519	86.3
$v = 1, J = 66.5, \Omega = 1/2$	109.7	202.9	0.522	77.5
$v = 1, J = 69.5, \Omega = 1/2$	117.6	200.3	0.515	72.1
$v = 2, J = 58.5, \Omega = 1/2$	111.5	203.6	0.524	75.0
$v = 2, J = 60.5, \Omega = 3/2$	118.9	200.3	0.515	70.8
$v = 3, J = 59.5, \Omega = 1/2$	132.5	175.3	0.451	82.2

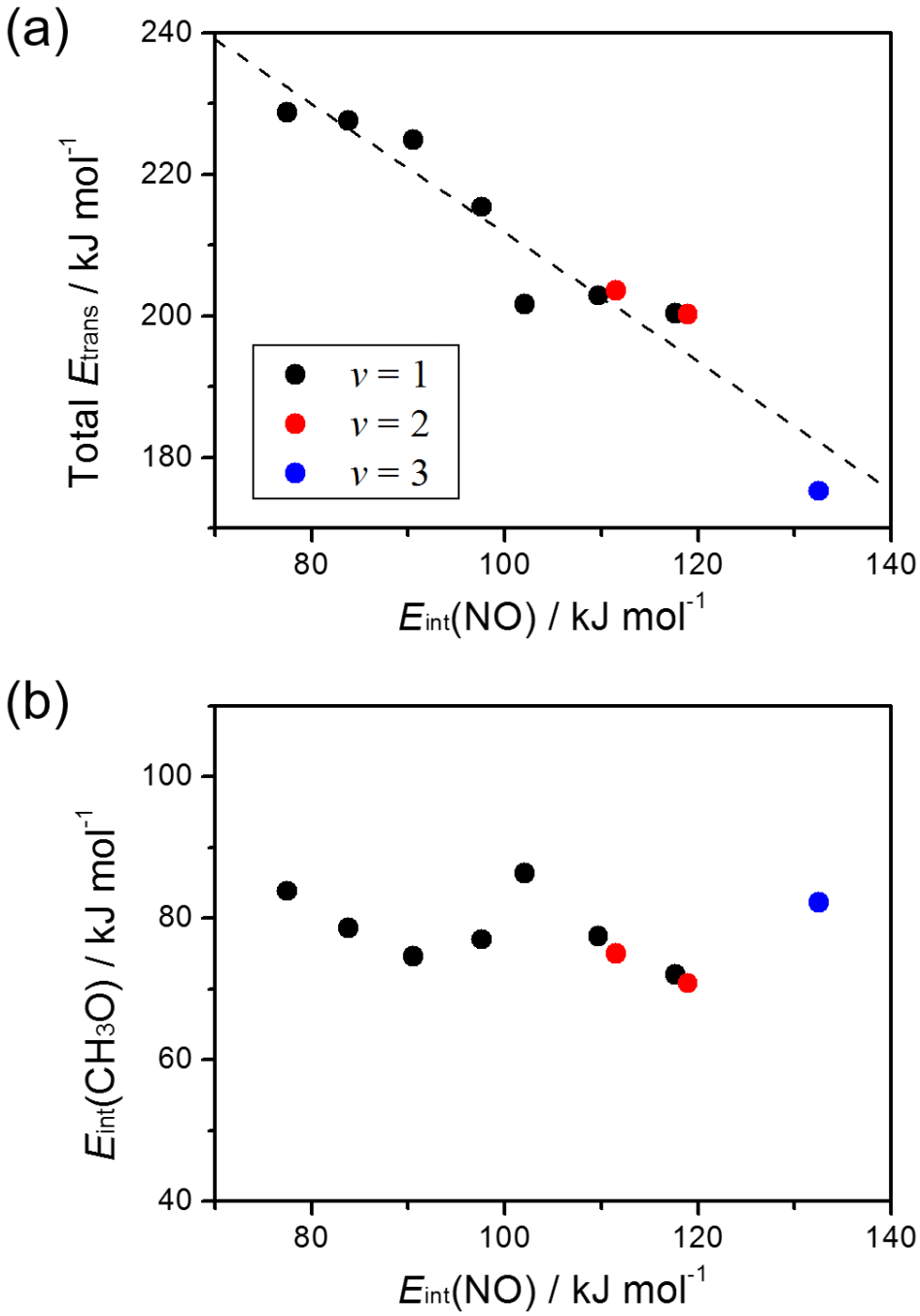

Figure 5.9 (a) The CM frame translational energy vs the NO fragment internal energy. (b) The CH_3O fragment internal energy vs the NO fragment internal energy. Black closed circles in (a) and (b) indicate the $<E_{trans}>$ and the $<E_{int}(CH_3O)>$ for the single NO internal state at the $v = 1$ level, respectively. Red and blue closed circles indicate those for the $v = 2$ and $v = 3$ levels, respectively. A broken line in (a), which obtained by linear fitting, has a slope of –0.911.

5.3.3 Rotational Alignment Effects

I determined the anisotropy parameter, β, for each NO internal state by fitting Eq. (2.2) to an observed scattering distribution of the NO fragment in each internal state. Angular distributions of the NO photofragments cannot be separated into a one-color laser and a two-color laser components due to considerable overlapping between them. Although the determined β values include the contribution from two components, both components would have similar β values and show the similar trend with an increase of E_{int}(NO) due to the photoproducts in the same absorption band. The determined β values are summed at Table 5.6. All β were determined as the positive values in the range of 1.0 to 1.5, which indicate that the $S_0 \rightarrow S_2$ excitation is characterized by the parallel type transition. Huber and coworkers[102] measured the angular distribution at 248 nm and 193 nm with a non-state-selective detection and determined the β values as 1.36 ± 0.10 and 1.08 ± 0.07, respectively. This difference was attributed to the difference of the angle χ between the electronic transition moment and the dissociation direction. They have proposed a contribution of a perpendicular transition is responsible for the increase of the χ at a shorter excitation laser wavelength. If the β values measured in the present study state-selectively are averaged over all v and J states, the average value at 213 nm would indicate a magnitude of 1.2–1.3, according with the trend predicted by Huber and coworkers.

Figure 5.10 shows the β values plotted as a function of E_{int}(NO). As is evident from Figure 5.10, the β value slightly decreases as the E_{int}(NO) increases. Considering the dissociation lifetime on S_2 PES is as short as 25 ± 15 fs, which has been determined by Farmanara *et al.*[98], the difference of the β values between the NO fragment internal states are not caused by the difference

of the dissociation time. It would be due to the decrease of the β values that the larger nuclear motion of dissociating CH_3ONO molecule on the S_2 PES correlates to the production of NO in higher internal states. The violent changes of the nuclear coordinates during the dissociation occur the memory loss of the original structure of the photoinitiated CH_3ONO molecule, obscuring the correlation between the electronic transition moment and the dissociation direction.

Table 5.6 Anisotropy parameters of the NO(v = 1-3) photofragments in several rovibrational levels

NO state	E_{int}(NO) / kJ mol^{-1}	β
$v = 1, J = 51.5, \Omega = 3/2$	77.5	1.41
$v = 1, J = 54.5, \Omega = 3/2$	83.9	1.33
$v = 1, J = 57.5, \Omega = 3/2$	90.6	1.42
$v = 1, J = 60.5, \Omega = 3/2$	97.6	1.29
$v = 1, J = 63.5, \Omega = 1/2$	102.1	1.10
$v = 1, J = 66.5, \Omega = 1/2$	109.7	1.10
$v = 1, J = 69.5, \Omega = 1/2$	117.6	1.08
$v = 2, J = 58.5, \Omega = 1/2$	111.5	1.02
$v = 2, J = 60.5, \Omega = 3/2$	118.9	1.08
$v = 3, J = 59.5, \Omega = 1/2$	132.5	1.07

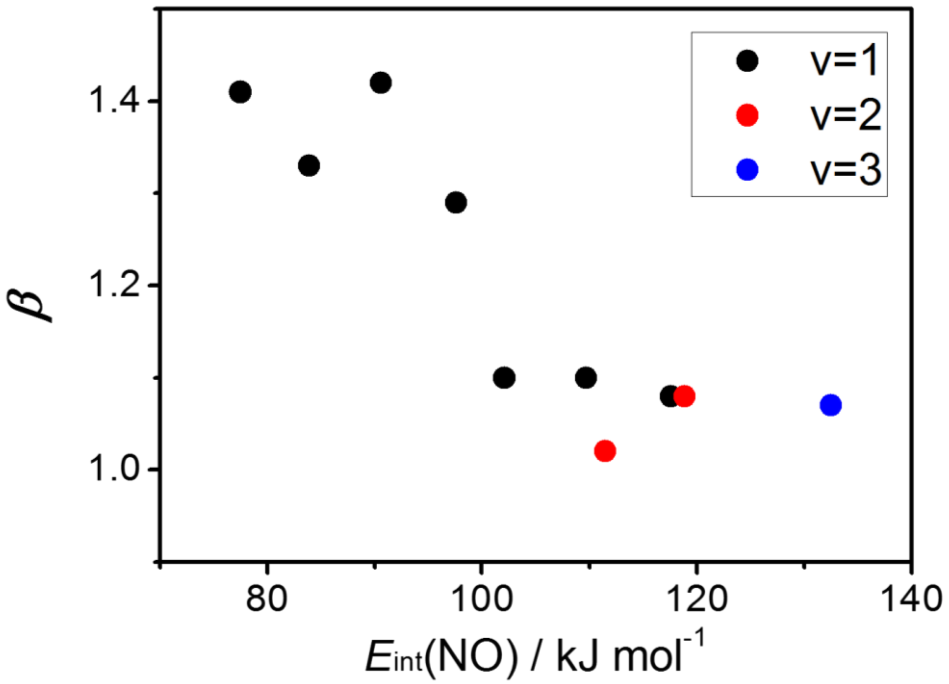

Figure 5.10 The β value vs internal energy of the NO photofragments at 213 nm. Black closed circles indicate the β value of the NO(v = 1) photofragments. Red and blue closed circles indicate the NO(v = 2 and 3) photofragment, respectively.

Figure 5.11 shows the scattering images of the NO(v = 1, J = 60.5) photofragments probed by a linearly polarized laser and a circularly polarized laser. I determined anisotropy parameters up to the fourth-order (β_4) for a linearly polarized probed image and a circularly polarized probed image as β_2 = 1.29 and β_4 = –0.01 and β_2 = 1.15 and β_4 = –0.27, respectively, by fitting the standard formula with high-order Legendre polynomial terms ($P_4(\cos\theta)$) to the observed angular distributions. Although the β_4 value slightly decreases by the change of the probe laser polarization from linear to circular, there are no drastic changes in the bias of the scattering distribution along angular coordinate. This result suggests that the rotational angular momentum vectors of the NO photoproducts are not strongly orientated to the particular direction. It is because changing the probe laser polarization from linear to circular is corresponding to changing the selection rule of a transition from $\Delta K = 0$ to $\Delta K = \pm 1$ (K indicates the component of the total angular momentum, J, on the internal figure axis of a molecule), which enables to investigate the fragment rotational orientation with respect to the polarization of the excitation laser.

Winniczek *et al*.[97] and Huber and coworkers[103] have investigated the molecular alignment at 266 nm and 250 nm, respectively. They concluded that the S_2 dissociation of CH_3ONO occurs preferentially in the C–O–N=O plane and angular momentum vector J is perpendicular to the photolysis transition moment in the plane. In the present study, striking alignment effects were not observed at 213 nm, which is shorter than their utilizing laser. This result implies that the N=O bond tilts to out of the C–O–N=O plane by the nascent force

generated by the increase of the excess energy at 213 nm after the photoexcitation to the S_2 PES. Consequently, the orientation of J would be extended to the non-perpendicular direction to the C–O–N=O plane.

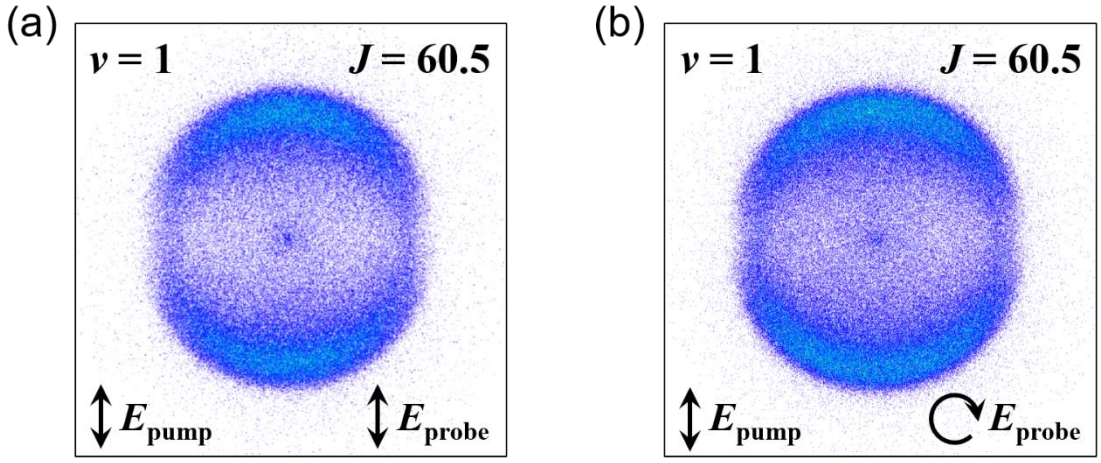

Figure 5.11 The scattering images of the NO(v = 1, J = 60.5) photofragments at 213 nm probed by (a) a linearly polarized laser and (b) a circularly polarized laser. The anisotropy parameters of (a) are determined as β_2 = 1.29 and β_4 = –0.01, while those of (b) are β_2 = 1.15 and β_4 = –0.27.

5.4 Summary and Conclusion

I performed the pump-probe experiment for investigate the photodissociation of CH_3ONO at the photolysis wavelength of 213 nm. The REMPI spectra were measured for the NO photofragment in the v = 1, 2, 3 states. The NO photofragment are found to be distributed up to at least the v = 3 state and be preferentially populated in the v = 1 state. The NO fragment rotational distribution is not found to be strongly dependent on the v levels, implying that the motion correlating to the rotational excitation of the NO fragment does not couple to the N=O bond stretching motion during the O–N bond dissociation on the S_2 PES. The J peak value and the F_{rot} slightly increase as the photon energy of the photolysis laser increases. This result indicates that the internal energy a photoinitiated CH_3ONO at the $S_0 \rightarrow S_2$ band is likely transformed into the NO fragment rotational energy as the photon energy of a photolysis light increases. The state-resolved scattering distributions of the NO(v = 1, 2, 3) photofragment were observed in both the pump-probe laser experiment and only the probe laser experiment under the same other conditions. The pure pump-probe laser components of the recoil velocity distributions of the NO fragments were successfully extracted from total signals by the subtraction of one color laser signal from total signal. Similar to the previous researches using different photolysis laser wavelengths, the available energy at the 213 nm photolysis wavelength is preferentially distributed into the translational energy. The internal energy of the CH_3O counterproduct was calculated on the basis of the energy conservation law. The CH_3O photoproduct is enough stable not to undergoes further dissociation reaction. The internal energy of the CH_3O coun-

terproduct has been found not to correlate with the NO fragment internal energy. The β value for each NO internal state was obtained from the angular distribution and then, is found to decrease as the E_{int}(NO) increases. These decrease implies that the highly internally excited NO product is generated through large structural changes from the photoinitiated CH_3ONO, which occurs the loss of memory for the direction of the electronic transition moment. The circularly polarized probe light was utilized for investigating the NO fragment rotational alignment. The anisotropy parameters were determined for both detections using probe laser with polarization and a circular polarization and indicated similar values independently of the laser polarization. The J alignment randomization of the NO photofragment in the peak region of the $S_0 \rightarrow S_2$ absorption band would be caused by the nascent force on the S_2 PES tilting the N=O bond to out of the C–O–N=O plane.

The LIF spectrum of the CH_3O photofragment was measured for directly observing the internal state distributions. I observed only the vibrational bands corresponding to the transitions from the vibrational ground state, which show relatively rotationally cold structures unlike the NO fragment. These results are inconsistent with the $<E_{int}(CH_3O)>$ value estimated from the state-resolved scattering distributions of the NO counterproduct. This inconsistence might be due to the preferential production of the CH_3O fragment in the vibrational states with too small transition intensity to be observed. It is quite possible that the CH_3O photofragments in excited vibrational states have also been populated in lower rotational levels.

Chapter 6.
Concluding Remarks

In this thesis, I have revealed the photodissociation dynamics of the three polyatomic molecules with different chromophores by the measurement of the photoproducts final state distributions and scattering distributions. In Chapter 2, I have explained the experimental apparatus which I have designed and developed for the present researches, and experimental methods and principles. In Chapter 3, I investigated the photodissociation dynamics of allyl iodide (C_3H_5I) at 266 nm and 213 nm. Site-selective photodissociation dynamics initiated by the excitation of C=C and C–I bonds has been observed. In Chapter 4, I investigated the multiple product pathways in the $\pi\pi^*$ photodissociation dynamics of nitromethane (CH_3NO_2). The present results support the C–N bond dissociation pathways, methoxy radical (CH_3O) production pathway, and N–O bond dissociation pathway. The slower components of CH_3 and NO products suggest that the CH_3NO product with larger internal energy than the C–N bond dissociation barrier undergoes further decomposition. The origin of electronic excited NO($A\ ^2\Sigma^+$) was determined as the accidental photoexcitation of the NO($X\ ^2\Pi$) product by the pump laser. In Chapter 5, I investigated the direct O–N bond dissociation dynamics in the $S_0 \rightarrow S_2$ photoexcited methyl nitrite (CH_3ONO). The detailed nuclear dynamics of CH_3ONO on the S_2 PES has been elucidated.

Finally, I strongly believed that the present results will be important benchmark for understanding photodissociation dynamics of larger polyatomic molecules with the same chromophore. In addition, the knowledge obtained in the present research will widely contribute to development of both experimental and theoretical studies of reaction dynamics.

References

[1] D. H. Parker, and A. Eppink, Journal of Chemical Physics **107** (1997) 2357.
[2] A. Zewail, Journal of Physical Chemistry a **104** (2000) 5660.
[3] D. Proch, and T. Trickl, Review of Scientific Instruments **60** (1989) 713.
[4] S. Ashworth, H, and J. Brown, M, *An Atlas of Optogalvanic Transitions in Ne* (SERC, 1991),
[5] B. Chang *et al.*, Review of Scientific Instruments **69** (1998) 1665.
[6] W. Li *et al.*, Review of Scientific Instruments **76**, ARTN 063106 (2005)
[7] A. Eppink, and D. H. Parker, Review of Scientific Instruments **68** (1997) 3477.
[8] G. Garcia, L. Nahon, and I. Powis, Review of Scientific Instruments **75** (2004) 4989.
[9] C. W. Worrell, J. Electron. Spectrosc. Relat. Phenom. **3** (1974) 359.
[10] R. A. Boschi, and D. R. Salahub, Mol. Phys. **24** (1972) 735.
[11] B. Parsons, D. Szpunar, and L. Butler, J. Phys. Chem. A **104** (2000) 10669.
[12] T. P. M. M.E. Jenkin, S.J. Shalliker, and G.D. Hayman, J. Chem. Soc. Faraday Trans **89** (1993) 433.
[13] H. Keller-Rudek *et al.*, (Max-Planck Institute for Chemistry,, Mainz, Germany, 2013), pp. 365.
[14] A. V. Baklanov *et al.*, Chem. Phys. **184** (1994) 357.
[15] A. V. Baklanov *et al.*, J. Chem. Soc., Faraday Trans. **92** (1996) 1681.
[16] A. V. Baklanov *et al.*, J. Chem. Phys. **112** (2000) 6649.
[17] J. D. Getty, X. M. Liu, and P. B. Kelly, J. Phys. Chem. **96** (1992) 10155.
[18] J. D. Getty *et al.*, J. Am. Chem. Soc. **113** (1991) 801.
[19] H. Fan, and S. T. Pratt, J. Chem. Phys. **125**, 144302 (2006)
[20] D. E. Szpunar *et al.*, J. Chem. Phys. **119** (2003) 5078.
[21] D. E. Szpunar *et al.*, J. Phys. Chem. B **106** (2002) 8086.
[22] I. Fischer *et al.*, Int. J. Mass spectrom. **261** (2007) 227.
[23] H. C. Kwon *et al.*, J. Chem. Phys. **116** (2002) 2675.
[24] H. J. Deyerl, I. Fischer, and P. Chen, J. Chem. Phys. **110** (1999) 1450.
[25] D. W. Minsek, and P. Chen, J. Phys. Chem. **97** (1993) 13375.
[26] D. W. Kohn, H. Clauberg, and P. Chen, Rev. Sci. Instrum. **63** (1992) 4003.
[27] E. J. Hintsa, X. S. Zhao, and Y. T. Lee, J. Chem. Phys. **92** (1990) 2280.
[28] A. Kramida, Ralchenko, Yu., Reader, J., and NIST ASD Team, (National Institute of Standards and Technology, Gaithersburg, MD. , 2013).
[29] *NIST Chemistry WebBook, NIST Standard Reference Database Number 69* (National Institute of Standards and Technology, Gaithersburg MD, 20899, P.J. Linstrom and W.G. Mallard edn.,
[30] H. Fan, and S. T. Pratt, J. Phys. Chem. A **111** (2007) 3901.
[31] R. Boschi, and D. Salahub, Mol. Phys. **24** (1972) 735.
[32] A. Eppink, and D. Parker, J. Chem. Phys. **109** (1998) 4758.

[33] W. Hess *et al.*, J. Chem. Phys. **84** (1986) 2143.
[34] S. Riley, and K. Wilson, Faraday Discuss. **53** (1972) 132.
[35] H. Y. Fan, and S. T. Pratt, J. Chem. Phys. **123**, 204301 (2005)
[36] Y. S. Kim *et al.*, J. Phys. Chem. A **101** (1997) 7576.
[37] D. K. Zaouris *et al.*, J. Chem. Phys. **135**, 094312 (2011)
[38] Y. Tang *et al.*, J. Chem. Phys. **126**, 064302 (2007)
[39] W. K. Kang *et al.*, J. Phys. Chem. **98** (1994) 1525.
[40] R. S. Mulliken, Phys. Rev. **61** (1942) 277.
[41] R. S. Mulliken, J. Chem. Phys. **8** (1940) 382.
[42] P. Zou *et al.*, Physical Chemistry Chemical Physics **10** (2008) 713.
[43] A. G. Sage *et al.*, Physical Chemistry Chemical Physics **13** (2011) 8075.
[44] H. J. Hwang, and M. A. ElSayed, J. Photochem. Photobiol., A **102** (1996) 13.
[45] I. Fischer, and P. Chen, J. Phys. Chem. A **106** (2002) 4291.
[46] S. Davis, C. Law, and H. Wang, J. Phys. Chem. A **103** (1999) 5889.
[47] L. Ji *et al.*, J. Chem. Phys. **125**, 164307 (2006)
[48] Y. Liu, and L. J. Butler, J. Chem. Phys. **121** (2004) 11016.
[49] R. A. Boschi, and D. R. Salahub, Mol. Phys. **24** (1972) 289.
[50] M. S. Park, K. W. Lee, and K. H. Jung, J. Chem. Phys. **114** (2001) 10368.
[51] P. E. Schoen *et al.*, Chem. Phys. Lett. **90** (1982) 272.
[52] J. Mialocq, and J. Stephenson, Chem. Phys. **106** (1986) 281.
[53] H. S. Kwok *et al.*, Int. J. Chem. Kinet. **13** (1981) 1125.
[54] S. Zabarnick, J. W. Fleming, and A. P. Baronavski, J. Chem. Phys. **85** (1986) 3395.
[55] G. Greenblatt, H. Zuckermann, and Y. Haas, Chem. Phys. Lett. **134** (1987) 593.
[56] A. M. Wodtke, E. J. Hintsa, and Y. T. Lee, J. Chem. Phys. **84** (1986) 1044.
[57] M. S. Park *et al.*, Chem. Phys. **270** (2001) 133.
[58] N. C. Blais, J. Chem. Phys. **79** (1983) 1723.
[59] L. J. Butler *et al.*, J. Chem. Phys. **79** (1983) 1708.
[60] K. Q. Lao *et al.*, J. Chem. Phys. **93** (1990) 3958.
[61] D. B. Moss, K. A. Trentelman, and P. L. Houston, J. Chem. Phys. **96** (1992) 237.
[62] Y. Q. Guo, A. Bhattacharya, and E. R. Bernstein, J. Phys. Chem. A **113** (2009) 85.
[63] J. Rodriguez *et al.*, J. Phys. Chem. A **117** (2013) 8175.
[64] J. F. Arenas *et al.*, J. Chem. Phys. **119** (2003) 7814.
[65] J. F. Arenas *et al.*, J. Chem. Phys. **122** (2005) 084324.
[66] M. Isegawa *et al.*, J. Chem. Phys. **140**, ARTN 244310 (2014)
[67] W. D. Taylor *et al.*, Int. J. Chem. Kinet. **12** (1980) 231.
[68] Y. Kohge *et al.*, Chem. Phys. Lett. **556** (2013) 49.
[69] K. Chen, and E. Yeung, J. Chem. Phys. **69** (1978) 43.
[70] M. E. Jacox, J. Phys. Chem. Ref. Data **32** (2003) 1.

[71] J. Brand, K. Cross, and A. Hoy, Can. J. Phys. **60** (1982) 1081.
[72] A. Weaver *et al.*, J. Chem. Phys. **90** (1989) 2070.
[73] S. W. Benson, *Thermochemical Kinetics, 2nd Ed.* (Wiley, New York, 1976),
[74] R. Jost *et al.*, Journal of Chemical Physics **105** (1996) 1287.
[75] S. P. Sander, Abbatt, J., Barker, J. R., Burkholder, J. B. , Friedl, R. R. , Golden, D. M. , Huie, R. E. , Kolb, C. E. , Kurylo, M. J. , Moortgat, G. K. , Orkin, V. L., and Wine, P. H., *Chemical Kinetics and Photochemical Data for Use in Atmospheric Studies, Evaluation Number 17* (JPL Publication, Jet Propulsion Laboratory, Pasadena, 2011),
[76] G. KING, and D. MOULE, Canadian Journal of Chemistry-Revue Canadienne De Chimie **40** (1962) 2057.
[77] M. DUBS, U. BRUHLMANN, and J. HUBER, Journal of Chemical Physics **84** (1986) 3106.
[78] B. A. Keller, P. Felder, and J. R. Huber, Chemical Physics Letters **124** (1986) 135.
[79] U. Bruhlmann, M. Dubs, and J. R. Huber, Journal of Chemical Physics **86** (1987) 1249.
[80] U. Bruhlmann, and J. R. Huber, Chemical Physics Letters **143** (1988) 199.
[81] B. A. Keller, P. Felder, and J. R. Huber, Journal of Physical Chemistry **91** (1987) 1114.
[82] M. DOCKER *et al.*, Journal of the Chemical Society-Faraday Transactions Ii **85** (1989) 1169.
[83] E. Kades *et al.*, Journal of Physical Chemistry **97** (1993) 989.
[84] E. Kades, M. Rosslein, and J. R. Huber, Chemical Physics Letters **209** (1993) 275.
[85] G. RADHAKRISHNAN, and R. ESTLER, Chemical Physics Letters **100** (1983) 403.
[86] G. Inoue *et al.*, Journal of Chemical Physics **87** (1987) 5722.
[87] F. Lahmani, C. Lardeux, and D. Solgadi, Journal of Chemical Physics **73** (1980) 4433.
[88] F. Lahmani, C. Lardeux, and D. Solgadi, Chemical Physics Letters **129** (1986) 24.
[89] F. Lahmani, C. Lardeux, and D. Solgadi, Chemical Physics Letters **102** (1983) 523.
[90] O. B. Dazy *et al.*, Chemical Physics **94** (1985) 247.
[91] M. R. S. McCoustra, M. Hippler, and J. Pfab, Chemical Physics Letters **200** (1992) 451.
[92] M. Hippler, M. R. S. McCoustra, and J. Pfab, Chemical Physics Letters **198** (1992) 168.
[93] M. Hippler, F. A. H. Aljanabi, and J. Pfab, Chemical Physics Letters **192** (1992) 173.
[94] M. HIPPLER, and J. PFAB, Journal of the Chemical Society-Faraday Transactions **88** (1992) 2109.
[95] S. A. Reid, J. T. Brandon, and H. Reisler, Chemical Physics Letters **209** (1993) 22.
[96] J. M. Mestdagh *et al.*, Journal of Chemical Physics **103** (1995) 1013.
[97] J. W. Winniczek *et al.*, Journal of Chemical Physics **90** (1989) 949.
[98] P. Farmanara, V. Stert, and W. Radloff, Chemical Physics Letters **303** (1999) 521.
[99] H. M. Yin *et al.*, Journal of Chemical Physics **118** (2003) 8248.
[100] X. Yue *et al.*, Chemical Physics Letters **426** (2006) 57.

[101] X. F. Yue *et al.*, Journal of Physical Chemistry A **113** (2009) 3303.
[102] P. Felder, B. A. Keller, and J. R. Huber, Zeitschrift Fur Physik D-Atoms Molecules and Clusters **6** (1987) 185.
[103] H. U. Suter, U. Bruhlmann, and J. R. Huber, Chemical Physics Letters **171** (1990) 63.
[104] C. S. Effenhauser, P. Felder, and J. R. Huber, Journal of Physical Chemistry **94** (1990) 296.
[105] M. Nonella, and J. R. Huber, Chemical Physics Letters **131** (1986) 376.
[106] S. Hennig *et al.*, Journal of Chemical Physics **87** (1987) 3522.
[107] M. NONELLA *et al.*, Journal of Chemical Physics **91** (1989) 194.
[108] A. UNTCH *et al.*, Journal of Chemical Physics **99** (1993) 9553.
[109] J. R. Huber, and R. Schinke, Journal of Physical Chemistry **97** (1993) 3463.
[110] R. W. Nicholls, J. Res. NBS **68A** (1964) 535.
[111] D. Powers, M. Pushkarsky, and T. Miller, Journal of Chemical Physics **106** (1997) 6863.
[112] Q. Cui, and K. Morokuma, Chemical Physics Letters **263** (1996) 54.